Development and evaluation of new approaches for fluorescence-guided surgery and therapy of pancreatic ductal adenocarcinoma using orthotopic mouse models

Doctoral Thesis

In partial fulfilment of the requirements for the degree

"Doctor rerum naturalium (Dr. rer. nat.)"
in the Molecular Medicine Study Program
at the Georg-August-University Göttingen

submitted by Mara Saccomano, M.Sc.

born in Portogruaro (Venezia, Italy)

Göttingen, May 2016

Members of the Thesis Committee:

Supervisor

- **Prof. Dr. Frauke Alves**

  Department of Haematology and Medical Oncology, Institute of Diagnostic and Interventional Radiology (Georg-August University Medical School of Göttingen) and
  Department of Molecular Biology of Neuronal Systems (Max-Planck Institute for Experimental Medicine, Göttingen)

Second member of the Thesis Committee

- **Prof. Dr. Blanche Schwappach**

  Department of Molecular Biology (Georg-August University Medical School of Göttingen / Max-Planck Institute for Biophysical Chemistry, Göttingen)

Third member of the Thesis Committee

- **Prof. Dr. Hubertus Jarry**

  Department of Endocrinology (Georg-August University Medical School of Göttingen)

Date of Disputation:

AFFIDAVIT

Here I declare that my doctoral thesis entitled "**Development and evaluation of new approaches for fluorescence-guided surgery and therapy of pancreatic ductal adenocarcinoma (PDAC) using orthotopic mouse models”** has been written independently with no other sources and aids than quoted.

Mara Saccomano
Göttingen, May 2016

If you think you can, you can.
If you think you can’t, you are right.

List of Publications

Zeeberg K., Cardone R.A., Greco M.R., **Saccomano M.**, Nøhr-Nielsen A., Alves F., Pedersen S.F., and Reshkin S.J.: Assessment of different 3D culture systems to study tumor phenotype and chemosensitivity in pancreatic ductal adenocarcinoma (PDAC). Oncology Report, 2016. (in press)

Saccomano M., Dullin C., Alves F., and Napp J.: Preclinical evaluation of near-infrared (NIR) fluorescently labeled Cetuximab as a potential tool for fluorescence-guided surgery. International Journal of Cancer, 2016. (submitted, under review)

Giannuzzo A.*, **Saccomano M.***, Napp J., Alves F.*, and Novak I.*: Therapeutic targeting of the P2X7 receptor in pancreatic cancer and stellate cells. International Journal of Cancer, 2016. (submitted, under revision)

* equal contribution

Cardone R.A., Greco M.R., Zeeberg K., Zaccagnino A., **Saccomano M.**, Bellizzi A., Bruns P., Menga M., Pilarsky C., Schwab A., Alves F., Kalthoff H., Casavola V., and Reshkin S.J.: NHE1-centered signaling cassette drives Epidermal Growth Factor Receptor–Dependent Pancreatic Tumor Metastasis and Is a Target for Combination Therapy. Neoplasia. 2015 Feb;17(2):155-66. doi: 10.1016/j.neo.2014.12.003.

Table of Content

List of Publications I

Table of Content II

Acknowledgements V

Abstract VII

List of Figures X

List of Tables XI

List of Abbreviations XII

1. Introduction 1

1.1 Anatomy and physiology of the pancreas 1

1.2 Pancreatic Ductal Adenocarcinoma (PDAC) 1

1.2.1 Desmoplastic reaction 2

1.2.2 Treatment 3

1.2.2.1 Early stage disease 3

1.2.3.2 Locally advanced and systemic PDAC 4

1.3. Orthotopic PDAC mouse models 4

1.4. Molecular imaging for tumor monitoring in preclinical models 5

1.4.1 Computed tomography 6

1.4.2 *In vivo* fluorescence imaging 6

1.4.2.1 Fluorescent labels for *in vivo* NIRF imaging 6

1.4.2.2 The principle of *in vivo* fluorescence imaging 8

1.5 Fluorescence-guided surgery 9

1.6 Targeting EGFR and NHE1 in cancer 10

1.6.1 The role of EGFR in cancer 10

1.6.1.1 Cetuximab as antibody-based targeting of EGFR 12

1.6.1.2 Erlotinib as tyrosine kinase inhibitor of EGFR 12

1.6.2 The role of NHE1 in cancer 12

1.6.2.1 Cariporide 14

Aims of the Study 15

2 Material and Methods 17

2.1 Material 17

2.1.1 Equipment 17

2.1.2 Consumable supplies 18

2.1.3 Chemicals and reagents 19

2.1.4 Buffers and freezing medium 20

2.1.5 Kits 20

2.1.6 Anesthetics and Analgesic 21

2.1.7 Fluorescent probes 21

2.1.8 Therapeutic Drugs 21

2.1.9 Antibodies 22

2.1.10 Eukaryotic cell lines 22

2.1.11 Cell culture media 23

2.1.12 Software 23

2.1.13 Animals 23

2.2. Methods 24

2.2.1 Molecular Biology 24

2.2.1.1 Protein extraction and BCA protein assay 24
2.2.1.2 SDS-PAGE and Western Blot 24
2.2.2 Cell biological methods 25
2.2.2.1 Cell culture conditions 25
2.2.2.2 Cryoconservation 25
2.2.2.3 Revitalization 26
2.2.2.4 *In vitro* binding assay to PDAC cells for Cetuximab NIRF conjugates 26
2.2.2.5 Cell preparation for implantation 26
2.2.3 *In vivo* experiments 27
2.2.3.1 Orthotopic PDAC mouse models 27
2.2.3.2 NIRF fluorescence imaging 28
2.2.3.3 Co-registration of fluorescence tomography and CT data 31
2.2.3.4 Fluorescence-guided dissection 32
2.2.3.5 Schedule and evaluation of Cariporide-Erlotinib treatment 33
2.2.3.6 Tissue preparation 34
2.2.4 Histology of tissue sections 34
2.2.4.1 Hematoxylin-Eosin (HE) staining 34
2.2.4.2 Immunohistochemistry staining of tissue sections 35
2.2.4.3 Collagen staining 35
2.2.5 NIRF analysis of tumor and metastases sections 36
2.2.5.1 Immunofluorescence and NIRF microscopy 36
2.2.5.2 Odyssey scans of tissue sections 37
2.2.6 Statistical analysis 37

3. Results 38
3.1 Orthotopic human PDAC mouse models 38
3.1.1 Growth characteristics and time of tumor development 38
3.1.2 Histological features and desmoplastic reaction of primary tumors developed in PDAC mouse models 39
3.2 NIRF labeled Cetuximab targeting EGFR as a tool for fluorescence-guided surgery 42
3.2.1 Characterization of PDAC cell lines for EGFR expression 42
3.2.2 *In vitro* binding studies of NIRF labeled Cetuximab to EGFR expressing PDAC cells 43
3.2.3 Characterization of EGFR expressing orthotopic PDAC xenografts 44
3.2.3.1 Tumor growth, invasion and metastatic spread of ASPC-1 and MIA PaCa-2 mouse models ..45
3.2.3.2 Characterization of EGFR expression in tumor tissue obtained from PDAC mouse models ...46
3.2.4 Characterization of the *in vivo* binding of Cetux-Alexa-647 in EGFR expressing PDAC xenografts 47
3.2.4.1 Cetux-Alexa-647 accumulates within primary PDAC tumors *in vivo* 47
3.2.4.2 Validation of the specificity of *in vivo* signals by fluorescence LTs 51
3.2.5 Cetux-Alexa-647 detects PDAC primary tumors and metastases by *ex vivo* optical imaging 52
3.2.6 Validation of Cetux-Alexa-647 fluorescence by NIRF microscopy 55
3.2.7 Cetux-800CW detects AsPC-1 tumors and metastases during fluorescence-guided dissection 56
3.2.8 *Ex vivo* validation of Cetux-800CW fluorescence signals of tumor and metastases 58
3.3 Proof-of-Concept: Validation of treatment efficacy targeting EGFR in combination with NHE1 in the orthotopic AsPC-1 tumor mouse model 59
3.3.1 Treatment schedule of Erlotinib/Cariporide therapy in AsPC1 tumor bearing mice 59
3.3.2 Tolerance of the treatment and effect on body weight of the mice 60
3.3.3 Effect of Erlotinib/Cariporide therapy on primary tumor growth 61
3.3.4 Effect of Erlotinib/Cariporide therapy on tumor infiltration into the stomach and duodenum 62
3.3.5 Effect of Erlotinib/Cariporide therapy on metastatic spread 64

4. Discussion 67
4.1 Orthotopic human PDAC mouse models with distinct growth and metastatic behavior 67

4.2 NIRF labeled Cetuximab as a tool for fluorescence-guided surgery 70
4.2.1 Visualization of PDAC primary tumors and metastases with Cetux-Alexa-647 by NIRF imaging 70
4.2.2 Identification of AsPC-1 primary tumor and metastatic sites with Cetux-800CW by fluorescence-guided dissection 72
4.3 Anti metastatic effect of NHE1 and EGFR inhibition in PDAC xenografts............... 73

5. Summary and Conclusions 76

Bibliography........ 78

Curriculum vitae........ 85

Acknowledgements

First and foremost, I want to express my deep gratitude to my supervisor Prof. Dr. Frauke Alves for the tremendous opportunity that she gave me by choosing me as EU-Marie Curie fellow in her lab and being part of the amazing group that turned out to be ‘IonTrac’. Moreover, I would like to thank her for giving me the possibility to develop such different projects and to collaborate with different research groups. Last, I want to thank her for the high quality of critical support for this thesis which will definitely help me on growing as a researcher.

I also would like to acknowledge the members of my Thesis Committee, Prof. Dr. Blanche Schwappach and Prof. Dr. Hubertus Jarry, together with Prof. Dr. Luis Pardo and Prof. Dr. Walter Stühmer, for participating at my PhD thesis committee meetings and for the nice and fruitful discussions on my data.

Moreover, I am indebted to Dr. Joanna Napp, who did a great job in motivating and directing me towards the last months of this project.

The endeavor of such a study, would have not been certainly possible without the practical help of many people for whose support I am very grateful: Roswitha Streich, Mercedes Martin-Ortega, Sarah Garbode, Sabine Wolfgramm, Bettina Jeep and Hanna Puchala. But among all, the one who really made these results possible, is Bärbel Heidrich, who gave me a tremendous help and support during the whole 4 years of my project. Not only regarding work but also at personal level. Herzliches Dankeschön, Bärbel!
Together with them, I would also like to thank all the members of the AG Alves, especially Dr. Andrea Markus and Dr. Christian Dullin, for the great help during the submission of the thesis, and Dr. Fernanda Ramos Gomes, for her constant inspiring happiness.

I would also like to thank Prof. Dr. Reshkin, together with his group from University of Bari, for the nice collaboration we planned together, and for being so helpful during the thousands of skype calls that I required. He was always available to discuss my research and willing to help with even the smallest of problems. Grazie mille Professore!

This study was financially supported by “IonTrac” EU - project. It was a pleasure to share that experience with so many different PhDs around Europe. One especially turned out to be not only a great colleague but also an amazing friend: Grazie Andrea!
Together with Andrea Giannuzzo, I owe thanks to his supervisor, Prof. Dr. Ivana Novak, for hosting me during my secondment in Copenhagen and for the nice collaboration that we have established.

Then, a big thanks goes to all my friends I have met along the last 4 years here in Göttingen. My flatmates, Eva and Marco, the PizzaPasta group, with whom I shared some of the best moments ever here in Göttingen, and the MonsterParty Group. Among them, a big thanks goes to Giulia Poggi, semplicemente perchè sei come sei!

But moreover and most importantly, I want to thank the 3 most important person I have in my live, who have encourage and support me every single day (thanks skype!) during the entire course of my PhD: Un grazie infinito ai miei genitori e a mia sorella Giulia, che OGNI SINGOLO GIORNO di questo dottorato mi hanno spronato ad andare avanti fino ad ottenere un simile risultato.
Un sincero grazie va anche alle mie zie Luciana e Mara per avermi fatto sempre sentire la loro vicinanza e il loro supporto.

And finally, the biggest “thank you” and gratitude goes to my ‘better half’, who has supported me along this last 4 years, being constantly at my side and always there in case of need, despite we liveD so far from each other. Ti dedico questo traguardo, Paolo. Grazie di cuore!

Abstract

Pancreatic cancer has the poorest survival rate of the most common types of cancers with a 5 year survival rate of only 3-5% after diagnosis. Since there has been no significant improvement in the clinical outcome for several decades, there is an urgent need for novel concepts in the understanding of the pathophysiology, diagnosis and treatment of PDAC.

Therefore, the aim of the study was to characterize the *in vivo* tumor progression and metastatic behavior of PDAC orthotopic mouse models, developing PDAC tumors with different grades of differentiation and to assess novel imaging strategies as well as a new combination therapy in some of these models.

To this end, PDAC xenografts were extensively characterized after orthotopic transplantation of five different human PDAC cell lines with known grade of differentiation (AsPC-1, MIA PaCa-2 and PANC-1 as poorly differentiated, BxPC-3 as moderately differentiated and Capan-1 as well differentiated) in the head of the pancreas of nude mice. Tumors that developed in each mouse model showed distinct tumor take rates and different time of tumor development, independently from the grade of differentiation. All of them presented with invasion into the stomach and duodenum, resembling the classic features of PDAC progression in humans. The differentiated tumors were composed of tumor cells organized in duct-like clusters (Capan-1), as seen in humans, and in round clusters (BxPC-3), whereas the poorly differentiated tumors (AsPC-1, MIA PaCa-2 and PANC-1) showed a typical unorganized morphology. Moreover, by analyzing the presence of PSCs and collagen deposition, in each PDAC mouse model different degrees of a desmoplastic reaction, another hallmark of human PDAC, were observed. Similar to human PDAC, high amounts of collagen fibers around the duct-like cell clusters were only found in Capan-1 tumors.

Two EGFR expressing PDAC models, AsPC-1 and MIA PaCa-2, were applied for testing the suitability of near-infrared fluorescent (NIRF) labeled Cetuximab, a therapeutic monoclonal antibody targeting the human epidermal growth factor receptor (EGFR), as a new tool for fluorescence-guided surgery (FGS). Distribution and binding of systemically injected Cetuximab Alexa Fluor 647 conjugate (Cetux-Alexa-647) and the co-injected control human IgG Alexa 750 conjugate (hIgG-Alexa-750) (25 µg each) were studied over 48 h by NIRF imaging (Optix MX2 and IVIS) in mice bearing orthotopic AsPC-1 and MIA PaCa-2 tumors. Results obtained here showed that Cetux-Alexa-647 but not the control hIgG-Alexa-750 fluorescence was specifically detected *in vivo* and *ex vivo* in the primary pancreatic tumors and metastases as small as 1 mm, with maximum intensities at 24 h.

LT analysis and NIRF microscopy of tumor sections confirmed the binding specificity of Cetux-Alexa-647 to PDAC cells, whereas a multimodal approach applying 3D NIRF imaging and CT of AsPC-1 mice receiving both, the Cetux-Alexa-647 and iodine containing CT contrast agent, confirmed that the Cetux-Alexa-647 signal localized at the primary pancreatic tumor in correlation with the anatomical structure of the mice. Moreover, during fluorescence-guided dissection, performed 24 h after injection of the probe using the Quest Spectrum clinical device for FGS, Cetuximab conjugated to IRDye-800CW (Cetux-800CW) enabled fast and straightforward real time delineation of AsPC-1 tumor margins and also of small metastases. Odyssey scans revealed that only the vital part of the tumor, but not the necrotic part, was stained with Cetux-800CW. Tumor cells invading into the stomach and duodenum were also detected. Moreover, *ex vivo* scans of organs with detected metastases during fluorescence-guided dissection, also revealed high signals only at the metastatic sites and not in the healthy tissue. Taken together, NIRF labeled Cetuximab might be a promising tool for the visualization of tumor margins and metastatic sites during FGS, allowing a precise surgical resection and consequently aiding the decrease of disease recurrence.

Finally, a combination of Erlotinib, a TKi of EGFR, and Cariporide, a specific inhibitor of NHE1, was tested *in vivo* in the highly metastatic AsPC-1 mouse model to determine their effect on tumor growth, invasion and metastatic spread. 10 days after cell transplantation AsPC-1 mice were divided in 4 groups and treated for 20 days with Erlotinib (50 mg/kg) or Cariporide (3 mg/kg) only or with the combination of both. The control group received saline solution and Captisol 6%. Primary tumor and tumor spread in different peritoneal organs (liver, spleen, kidney, diaphragm, mesentery and site of surgical incision) were analyzed. Quantification of the metastatic spread was difficult to obtain, due to the low number of metastatic findings in each organ and to the high variation of the data within each treated group. However, Erlotinib/Cariporide-double treated mice presented with less metastatic spread to different organs such as liver, kidney and mesentery, and tumor infiltration of the site of surgical incision. Moreover, Erlotinib/Cariporide-double therapy showed a slight but no significant inhibitory effect on tumor growth as compared to controls, and decreased the grade of tumor infiltration in the stomach. Individual therapies with either Erlotinib and Cariporide did not show any therapeutic response, neither to tumor growth nor to tumor invasion in the stomach, but the metastatic spread to the kidney (Erlotinib treated group) and to the diaphragm (Cariporide-treated group) was slightly reduced. Taken together, this study provides a preclinical proof-of-concept for a novel anti-metastatic activity of Erlotinib/Cariporide-double therapy based on the inhibition of both, EGFR, whose overexpression usually correlates with an advanced cancer disease, and NHE1, a protein interconnected with the EGFR downstream signaling and implicated in the pH regulation of cell invasion.

List of Figures

Figure 1: 1
Figure 2: 2
Figure 3: 3
Figure 4: 7
Figure 5: 10
Figure 6: 11
Figure 7: 14
Figure 8 : 30
Figure 9: 39
Figure 10: 41
Figure 11: 43
Figure 12: 44
Figure 13: 45
Figure 14: 46
Figure 15: 48
Figure 16: 50
Figure 17: 51
Figure 18: 52
Figure 19: 53
Figure 20: 54
Figure 21: 55
Figure 22: 57
Figure 23: 58
Figure 24: 59
Figure 25: 60
Figure 26: 61
Figure 27: 62
Figure 28: 63
Figure 29: 66

List of Tables

Table 1: 5
Table 2 : 29
Table 3: 31
Table 4: 32
Table 5: 34
Table 6: 36
Table 7: 65

List of Abbreviations

AEC	3-Amino-9-ethylcarbazole
BCA	Bicinchoninic acid
BSA	Bovine serum-albumin
CA 19.9	Carbohydrate antigen 19.9
CCD	Coupled charge device
Cetux-Alexa-647	Cetuximab Alexa Fluor 647 conjugate
Cetux-800CW	Cetuximab conjugated to IRDye-800CW
CT	Computed tomography
DAPI	4',6-diamidino-2-phenylindole
DEPC	Diethylpyrocarbonat
DICOM	Digital Imaging and COmmunications in Medicine
DMEM	Dulbecco's Modified Eagle Medium
DMEM/F-12	Dulbecco's Modified Eagle Medium supplemented with Nutrient Mixture F-12
DMSO	Dimethy sulfoxide
ECM	Extracellular matrix
EDTA	Ethylene-diamine-tetraacetic acid
EGFR	Epidermal growth factor receptor
EPR	Enhanced permeability and retention
FCS	Fetal calf serum
FDA	Food and Drug Administration
FGS	Fluorescence-guided surgery
FLIT	Fluorescence Imaging Tomography
FOV	Field of view
FMT	Fluorescence molecular tomography
FRI	Fluorescence Reflectance Imaging
h	Hour
H^+	Proton
Hb	Hemoglobin
HbO_2	Oxygeneted hemoglobin
HE	Hematoxylin-Eosin
hIgG-Alexa-750	Human IgG Alexa 750 conjugate
HNSCC	Head and neck squamous-cell carcinoma
HRP	Horseradish peroxidase

ICG	Indocyanine green
i.e.	id est (that is)
IHC	Immunohistochemistry
IMDM	Iscove's modified dulbecco's medium
i.p.	Intraperitoneal
i.v.	Intravenous
kDa	Kilodalton
KRAS	V-Ki-ras2 Kirsten rat sarcoma viral oncogene homolog
$KRAS^{mut}/KRAS^{wt}$	KRAS mutated and KRAS wild type
KVp	Kilovoltage peak
LT/LTs	Lifetime/Lifetimes
MB	Methylene blue
MMPs	Matrix metalloproteinases
MRI	Magnetic resonance imaging
MUC-1	Mucin-1
NC	Normalized count
NHE1	Sodium–hydrogen exchanger 1
NIR	Near-infrared
NIRF	Near-infrared fluorescent
ns	nanosecond
NSCLC	Non-small cell lung cancer
PBS	Phosphate buffered saline
PDAC	Pancreatic ductal adenocarcinoma
PET	Positron emission tomography
PFA	Paraformaldehyde
pHe	Extracellular pH
pHi	Intracellular pH
PSCs	Pancreatic stellate cells
RIPA	Radioimmunoprecipitation assay
ROI	Region of interest
rpm	Rounds per minute
RPMI-1640	Roswell Park Memorial Institute medium-1640
RT	Room temperature
SDS	Sodium dodecyl sulfate
SDS-PAGE	Sodium dodecyl sulfate-polyacrylamide gel electrophoresis

SPECT	Single photon emission computed tomography
SRA	Sample reducing agent
TBS	TRIS buffered saline
TBST	TRIS buffered saline containing Tween-20
TGFα	Transforming growth factor alpha
TK	Tyrosine kinase
TKi/TKIs	Tyrosine kinase inhinbitor/Tyrosine kinase inhibitors
TPSF	Temporal point spread function
TRIS	Trishydroxymethylaminomethane
US	Ultrasound
2D	Two Dimensional
3D	Three Dimensional
5-ALA	5-aminolevulinic acid
α-SMA	α-smooth muscle actin
µA	microampere
µCT	micro CT
µg/mg/gr/kg	microgram/milligram/gram/kilogram
µl/ml	microliter/milliliter
µm/mm/cm	micrometer/millimeter centimeter

1. Introduction

1.1 Anatomy and physiology of the pancreas

The pancreas is a combined endocrine and exocrine gland deeply located in the upper-retroperitoneal cavity. It can be divided into four parts: head, neck, body, and tail. In humans, the pancreatic head, located on the right of the superior mesenteric vein, is closely associated with the pyloric antrum and the upper part of the duodenum, through the pancreatic duct. The pancreatic neck is the constricted portion to the left of the head, whereas the body and tail of the pancreas are located on the left side of the abdomen behind the stomach in the proximity of the spleen (Figure 1).

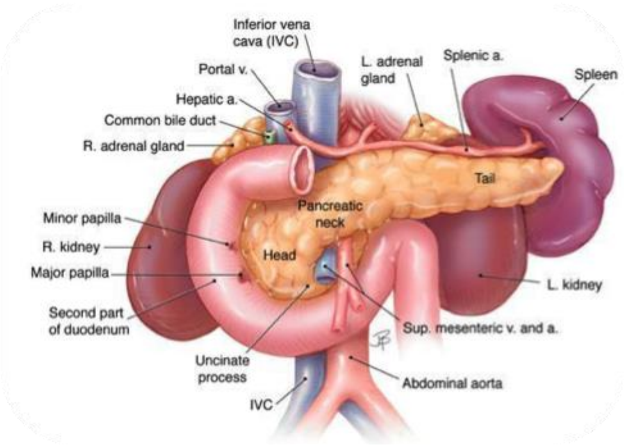
Inferior vena cava (IVC)
Portal v.
L. adrenal gland
Splenic a.
Spleen
Hepatic a.
Common bile duct
R. adrenal gland
Tail
Pancreatic neck
Minor papilla
R. kidney
Head
Major papilla
L. kidney
Second part of duodenum
Sup. mesenteric v. and a.
Uncinate process
Abdominal aorta
IVC

Figure 1: Anatomical localization of human pancreas. The pancreas is located posterior and inferior to the stomach on the left side of the abdominal cavity. It extends laterally and superiorly across the abdomen from the curve of the duodenum to the spleen. Figure taken from Longnecker [1].

Functionally, the pancreas is a complex organ consisting of a combination of different cell lineages: an endocrine portion that is arranged as discrete islets of Langerhans, involved in the regulation of metabolism and glucose homeostasis, and an exocrine part that consists of acinar cells synthesizing and secreting digestive enzymes concentrated into a bicarbonate rich fluid that is drained into the small intestine by a complex duct system [2].

1.2 Pancreatic Ductal Adenocarcinoma (PDAC)

Each cell type forming pancreas can potentially lead to cancer formation. Depending on the cell origin of the tumor, pancreatic cancer can be divided in two main groups: cancers that occur in the exocrine part of the pancreas and those that occur in the endocrine one. Tumors of exocrine pancreas are far more common accounting for 95% of all cases, developing in glands or ducts of the exocrine pancreas, where digestive juices are produced. Pancreatic ductal adenocarcinoma (PDAC) typically affects people in their late adult life with 80% of PDAC arising between the ages of 60 and 80 whereas it is extremely rare in young people (< 40 years) [3] and more prevalent in males than in females [4]. PDAC is the fourth leading cause of cancer death in men and women in western societies, with a 5-year survival rate of less than 5% [5]. This extremely poor prognosis is largely attributed to its propensity for early local infiltration into surrounding organs including stomach and duodenum, to peritoneal metastases into the liver and spleen and distant metastases into the lymphatic system and lungs [6-8]. The most common symptoms of PDAC include abdominal pain, weight loss, digestive problems and chronic fatigue, whereas jaundice is the most common clinical sign. Since the presenting signs and symptoms can be caused by multiple other conditions, PDAC is often overlooked during differential diagnosis or develops asymptomatically at early stages. Therefore, the diagnosis usually occurs in the late onset of the disease, when it has already disseminated to surrounding or distant organs and vessels [9].

1.2.1 Desmoplastic reaction

Although PDAC shows a highly aggressive behavior, histologically it usually appears well differentiated, comprising a well formed tubular or duct-like structure with cuboidal epithelium. However, varying degrees of cellular atypia and differentiation are also common features [10]. PDAC is one of the most stroma-rich cancers, characterized by a remarkable increase in fibrotic tissue that infiltrates and envelopes the neoplasm, referred to as the desmoplastic reaction. The resulting fibrosis is composed of a dynamic assortment of extracellular matrix (ECM) components, such as collagen type I and other glycoproteins, and non-neoplastic cells including fibroblastic, vascular and immune cells, which often can even outnumber the tumor cells (Figure 2) [11].

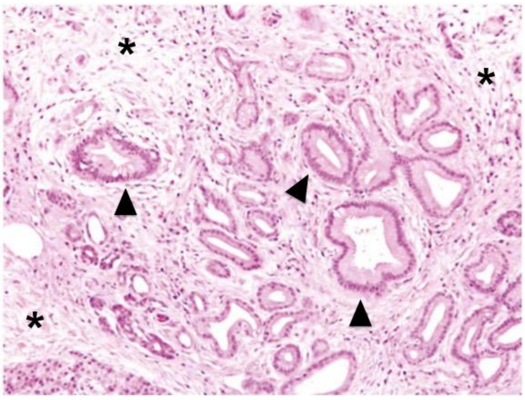

Figure 2: Desmoplastic reaction of human PDAC. Hematoxylin and eosin stained section of a human PDAC showing tumor elements (black arrows) embedded in an abundant collagenous stroma (asterisks). Figure taken from Xu et al. [12].

There is now unequivocal evidence that fibrosis of PDAC is mainly produced by pancreatic stellate cells (PSCs). PSCs are fibroblast-like cells residing in the exocrinal areas of the pancreas in a quiescent status and are activated during the pathogenesis of

PDAC. When activated, PSCs assume a myofibroblast phenotype and exhibit expression of the cytoskeletal protein α-smooth muscle actin (α-SMA) [13]. Substantial evidence indicates that PSCs interact closely with cancer cells to modulate their proliferation and migration and play an important role in the chemoresistance of PDAC as well as in the immune evasion and tumor recurrence [13].

1.2.2 Treatment

1.2.2.1 Early stage disease

Only 10-15% of the PDAC cases have localized disease (tumor at stage I or II) and can therefore undergo a resection procedure. For this, depending on the tumor location and type, different surgical resections are considered: pancreatoduodenectomy, or Whipple procedure (Figure 3), is preferred for tumors of the head of pancreas, distal pancreatomy for tumors located in the tail of the pancreas or a total pancreatectomy for large cystic lesions.

Within patients that underwent resection, the incidence of the so called R1-resection (microscopical presence of tumor cells at the resection margins) is quite high and varies considerably in the literature ranging from <20% to >80% [14, 15] meaning that microscopically positive tumor margins remain after surgical resection resulting in a high risk of local tumor recurrence. Therefore, after surgery, PDAC patients usually receive an adjuvant chemotherapy to improve the progression-free survival [16], but the overall survival is only marginally affected [17].

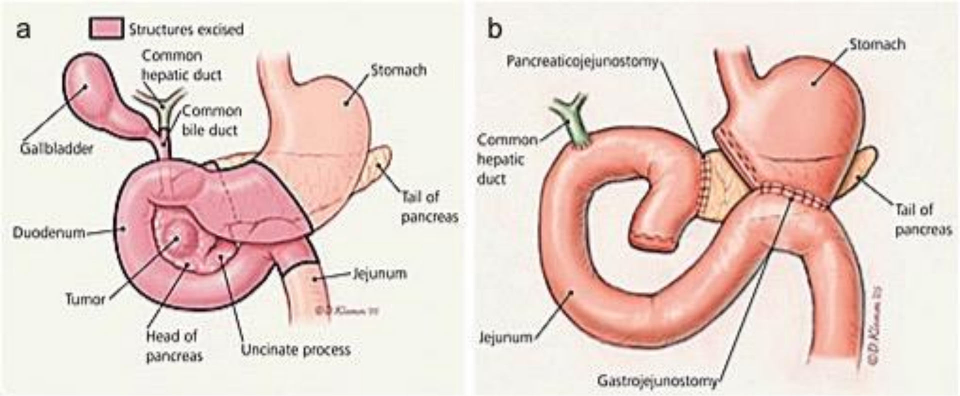
a
Structures excised
Common hepatic duct
Common bile duct
Gallbladder
Stomach
Tail of pancreas
Duodenum
Jejunum
Tumor
Head of pancreas
Uncinate process
b
Pancreaticojejunostomy
Stomach
Common hepatic duct
Tail of pancreas
Jejunum
Gastrojejunostomy

Figure 3: The Whipple procedure. Anatomical view before (a) and after (b) the surgical intervention; note the anastomosis of the hepatic duct and the remaining pancreas and stomach to the jejunum (b). Figure taken from Freelove and Walling [9].

1.2.3.2 Locally advanced and systemic PDAC

Most of the patients that are diagnosed with PDAC (~80% of the cases) present with a locally advanced or metastatic disease (tumors at stage III and IV) and are consequently not suitable for surgery. Over the two last decades, the first-line therapy for these patients has been the chemotherapeutic agent gemcitabine, a pyrimidine analog, administered as monotherapy [18]. However, since numerous patients do not respond to gemcitabine therapy due to chemoresistance [19], chemotherapeutic alternatives have been tested and only a few have been proven to provide significant prolongation of overall survival rates [20]. Among them, FOLFIRINOX (combination of oxaliplatin, irinotecan and 5-FU with leucovorin) is now considered as the most promising combination chemotherapy, which achieves a significant survival benefit for patients (from 6.8 months with gemcitabine alone to 11.1 months with FOLFIRINOX), at the expense though of an extremely high toxicity. Therefore, it is suitable only for patients with a good performance status [21].

In addition to chemotherapies, several studies testing specific therapeutic compounds (i.e. monoclonal antibodies or small molecules) in combination with gemcitabine have been performed [22]. Among all, only Erlotinib (Tarceva), an inhibitor of the tyrosine kinase (TK) activity of epidermal growth factor receptor (EGFR), increased the overall survival of PDAC patients from 5.91 to 6.24 months when combined with gemcitabine monotherapy and was approved as first-line therapy of PDAC [23].

However, neither FOLFIRINOX nor the Erlotinib/Gemcitabine combination improves the overall survival by much and therefore, new therapeutic approaches are in high demand for PDAC.

1.3. Orthotopic PDAC mouse models

Mouse PDAC models have been crucial for a better understanding of the molecular mechanisms regulating the development of PDAC, as well as its prevention, diagnosis and treatment. One of the most widely used animal models in oncology is the human tumor xenograft in immunodeficient mice. Orthotopic transplantation of tumor cells in the corresponding organ of the mouse, e.g. PDAC cells into the pancreas, results in a tumor formation comparable to the one observed in humans in terms of tumor morphology, expression of tumor markers, presence of desmoplastic reaction, invasiveness and metastatic spread to distant organ such as lymph nodes and lungs [24-26].

In order to avoid rejection of the transplanted human cells/tissue by the immune system of the host mouse, these models require the use of totally or partially immunodeficient mice such as athymic nude mice that are characterized by a genetic spontaneous mutation of the Foxn1$^{nu/nu}$ gene responsible for the maturation of the thymus gland. Therefore, these mice are unable to produce mature T cells and consequentially lack cell-mediated immunity whereas the innate response remains intact. Moreover, these mice are hairless and therefore they are extremely useful and practical for optical imaging studies.

1.4. Molecular imaging for tumor monitoring in preclinical models

The *in vivo* evaluation of the suitability of novel diagnostic tumor markers as well as the efficacy of novel therapeutic strategies by imaging over time is of growing interest. Imaging strategies with CT (computed tomography), MRI (magnetic resonance imaging) and US (ultrasound), are mainly employed to detect anatomical structures of the body including internal organs. Nuclear imaging including SPECT (single photon emission computed tomography) and PET (positron emission tomography), and optical imaging including fluorescence and bioluminescence imaging, are considered as functional imaging, since they are able to assess molecular processes such as physiological or metabolic activities *in vivo* [27]. The choice of a particular imaging technology for a particular research depends on different factors required for the study such as imaging frequency, field of application and required spatial resolution. Since each imaging technique has unique advantages and limitations (Table 1), in general they are more complementary than competitive, and researchers increasingly combine them [28].

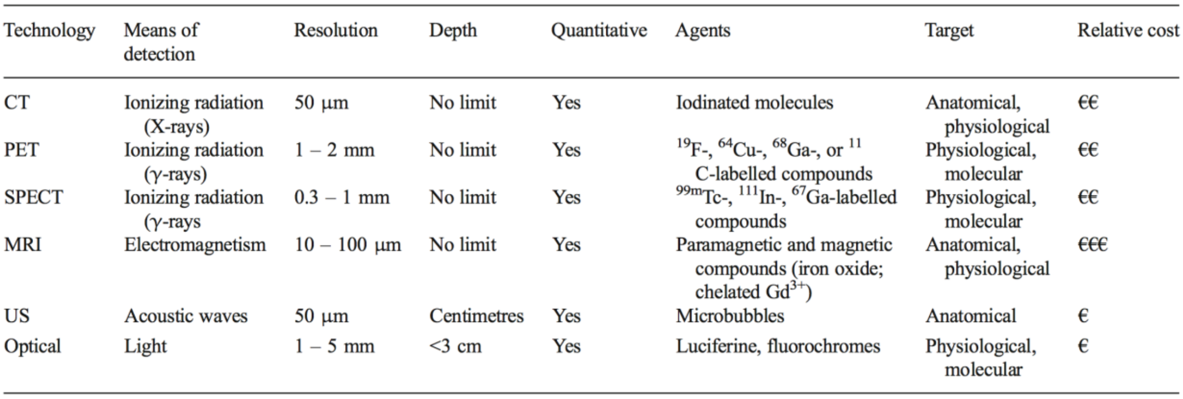

Technology	Means of detection	Resolution	Depth	Quantitative	Agents	Target	Relative cost
CT	Ionizing radiation (X-rays)	50 µm	No limit	Yes	Iodinated molecules	Anatomical, physiological	€€
PET	Ionizing radiation (γ-rays)	1 – 2 mm	No limit	Yes	^{19}F-, ^{64}Cu-, ^{68}Ga-, or ^{11}C-labelled compounds	Physiological, molecular	€€
SPECT	Ionizing radiation (γ-rays	0.3 – 1 mm	No limit	Yes	^{99m}Tc-, ^{111}In-, ^{67}Ga-labelled compounds	Physiological, molecular	€€
MRI	Electromagnetism	10 – 100 µm	No limit	Yes	Paramagnetic and magnetic compounds (iron oxide; chelated Gd^{3+})	Anatomical, physiological	€€€
US	Acoustic waves	50 µm	Centimetres	Yes	Microbubbles	Anatomical	€
Optical	Light	1 – 5 mm	<3 cm	Yes	Luciferine, fluorochromes	Physiological, molecular	€

Table 1: Overview of characteristic features of different *in vivo* small-animal imaging modalities. Each modality is characterized by specific detection modality, resolution, penetration depth, agents employed, field of study and cost. Most imaging modalities are used clinically and can be translated from animals to humans in the drug development process. Table taken from Bersen et al. [27].

1.4.1 Computed tomography

To date, CT is the workhorse of anatomical imaging not only in clinical but also in preclinical oncology since it is fast, cost-effective, non-invasive and obtains high resolution images. It consists of an X-ray source and X-ray detectors between which the subject is placed. Most systems commonly use cone-beam X-ray source and solid-state detectors that rotate around the animal to produce projections of X-ray attenuation through the body at many different angles [29]. Then, CT makes use of computer-processed combinations of the multiple X-ray images taken to produce cross sectional images of the scanned area. Digital geometry processing of the radiographic images can further be used to generate a three dimensional (3D) view of the region of interest (ROI) [30]. To assess tumor growth by CT, the use of iodine containing contrast agents is necessary as tumors without contrast agents can generally not be distinguished from their surrounding soft tissues.

1.4.2 *In vivo* fluorescence imaging

In vivo fluorescence imaging of small animals is unequivocally the most versatile visualization modality, which is increasingly employed across the drug development process, particularly in the oncology/cancer therapeutic area. One of the main applications is monitoring the treatment response for early indications of efficacy.

1.4.2.1 Fluorescent labels for *in vivo* NIRF imaging

Fluorescence is the property of certain molecules to absorb light at one wavelength and to emit light at a longer wavelength [31]. It takes place when an orbital electron of the molecule interacting with a photon, absorbs its energy and thereby is excited to a higher quantum state. Since this state is unstable, the electron relaxes back to its ground state by emitting fluorescence light [32]. Today, fluorophores in many colors exist that fluoresce from deep blue (~400 nm) in the visible spectrum to far red (~900 nm). Of particular advantage for optical imaging in animals are fluorophores absorbing and emitting in the near- infrared (NIR) wavelength region of 700 to 900 nm. The advantage of this spectral range is not only a decreased autofluorescence, when compared to the blue range (400-500 nm), but also less absorbance occurs by components of the blood such as haemoglobin and water (Figure 4). For this reason, NIRF imaging enables the best penetration of light into the tissue, and fluorophores that absorb in this window are preferably used for *in vivo* fluorescence imaging [33].

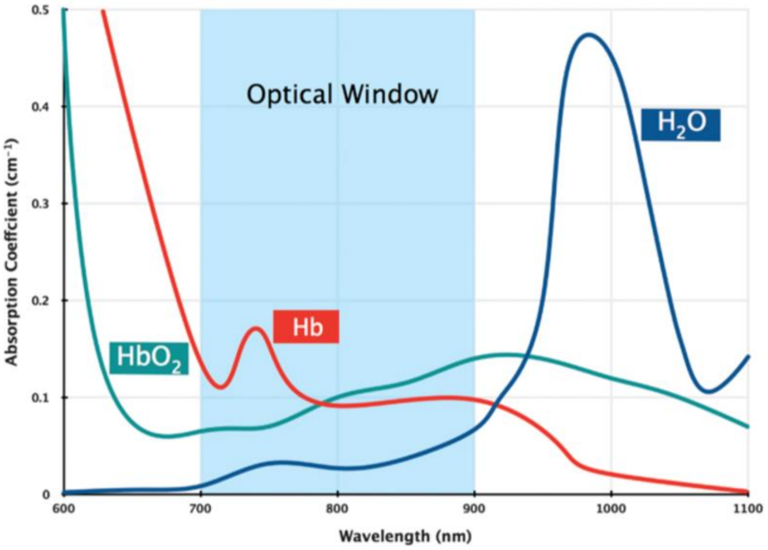

Figure 4: Tissue optical window. The absorption (illustrated as absorption coefficient) by major light absorbers in tissue is illustrated at distinct wavelengths. In the optical window (700 to 900 nm; light blue) absorption by hemoglobin (Hb), oxygenated hemoglobin (HbO$_2$), and water (H$_2$O) is low. Figure taken from Phan et al. [34].

Fluorescent probes for *in vivo* imaging can be divided in three groups, i) non-targeted or unspecific contrast agents, ii) targeted labels, depending on their association to a specific ligand directed against disease relevant molecules, and iii) activatable probes.

Non-targeted tracers are characterized by a sufficiently long blood circulation time and are mainly designed for imaging of blood vessels or blood vessel leakiness. Three unspecific NIR fluorophores available in the clinic are: indocyanine green (ICG), methylene blue (MB) and 5-aminolevulinic acid (5-ALA). The clinically most used NIRF dye is ICG, a tricarbocyanine dye, which is FDA approved since 2006 for cerebral and retinal angiography and for liver clearance in humans. Furthermore, ICG has been shown to be a valid alternative to radiotracers in sentinel lymph node mapping in different types of cancers [35]. The enhanced permeability and retention (EPR) effect that involves hyperpermeable and leaky vasculature in tumors, as well as suppression of lymphatic function allows unspecific probes to extravasate passively, accumulate in the tumor tissue and therefore be suitable for tumor studies (i.e. fluorescence-guided surgery (FGS).

In order to improve the accumulation of fluorescent contrast agents in a specific area of interest, NIR- fluorochromes are often conjugated to ligands, such as antibodies, antibody fragments (nanobodies or single chain antibodies), or small peptides, which interact with a specific molecular target. The probes that bind are retained at the target site (i.e. tumor), while non-bound probes are cleared from the circulation.

1.4.2.2 The principle of *in vivo* fluorescence imaging

In vivo fluorescence imaging is mostly based on the detection of the fluorescence emission from fluorophores, after excitation at a distinct wavelength, in small living animals. Different devices for NIRF imaging are currently available on the market. Most of them are equipped with a multispectral light source or a laser for excitation of the fluorescent probe, appropriate filters to set the desired excitation light as well as to collect the fluorescence emission light, and a detector, which is usually either a coupled charge device (CCD) camera or a photomultiplier tube. The most common method to record fluorescence deeper from the tissues is associated with planar measurements, which are usually overlaid with photographic images of the surface of the scanned sample. Planar imaging can be performed either in an epi-illumination mode, also called fluorescence reflectance imaging (FRI), as well as in transillumination mode, based on the reciprocal position of the excitation source and the detector used in relation to the scanned object. These are located on the same side of the object in the case of the epi-illumination mode, whereas when the excitation source and the detector are placed on the opposite sides of the scanned animal, imaging is performed in a trans-illumination mode, in which the light penetrating the object is collected [36]. One of the most recent progressions in NIRF imaging was the development of tomographic fluorescence imaging, including fluorescence molecular tomography (FMT), which requires reconstruction with sophisticated image processing algorithms, providing 3D images of the fluorescence biodistribution in the whole animal as well as the precise information about the probe concentration and depth [37].

Although NIRF imaging has a limited tissue penetration depth of ~1 cm, it offers several advantages in comparison to other functional imaging technologies, like SPECT or PET. It has a high spatial resolution, producing fast and real time measurements with relatively low cost. Moreover, it is a highly sensitive technique enabling the detection of fluorophore of picomolar or even femtomolar concentrations [38]. Unlike SPECT or PET, a unique characteristic of fluorescence imaging is the spectral unmixing analysis, which is able to distinguish between several applied fluorescence labels injected simultaneously and differing in their emission excitation. Time-domain NIRF imaging is also a well establish method for studying the emission dynamics of the fluorescent molecules. This approach employs pulsed laser diode as an excitation source, and is able to measure time-resolved the emitted photons from the object after each single excitation pulse using a photomultiplier tube. Thus, the lifetime (LT), characterizing specifically each fluorescent probe by describing the average time it spends in the excited state before returning to the ground state, can be calculated over a specific area of the scan. This permits the identification of probe-derived signals *in vivo* [39].

1.5 Fluorescence-guided surgery

Along with the application in small animal research, NIRF imaging is obtaining more and more interest in clinic translation. Due to the low tissue penetration of fluorescent light, one of its most promising use in the clinic is image-guided open surgery or laparoscopy, e.g. for real time fluorescence guidance for tumor resection in order to minimize the R1 positive tumor margins [40]. In fact, the high sensitivity of NIR fluorescence imaging potentially allows the visualization of a very low number of tumor cells on the surface of a tissue (i.e. margin positivity), otherwise only detected by histopathological analysis. Different intraoperative imaging systems (SPY, Artemis and FLARE) for open surgery (Figure 5a) or laparoscopy (Figure 5b) are available in the clinic [40]. Using these systems, NIRF contrast agents can be visualized with acquisition times in the millisecond range (Figure 5c) enabling real-time guidance during surgery. The NIR light used for monitoring the fluorescence probes is invisible to the human eye, thus not altering the look of the surgical field [41]. Moreover, since it does not require the handling of ionizing radiation, it can be considered as a relative safe technique. While no standardized protocol for fluorescence guidance exists as yet in the routine applied for oncologic surgery, clinical trials have been lately conducted in patients using ICG, 5-ALA and MB for guidance during the resection of liver metastases, glioma and a fibrous tumor of the pancreas, respectively [42-44], providing, in some cases, a modest and useful contrast to distinguish the tumor lesions from normal tissue. However, all these probes lack sufficient reliability regarding specificity and histopathologic accuracy to establish a consistent real-time assistance during surgery. In some cases, where fluorescence was reported, the difference between tumor and background fluorescence was hardly detectable [45]. Therefore, there is a high demand for novel specific fluorescence targeting approaches in order to obtain a more precise intraoperative visualization of the tumor tissue.

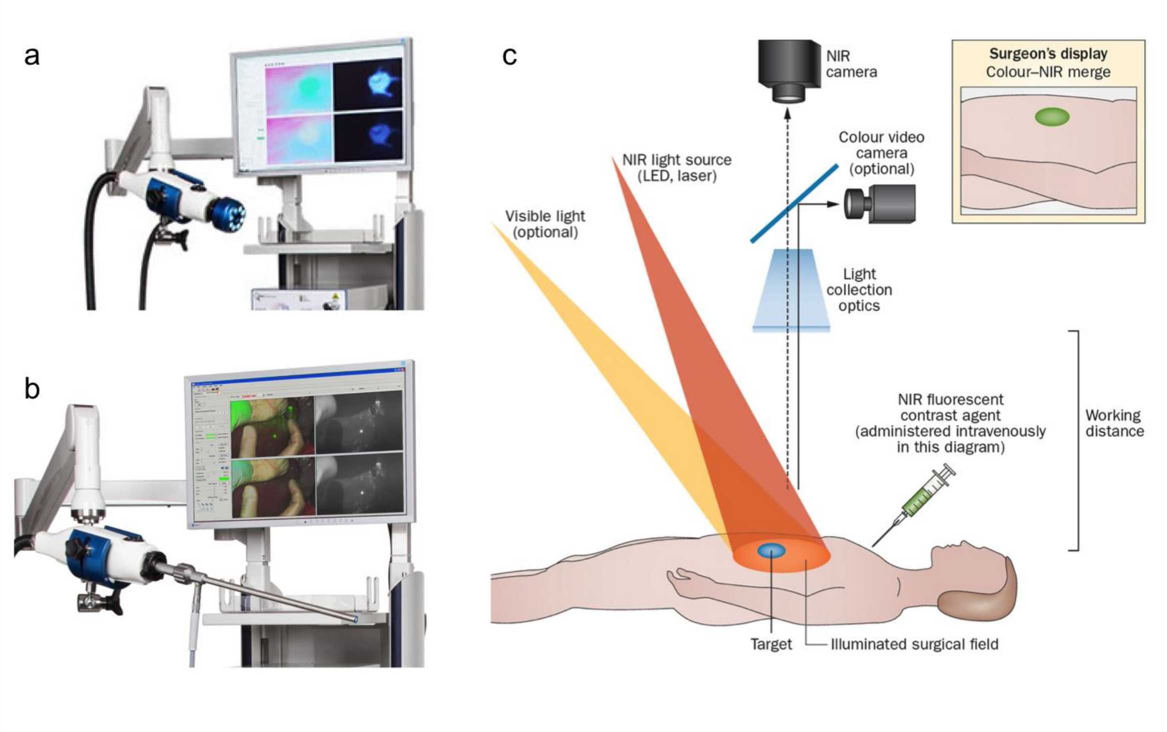
a
b
c
NIR camera
Surgeon's display
Colour–NIR merge
Colour video camera (optional)
NIR light source (LED, laser)
Visible light (optional)
Light collection optics
NIR fluorescent contrast agent (administered intravenously in this diagram)
Working distance
Target
Illuminated surgical field

Figure 5: The approach for fluorescence-guided surgery. Different NIR fluorescence imaging systems are available for open surgery (a) or for minimally-invasive laparoscopy (b). (c) For FGS, a NIR fluorescent contrast agent is administered intravenously, topically, or intraparenchymally before surgery. During surgery, the agent is visualized using adequate NIR excitation light, collection optics and filtration, and a camera sensitive to NIR fluorescence emission light. Figures adapted from Vahrmeijer et al. [35] and Quest web site (http://www.quest-mi.com).

1.6 Targeting EGFR and NHE1 in cancer

Today, one of the most promising approaches to detect or treat tumors involves strategies targeting tumor associated antigens over-expressed on tumor cells. These antigens are usually easily accessible targets, located preferentially on the cell membrane, such as mucins, growth factor receptors (i.e. EGFR), ion-channels, or cell-adhesion molecules (i.e. integrin receptors) [27, 46, 47].

1.6.1 The role of EGFR in cancer

A well-known biomarker of various cancer types is the human EGFR, also called ErbB1 or HER1. It is overexpressed in up to 90% of pancreatic cancers [48] and in many other human cancers including head and neck squamous-cell carcinoma (HNSCC), colorectal and brain cancer [49].

EGFR is a transmembrane 170 kDa glycoprotein belonging to the four-member ErbB1-4 family of tyrosine kinase growth factor receptors. All of them share the same structure composed of an extracellular domain, a hydrophobic transmembrane region and a tyrosine kinase-containing cytoplasmic region. Binding of EGF or transforming growth factor alpha (TGFα), which are the most important endogenous ligands for EGFR, to its extracellular region, promotes major domain reorganization and conformational changes, that permit it to dimerize with other receptors of the family [50]. Dimerization results in receptor autophosphorylation and further activation of the downstream signaling cascades, including Ras-ERK, phosphoinositide-3 kinase and STAT, which are all associated with cell growth, proliferation, survival, cell motility, and angiogenesis [51]. Due to the increasing knowledge of the structure and function of EGFR and of its role in the initiation and progression of various cancers, many efforts have been made in the development of new anticancer therapies targeting EGFR.

Selective compounds have been developed targeting either the extracellular ligand-binding region of the EGFR using e.g. monoclonal antibodies, immunotoxins and ligand-binding cytotoxic agents, or the intracellular tyrosine kinase region through the employment of small molecules tyrosine kinase inhibitors (TKIs) [52]. Among them are monoclonal antibodies, such as Cetuximab or Panitumumab, and TKIs, such as Erlotinib, Gefitinib (Figure 6), both currently applied in the clinic.

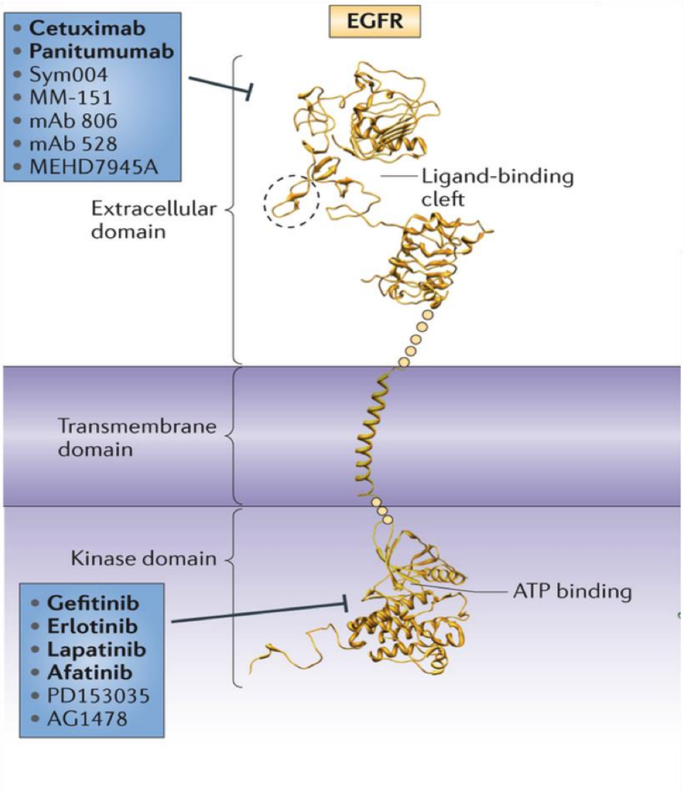
• **Cetuximab**
• **Panitumumab**
• Sym004
• MM-151
• mAb 806
• mAb 528
• MEHD7945A
EGFR
Ligand-binding cleft
Extracellular domain
Transmembrane domain
Kinase domain
ATP binding
• **Gefitinib**
• **Erlotinib**
• **Lapatinib**
• **Afatinib**
• PD153035
• AG1478

Figure 6: Inhibition of EGFR. Therapeutic antibodies and tyrosine kinase inhibitors (blue boxes) are directed against the ligand-binding cleft in the extracellular domain and to the intracellular kinase domain, respectively. Bold-written drugs have been FDA-approved. Figure adapted from Tebbutt et al. [53]

1.6.1.1 Cetuximab as antibody-based targeting of EGFR

Cetuximab (Erbitux) is a chimeric human/mouse monoclonal antibody (150 kDa) that specifically binds to the extracellular domain of human EGFR, competing with the natural ligands (EGF and TGFα). It has a similar or even higher affinity for the EGFR than the natural ligands, and effectively blocks the ligand-induced signaling cascade [54]. There is evidence suggesting that, after binding to EFGR, Cetuximab promotes its internalization by endocytosis and its further lysosomal degradation, leading to an overall downregulation of the number of EGFRs expressed on the surface of the cells [53]. Cetuximab is currently approved as a single agent or in combination with radiation therapy for the treatment of HNSCC, and as a single agent or in combination with chemotherapy for the treatment of colorectal carcinoma [55].

1.6.1.2 Erlotinib as tyrosine kinase inhibitor of EGFR

Erlotinib (Tarceva) is a low-molecular weight reversible EGFR TKI. However, it has been recently demonstrated that it targets several kinases and should therefore be considered as a multikinase inhibitor [56]. Due to its much smaller size in comparison to i.e. monoclonal antibodies such as Cetuximab, Erlotinib can act at the cytoplasmatic level, where it competes with ATP for binding to the catalytic domain of the tyrosine kinase, disrupting the downstream signal transduction of EGFR. Erlotinib has been currently used in patients for the treatment of non-small cell lung cancer (NSCLC) and lately it was the first EGFR-targeted therapy approved by the US Food and Drug Administration (FDA) for the treatment of pancreatic carcinoma, in combination with gemcitabine, although presenting only modest survival benefits [23].

1.6.2 The role of NHE1 in cancer

Among many factors involved in the maintenance of homeostatic growth of a cell, the tight regulation of cellular pH has been considered of high importance. While normal cells maintain their intracellular pH (pHi) within a physiological range, malignant cells show an acidic extracellular pH (pHe) and an alkaline intracellular pHi [57]. This pH gradient creates a perfect environment for metastatic progression, by stimulating acid-activated proteases which then facilitate tumor cell invasion and dissemination [58]. The development and maintenance of this pathological pH gradient is directly due to an overexpression and/or overstimulation of different membrane bound proton transporters implicated in the secretion of protons (H^+), including the Na^+/H^+ exchanger NHE1 [59-61],

H^+ pump ATPase [62, 63] and the monocarboxylate H^+ efflux cotransporters MCT1 and MCT4 [64-66].

Among them, the most extensively studied is the NHE1, one of the 9 isoforms of the sodium–hydrogen antiporter family, composed of 12 transmembrane segments at the N terminus, mediating a 1:1 exchange of extracellular sodium for intracellular protons across the cell membrane [67, 68], and a long C-terminal cytoplasmic tail, that regulates the interaction with different cytoskeletal proteins such as the actin binding protein ezrin [68]. NHE1 is found in virtually all mammalian tissues and cells where it is involved in the regulation of pHi homeostasis, cellular volume and cytoskeletal organization [57].

Regulation of NHE1 activity is mediated by multiple extracellular stimuli comprised of three major categories: i) ligand receptors of the ECM, such as integrin [69] and CD44 [70]; ii) physical stimuli such as osmotic cell shrinkage and shear stress (for reviews, see [71, 72]); and iii) soluble growth factors, hormones or cytokines acting through receptor tyrosine kinases and G-protein coupled receptors, which increase NHE1 activity through the classical Ras-mediated ERK cascade [68]. Recently it has been shown that NHE1 is an important effector of EGFR driven tumor progression [73]. In addition, there is ample evidence that NHE1 can be activated by the components of the tumor metabolic microenvironment such as low serum [74, 75], acidic pHe [76] and hypoxia [77-79] (Figure 7a).

Recent work has demonstrated that NHE1 is localized at the migratory leading edge of the tumor cell membrane, called invadopodia, (Figure 7b) and its activity has a double function in driving invadopodia formation and proteolytic activity through the alkalinization of the invadopodia cytosol which stimulates the dynamic process of invadopodia protrusion [80, 81] and the acidification of the extracellular peri-invadopodia nanospace which is necessary for the pHe dependent up-regulation of proteolytic enzymes, above all matrix metalloproteinases (MMPs) and cathepsins, implicated in the ECM digestion at the front of migrating tumor cells [82, 83]. It has also been observed that the deregulation of NHE1 activity is an important factor leading to metastasis in human breast cancer [74]. Due to its critical role in tumor progression, different inhibitors of NHE1 have been developed during the last years, of which the best studied is Cariporide.

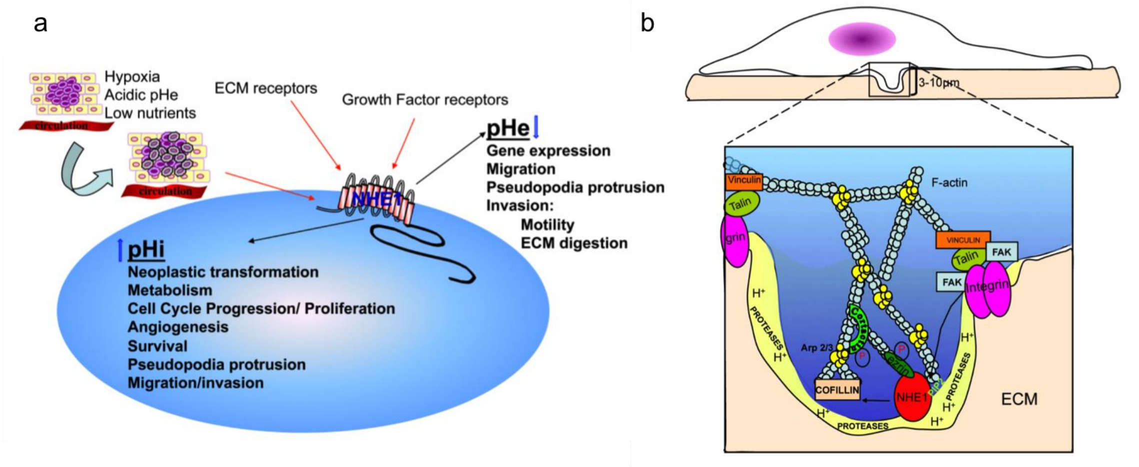
a
Hypoxia
Acidic pHe
Low nutrients
circulation
circulation
ECM receptors
Growth Factor receptors
NHE1
pHe
Gene expression
Migration
Pseudopodia protrusion
Invasion:
Motility
ECM digestion
pHi
Neoplastic transformation
Metabolism
Cell Cycle Progression/ Proliferation
Angiogenesis
Survival
Pseudopodia protrusion
Migration/invasion
b
3-10µm
Vinculin
Talin
grin
F-actin
VINCULIN
Talin
FAK
FAK
Integrin
H+
PROTEASES
Arp 2/3
Cortactin
P
P
ezrin
COFILLIN
NHE1
PIP2
PROTEASES
PROTEASES
H+
ECM

Figure 7: Activation of NHE1 and its role in invadopodia formation. (a) A general scheme showing the major systems regulating the activity of NHE1 with the resultant alkalinization of pHi and acidification of pHe. These altered intra- and extra-cellular environments drive a series of tumor cell behaviors resulting in progression to more aggressive tumor characteristics. (b) The insert is a magnification of the cellular extrusion into the ECM called invadopodia. They are F-actin enriched cellular protrusions responsible for ECM degradation whose formation is activated by integrin binding to the ECM and where enzymes such as MMP-2 and MMP-9 are released extracellularly in the peri-invadopodia region. In parallel, NHE1 is responsible for the localized production of protons and consequent acidification of this sub-cellular region, resulting in a favorable environment for the activation of those enzymes. Figure taken from Reshkin et al. [57]

1.6.2.1 Cariporide

Cariporide (N-(Aminoiminomethyl)-4-(1-methylethyl)-3-(methylsulfonyl)benzamide) is a potent selective inhibitor of NHE1, binding to Na+-binding site of the antiport [84], and used in the first instance in different clinical trials for ischemic-reperfusion injury, obtaining positive results as a cardioprotective drug, although with a slight cerebrovascular toxicity [84].

Most recently, the inhibition of NHE1 by Cariporide has also been explored in the oncological contest. It has been demonstrated that *in vitro* Cariporide reduces proliferation and induces apoptosis in cholangiocarcinoma cells [85], and inhibits hypoxia-mediated tumor invasion and migration of human tongue squamous carcinoma cells [86]. Following this approach, the role of the NHE1 in transducing the EGFR signal into increased growth and invasion behavior of tumor cells was demonstrated in different PDAC cells. Applying Cariporide in combination with the EGFR inhibitor Erlotinib demonstrated already a synergistic block of 3D multicellular tumor spheroid growth and of the invadopodia proteolitic activity [73]. However, how these very promising *in vitro* results on the synergistic inhibition of 3D growth and invasion by the Cariporide/Erlotinib combination can be translated to *in vivo* to reduce tumor growth and metastatic spread has still to be shown.

Aims of the Study

The main objective of my PhD project is to characterize and apply different orthotopic human PDAC mouse models to preclinically evaluate novel approaches for the visualization and therapy of PDAC.

The following tasks will be addressed:

1. The establishment of orthotopic human PDAC mouse models to provide a broad range of different PDAC xenografts (from well to poorly differentiated), resembling human pancreatic tumors and their metastatic spread as close as possible, for their use in preclinical imaging and therapeutic studies targeting tumor growth, invasion and metastatic spread. This will be achieved by:

    - Transplantation of five human PDAC cell lines with diverse differentiation status into the head of the pancreas of nude mice.
    - Evaluation of tumor growth rates and time of development of clinically relevant symptoms in the different PDAC mouse models.
    - Characterization of tumor morphology, differentiation grade and stroma organization.

2. The evaluation of Cetuximab-NIRF dye conjugates targeting EGFR (Cetux-Alexa-647 and Cetux-800CW) as new tools for fluorescence-guided surgery (FGS) to detect PDAC primary tumor and metastases. This will be achieved by:

    - Assessment of EGFR expression on PDAC cells and tumor tissues within the established orthotopic tumor models in order to identify the best suitable model.
    - Analysis of the *in vitro* binding of Cetux-Alexa-647 and Cetux-800CW conjugates to the selected EGFR expressing PDAC cells.
    - Preclinical *in vivo and ex vivo* evaluation of the tumor targeting specificity of Cetux-Alexa-647 in comparison to a control hIgG-Alexa-750 *conjug*ate.
    - Visualization of primary tumors and metastases using Cetux-800CW during fluorescence-guided dissection.
    - Validation of the binding of Cetuximab-NIRF dye conjugates to tumor tissue by NIRF microscopy and Odyssey scans.

3. The efficacy of a combined therapy targeting EGFR and NHE1 on growth, invasion and metastatic spread in the highly aggressive AsPC-1 mouse model. This will be achieved by:
    - Evaluation of the inhibitory effect of Erlotinib and Cariporide on the primary tumor growth, infiltration in the stomach and duodenum and metastatic spread in different peritoneal organs.

2 Material and Methods

2.1 Material

2.1.1 Equipment

Equipment:	**Manufacturer:**
Anesthesia system	VisualSonics, Toronto, Ontario, Canada
Analytical balance	Sartorius, Göttingen, Germany
AxioCamHR camera	Carl Zeiss, Göttingen, Germany
Centrifuge 5810 and 5424	Eppendorf, Hamburg, Germany
Chemi-Doc XRS luminescence detection system	Bio-Rad, München, Germany
Cooling centrifuge 5403	Eppendorf, Hamburg, Germany
Electrophoresis system Xcell SureLock™ Mini-Cell	LifeTechnologies (Invitrogen), Darmstadt, Germany
FGS system Quest Spectrum	Quest Medical Imaging, Middenmeer, the Netherlands
Fluorescence-Light microscope, Axiovert 200M	Carl Zeiss, Göttingen, Germany
Heating plate	Medax, Neumuenster, Germany
In vivo small animal microCT QuantumFX	Perkin Elmer, Waltham, MA, USA
Incubator, Heraeus BB6220	Heraeus Instruments, Hanau, Germany
Insulated box (cell freezing) Nalgene Mr. Frosty	Sigma Aldrich, Schnelldorf, Germany
Laboratory balance	Sartorius, Göttingen, Germany
Laboratory pipettes	Eppendorf, Hamburg, Germany
Light microscope, Telaval 31	Carl Zeiss, Göttingen Germany
Microtome HM 340E	Thermo Scientific, Darmstadt, Germany
Mini Trans-Blot ® Cells	Bio-Rad, München, Germany
Neubauer counting chamber	Schütt Labortechnik, Göttingen, Germany
Odyssey infrared imaging system	Li-Cor Biosciences, Bad Homburg, Germany
Optical imaging scanner IVIS Spectrum	Perkin Elmer, Waltham, MA, USA
Optical imaging scanner Optix MX2	ART, Montreal, Canada
ORCA-ER NIR-sensitive camera	Hamamatsu, Herrsching am Ammersee, Germany

pH meter Inolab	WTW, Weiheim, Germany
Steamer, MultiGourmet	Braun, Kronberg, Germany
Thermomixer Compact 5350	Eppendorf, Hamburg, Germany
Tissue processor, TP 1020	Leica, Wetzlar, Germany
Wallac Victor 2 multilabel counter 1420	Perkin Elmer, Waltham, MA, USA

2.1.2 Consumable supplies

Consumables:	**Manufacturer:**
Cell culture flasks	Sarstedt, Nümbrecht, Germany
Cellstar 12 wells culture plates	Greiner Bio-One, Frickenhausen, Germany
Cellstar 96 wells culture plates (F-bottom)	Greiner Bio-One, Frickenhausen, Germany
Cover glasses 12 mm Ø	Thermo Scientific, Darmstadt, Germany
Cryotube vials	Nunc, Roskilde, Denmark
Eppendorf tubes	Eppendorf, Hamburg, Germany
Falcontubes 15 ml, 50 ml	Corning, New York, USA
Filter pipette tips, 10 µl, 100 µl, 1000 µl	Sarstedt, Nümbrecht, Germany
Insulin syringes with integrated needle (30 G, 0.3 ml)	BD Bioscience, Heidelberg, Germany
Insulin syringes with integrated needle (30G x ½, 0.5 ml)	B. Braun, Melsungen, Germany
Microscope slides “Superfrost Plus”	Thermo Scientific, Darmstadt, Germany
ibidi µdishes $^{35\ \mathrm{mm/low}}$	Ibidi, Martinsried, Germany
Needles, Sterican, 27G x ¾	BD Bioscience, Heidelberg, Germany
Nitrocellulose hybridization transfer membranes	GE Healthcare (Amersham), Freiburg, Germany
NuPAGE Novex 3-8 % TRIS-acetate gels	Life Technologies, Darmstadt, Germany
Reusable Oral Gavage Needles	Fine Science Tool, Heidelberg, Germany
Serological pipettes 2 ml, 5 ml, 10 ml	Greiner Bio-One, Frickenhausen, Germany
Serological pipettes 25 ml	Corning, New York, USA
Surgical suture, absorbable, Vicryl 4/0	Johnson & Johnson, Neuss, Germany
Syringes 1 ml	BD Plastipak, Heidelberg, Germany
Tissue Tek cassette	Vogel, Giessen, Germany
Whatman filter paper	Bio-Rad, München, Germany

2.1.3 Chemicals and reagents

Chemicals and reagents:	**Manufacturer:**
Antibody diluent	Dako, Hamburg, Germany
Antigen-retrieval solution (pH 6)	Dako, Hamburg, Germany
Aqueous mounting medium (Aquatex)	Merck, Darmstadt, Germany
Bovine serum albumine (BSA)	Sigma Aldrich, Schnelldorf, Germany
ColorPlus™ Prestained Protein Ladder #7712	New England BioLabs, Frankfurt am Main, Germany
Western Blot Chemiluminescent HRP substrate	Millipore, Billerica, MA, USA
DAPI Nucleic Acid Stain	Invitrogen, Darmstadt, Germany
Diethylpyrocarbonate (DEPC) Water	Merck, Darmstadt, Germany
Dimethylsulfoxide (DMSO)	Sigma Aldrich, Schnelldorf, Germany
DPBS (1x) without Ca^{2+} and Mg^{2+}	Gibco/Invitrogen, Karlsruhe, Germany
Eosin G	Merck, Darmstadt, Germany
Ethanol absolute	Merck, Darmstadt, Germany
Fetal bovine serum (FBS) Gold	PAA Laboratories, Pasching, Austria
Formaldehyde 37%	Merck, Darmstadt, Germany
Glycine	Apllichem, Darmstadt, Germany
Haematoxylin (Mayer’s)	Merck, Darmstadt, Germany
Horse serum	Gibco/Invitrogen, Karlsruhe, Germany
Hydrochloric acid, 37%	Merck, Darmstadt, Germany
Hydrogen peroxid (H_2O_2) 30%	Merck, Darmstadt, Germany
Hydrophobic mounting medium (DePex)	Merck, Darmstadt, Germany
Imeron 300	Bracco, Konstanz, Germany
Low fluorescent food (Regime 210, U8959A01R)	Scientific Animal Food and Engineering, Augy, France
NuPAGE Antioxidant	Invitrogen, Darmstadt, Germany
NuPAGE Sample Reducing Agent (SRA) 10X	Invitrogen, Darmstadt, Germany
Paraffin (TM 60 °C)	Süsse, Guxhagen, Germany
Paraformaldehyd (pure)	Serva, Heidelberg, Germany
PBS tablets	Gibco/Invitrogen, Karlsruhe, Germany
ProLong gold antifade reagent with DAPI	Thermo Scientific, Darmstadt, Germany
Propanol	Chemsolute/Th. Geyer, Höxter, Germany
RIPA buffer	Thermo Scientific, Darmstadt, Germany

SEA BLOCK Blocking Buffer	Thermo Scientific, Darmstadt, Germany
Sodium chloride, isotone, 0.9%	Braun, Melsungen, Germany
Target retrieval solution	Dako, Hamburg, Germany
TRIS-HCl	Roth, Karlsruhe, Germany
TRIS-acetate SDS running buffer	Invitrogen, Darmstadt, Germany
Trypsin-EDTA (0.25%)	PAA Laboratories, Pasching, Austria
Tween-20	Sigma-Aldrich, Seelze, Germany
Western blot stripping buffer	Thermo Scientific, Bonn, Germany
Xylol	Merck, Darmstadt, Germany

2.1.4 Buffers and freezing medium

Buffer:	**Composition:**
TBS (10x)	1.4 M NaCl, 500 mM Tris-HCl, pH 7.5
TBST	1.4 M NaCl, 500 mM Tris-HCl, 0.05% Tween-20 pH 7.5
TRIS-glycine	50 mM TRIS-HCl (pH 7.6), 150 mM NaCl, 0.1 M glycine (pH 7.4)
Freezing medium	90% FCS + 10% DMSO

2.1.5 Kits

Kit:	**Manufacturer:**
AEC peroxidase substrate kit	BD Bioscience, Heidelberg, Germany
BCA protein assay kit	Thermo Scientific, Bonn, Germany
ECL kit	Merck Millipore, Darmstadt, Germany
Picro-Sirius Red Stain kit	Polysciences, Eppelheim, Germany

2.1.6 Anesthetics and Analgesic

Anesthetic:	**Manufacturer:**
Isoflurane	Abbvie, Ludwigshafen, Gemany
Ketamine 10%	Medistar, Ascheberg, Germany
Xylariem (Xylazine)	Ecuphar, Greifswald, Germany

Analgesic:	**Manufacturer:**
Novaminsulfon (Metamizole)	Zentiva, Berlin, Germany
Rimadyl (Carprofen)	Norbrook, Leverkusen, Germany

2.1.7 Fluorescent probes

Ligand:	**Fluorescence Dye:**	**Conjugate:**	**Dye to protein (DP) ratio:**
Cetuximab (Erbitux) Chimeric anti-human EGFR antibody Merck, Darmstadt, Germany	**Alexa Fluor 647** Invitrogen, Darmstadt, Germany	**Cetux-Alexa-647**	6.7
	IRDye 800CW Li-cor Biosciences, Bad Homburg vor der Höhe, Germany	**Cetux-800CW**	0.6
human IgG1 isotype #009-000-003 Jackson Immunolabs, Hamburg, Germany	**Alexa Fluor 750** Invitrogen, Darmstadt, Germany	**hIgG-Alexa-750**	5.3

Couplings and purifications (gel chromatography followed by a preparative gel filtration) of the conjugates was performed by Squarix Biotechnology GmbH, Marl, Germany

2.1.8 Therapeutic Drugs

Substance:	**Provider:**
Erlotinib HCl (OSI-744)	Genentech, South San Francisco, USA
Cariporide (HOE642)	Sanofi-Aventis, Paris, France
Captisol	Ligand Pharmaceuticals, San Diego, USA

2.1.9 Antibodies

Antibodies:	Application:	Provider:
mouse anti-actin mAb, #MAB1501 (cl. C4)	Western Blot	Merck Millipore, Darmstadt, Germany
goat anti-mouse mAb - HRP	Western Blot	GE Healthcare (Amersham), Freiburg, Germany
goat anti-rabbit mAb - HRP	Western Blot	GE Healthcare (Amersham), Freiburg, Germany
rabbit anti-human EGFR mAb, #MA5- 16359, cl. SP9	Immunohistochemistry	Thermo Scientific, Darmstadt, Germany
rabbit anti-human α-SMA IgG, #ab5694	Immunohistochemistry	Abcam, Cambridge, UK
Histofine Simple Stain Max PO-R (anti-rabbit-HRP)	Immunohistochemistry	Nichirei Biosciences, Tsukiji, Japan
goat anti-rabbit IgG, Alexa Fluor 488 labeled	Immunofluorecence	MoBiTec, Göttingen, Germany

2.1.10 Eukaryotic cell lines

Cells:	Tumor type:	Origin:
AsPC-1	human pancreatic cancer	nude mouse xenografts initiated with cells from the ascites of a 62-year-old woman with adenocarcinoma of the head of the pancreas and metastases to several abdominal organs
MIA PaCa-2	human pancreatic cancer	65-year-old man with adenocarcinoma involving the body and tail of the pancreas and infiltrating the periaortic area
PANC-1	human pancreatic cancer	56-year-old male with an adenocarcinoma in the head of the pancreas which invaded the duodenal wall
Capan-1	human pancreatic cancer	liver metastasis of a 40-year-old male with a pancreas adenocarcinoma in the head of the pancreas and metastases in regional lymph nodes
BxPC-3	human pancreatic cancer	61-year-old woman with adenocarcinoma of the pancreas body with no evidences of metastases
MCF7	human breast cancer	metastatic pleural effusion of an adenocarcinoma of the mammary gland
MDA MB 468	human breast cancer	pleural effusion of a 51-year-old black female patient with metastatic adenocarcinoma of the breast

All cells were bought from American type culture collection (ATCC)/LGC, Wesel

2.1.11 Cell culture media

Medium:	**Manufacter:**
DMEM + D-glucose (4.5 g/l), L-glutamine, Pyruvate	Gibco/Invitrogen, Karlsruhe, Germany
DMEM ⁄ F-12 (1:1) + Glutamax	Gibco/Invitrogen, Karlsruhe, Germany
IMDM + 25 mM HEPES	Gibco/Invitrogen, Karlsruhe, Germany
RPMI 1640	Gibco/Invitrogen, Karlsruhe, Germany

2.1.12 Software

Program:	**Used for:**
Artemis Capture Suite, v. 1.1.2	Quest Spectrum (Data acquisition)
AxioVision Rel., v. 4.6	Axiovert 200M fluorescence microscope
Image J [85]	Image processing
Image Studio, v. 3.1	Odyssey infrared imaging system
Living Image, v. 4.4	IVIS Spectrum (Data acquisition and analysis)
Optix, v 2.02.01	Optix MX2 (Data acquisition)
OptiView, v 2.01.00	Optix MX2 (Data analysis)
Past 3.11 [86]	Statistical analysis
Quantity One, v. 4.6.2	Chemi-doc luminescence detection system
Wallac 1420 Manager, Version 2.0	Victor 2 multilabel counter

2.1.13 Animals

Male athymic nude mice, strain CD1-Fox1$^{nu/nu}$ were directly purchased from Charles River (Sulzfeld, Germany) and used after 2 weeks of adaptation and strain NMRI-Fox1$^{nu/nu}$ were initially obtained from Charles River and bred in the Central Animal Facility, University Medical Center Göttingen.

2.2. Methods

2.2.1 Molecular Biology

2.2.1.1 Protein extraction and BCA protein assay

- **Protein extraction**

To obtain cell lysates, cells were detached from the dish as described in section 2.2.2.1, transferred to a 15 ml falcon tube, washed twice with Phosphate buffered saline (PBS), and resuspended in 100-300 µl of radioimmunoprecipitation assay (RIPA) buffer. After 30 min of incubation at room temperature (RT), cell debris were centrifuged for 15 min at 14000 rpm at 4°C and the supernatant was used as total cell extract.

- **BCA protein assay**

Protein concentration was determined using the bicinchoninic acid (BCA) protein assay kit that employs bovine serum-albumin (BSA) as a standard curve. The samples (duplicates) in a volume of 25 µl were incubated for 30 min at 37°C with the BCA reagent, composed of solution A (sodium carbonate, sodium bicarbonate, bicinchoninic acid and sodium tartrate in 0.1 M sodium hydroxide) and solution B (4% cupric sulfate). Absorbance at 550 nm was measured in the Wallac 1420 Victor 2 multilabel counter.

2.2.1.2 SDS-PAGE and Western Blot

30 µg of total protein extract reduced by 50 mM of NuPAGE sample reducing agent (NuPAGE SRA) were separated by SDS-PAGE (sodium dodecyl sulfate-polyacrylamide gel electrophoresis) on a NuPAGE Novex TRIS-acetate 3-8% gel according to the instruction manual. SDS-gels were then used for Western blot analysis.

Proteins were transferred to nitrocellulose hybridization transfer membranes using a series of increasing voltage gradients (10 V, 20 V, 30 V, 40 V for 10 min each, and 50 V for 1 h).

Blotted membranes were blocked for 1 h with 5% BSA in TRIS buffer containing 0.05% of Tween-20 (TBST), incubated with rabbit anti-EGFR antibody (1:1000) diluted in 5% BSA in TBST overnight at 4°C with gentle agitation. The day after, the membranes were washed with TBST buffer 3 times for 5 min and the membranes were then incubated with horseradish peroxidase (HRP)-coupled anti-rabbit antibody (1:8000) diluted in blocking solution for 1 h. After three washings with TBST, the bound antibody was visualized using chemiluminescent HRP substrate. Signals were detected in a Chemi-Doc XRS luminescence detection system. To verify equal amounts of proteins in each loaded sample, the membranes were stained afterwards with anti-actin antibody. For this purpose, the membranes were stripped by incubation in stripping buffer for 20 min at RT and washed and blocked as described above. The primary mouse anti-actin antibody and the HRP-coupled anti-mouse antibody were used at a 1:1000 dilution and 1:8000 dilution, respectively.

2.2.2 Cell biological methods

2.2.2.1 Cell culture conditions

Cells were cultivated under standard cell culture conditions at 37°C in a humidified atmosphere of 5% CO_2. The human PDAC cells AsPC-1 and BxPC-3 and the human mammary carcinoma cells MDA-MB-468 and MCF7 were grown in RPMI-1640 medium supplemented with 10% fetal calf serum (FCS). The human PDAC cells Capan-1 were grown in IMDM medium supplemented with 20% FCS, PANC-1 in high glucose (4.5 g/l) DMEM supplemented with 10% FCS and MIA PaCa-2 in DMEM/F-12 medium with Glutamax supplemented with 10% FCS and 2.5% horse serum.

For sub-cultivation, medium was removed, cells were washed twice with PBS, and treated with a 0.25% Trypsin-EDTA solution until they had detached from the dish. The enzyme was inhibited by addition of medium in which the cells were subsequently resuspended. When necessary, cells were counted in a Neubauer counting chamber and plated in the desired concentration into a new dish.

2.2.2.2 Cryoconservation

For cryoconservation, eukaryotic cells were detached as described above, centrifuged (1,200 x g for 2 min at RT), resuspended in freezing medium (1-5 x 10^6 cells/ml) and aliquoted into storage vials. Vials were placed in an freezing box in a -80 °C freezer overnight and finally stored in liquid nitrogen.

2.2.2.3 Revitalization

For revitalization, cryoconserved cells were quickly thawed in a 37°C water bath after being removed from liquid nitrogen. Then, cells were transferred to 10 ml pre-warmed medium and centrifuged (1,200 x g for 2 min at RT). After supernatant removal, cells were resuspended in ~3-5 ml of proper medium and transferred to a 25 cm^2 or 75 cm^2 cell culture flask. Subsequently, cells were allowed to attach overnight (37°C, 5% CO_2, 95% humidity) and medium was changed the next day.

2.2.2.4 *In vitro* binding assay to PDAC cells for Cetuximab NIRF conjugates

To analyze the binding of Cetux-Alexa-647 to AsPC-1 and MIA PaCa-2 cells, 2 x 10^5 tumor cells were seeded on coverslips in 24 wells plates. After 24 h the medium was removed, cells were washed once with PBS and incubated with 10 µg/ml of Cetux-Alexa-647 diluted in the culture medium for 1 h at 37°C. Afterwards, cells were washed three times with PBS to remove unbound probe and fixed with 4% paraformaldehyde (PFA) for 10 min washed with PBS and mounted in Prolong Gold Antifade Reagent with DAPI, in order to stain the nuclei. Cells were analyzed by NIRF microscopy using settings listed in Table 6 of section 2.2.5.1.

To analyze the binding of Cetux-800CW to AsPC-1 cells, 2 x 10^5 tumor cells were seeded in ibidi µdishes and incubated either with 10 µg/ml of Cetux-800CW diluted in culture medium or with medium only, for 1 h at 37°C. After 2 washes with PBS, cells were fixed with 4% PFA for 10 min, washed with PBS and mounted in Prolong Gold Antifade Reagent with DAPI. ibidi chambers were scanned with Odyssey infrared imaging system. Fluorescence intensity was detected by 800 nm channel in a raster mode with a resolution of 21 µm.

2.2.2.5 Cell preparation for implantation

One day before implantation, AsPC-1 and MIA PaCa-2 cells were sub-cultivated to achieve the cells in an exponential growth phase. On the day of implantation, cells were rinsed with PBS, detached as described above (section 2.2.2.1), and washed twice with corresponding culture medium. The cell number was determined using a Neubauer chamber and suspension volumes containing 1 x 10^6 cells were centrifuged at 1,200 x g for 2 min at RT. Right before the implantation, supernatant was removed and cell pellet was resuspended in 20 µl of PBS.

2.2.3 *In vivo* experiments

All animal experiments were approved by the administration of Lower Saxony (Germany). Animals were handled according to the guidelines issued by the animal protection (license no. 33.9-42502-04-13/1085). NIRF imaging was performed on 10 to 20 weeks old male athymic nude mice strain NMRI-Fox1$^{nu/nu}$ and Erlotinib/Cariporide treatment was performed on 9 weeks old male athymic nude mice strain CD1-Fox1$^{nu/nu}$

The mice were maintained in the animal facility of the University Medical Center of Göttingen in a sterile environment in individually ventilated cages and allowed food and water *ad libidum*. Cages, bedding, and water were autoclaved and the food was gamma irradiated. One week before starting the optical imaging experiments, mice received low fluorescence food to reduce the autofluorescence of gut and stomach.

2.2.3.1 Orthotopic PDAC mouse models

For orthotopic transplantation mice were anesthetized by intraperitoneal (i.p.) injection of 15 mg⁄kg xylazine and 75 mg/kg ketamine dissolved in PBS. The skin was disinfected, a median laparotomy was performed and the pancreas was exposed by applying gentle traction to the stomach. 1 x 10^6 cells in 20 µl of PBS were taken up with an insulin syringe with an integrated needle (30G) and cells were implanted into the head of the pancreas. The peritoneum was then closed first with continuous suture whereas the skin was closed with interrupted stitches, using 4/0 Vicryl in both cases. Mice were kept on a heating plate at 37°C and monitored until recovery from anesthesia. For analgesia, mice received Rimadyl (Carprofen; 5mg/kg) i.p. during surgery and Metamizole (1.33 mg/ml) in drinking water, for two days before and for three days after surgery. Recovered animals were inspected and weight three times a week for tumor formation, the occurrence of jaundice and general health conditions as well as weight loss.

Due to the deep location of the pancreas within the body of the animal, it is not possible to follow progressively tumor growth by external palpation in PDAC mouse models. Consequently, the criteria to sacrifice the mice were based on the loss of weight exceeding 20% of the initial weight lasting more than two days. Moreover, typical symptoms of PDAC such as jaundice and the general health condition of the mice were also carefully evaluated and taken into consideration. Animals were sacrificed with an overdose of CO_2 and cervical dislocation, and autopsies were performed. During autopsy, pancreatic tumors were excised together with stomach and duodenum, and tumor sizes were measured by a caliper. Under the assumption that the tumor shape is ellipsoid, the tumor volume was calculated according to the formula: volume [mm^3] = 0.5 x (length [mm] x width [mm] x height [mm]). Moreover, peritoneal organs, lymph nodes and lungs were excised, analyzed as for the presence of macroscopic metastases, and finally fixed in 4% formalin in PBS.

2.2.3.2 NIRF fluorescence imaging

AsPC-1 and MIA PaCa-2 tumor bearing nude mice were used for *in vivo* and *ex vivo* fluorescence imaging ~30 and ~90 days after tumor implantation, respectively.

Mice were anesthetized with 0.8-1 % vaporized isoflurane and each mouse received intravenously (i.v.) either a single dose of Cetux-Alexa-647 or the combination of Cetux-Alexa-647 and the control isotype hIgG-Alexa-750 (25 µg each in 150 µl of 0.9% NaCl) with an insulin syringe with integrated needle (30G x ½). *In vivo* and *ex vivo* imaging was performed by Optix MX2 and IVIS Spectrum scanners.

- **Optix MX2**

NIRF scans

Optix MX2 system was used for detection and quantification of Cetux-Alexa-647 and the control hIgG-Alexa-750 fluorescence signals *in vivo* over the upper abdomen of the living animals as well as *ex vivo* of the mice with open abdominal cavity and the explanted organs.

This system uses a fixed pulsed lasers as an illumination source, and works in reflection mode applying a raster acquisition scheme. It utilizes a single photon counting detector for measuring the number of photons coming in response to a pulsed excitation for each raster point. As illustrated in Figure 8, the resulted curve named temporal point spread function (TPSF) represents the distribution of the number of photons coming from a raster scan point over time.

For *in vivo* analysis, before (prescan), as well as at 24 h and 48 h after the injection of the fluorescent probes, mice were anesthetized with 0.8-1% vaporized isoflurane, placed inside the imaging device on a table preheated to 37°C, and scanned *in vivo* over the upper abdomen. After 48 h, mice were sacrificed and scanned with open abdominal cavity. Subsequently, tumors were excised and tumor sizes were measured with a caliper as described above (section 2.2.3.1). Furthermore, the organs such liver, kidneys, spleen, mesentery, as well as lung and lymph nodes, were isolated and imaged together with the primary tumors *ex vivo*. For *in vivo* and *ex vivo* acquisition of Cetux-Alexa-647 and hIgG-Alexa-750 derived fluorescence shown in the Table 2 were used:

Optix MX2

	Excitation wavelength	Emission filter
Alexa Fluor 647	635 nm	670 ± 20 nm
Alexa Fluor 750 / IRDye 800CW	730 nm	≥ 770 nm

	Laser Power	Integration time	Raster
in vivo scans	100 µW	1 sec	1 mm
ex vivo / in vitro scans	100 µW	0.5 sec	1.5 mm

Table 2 : Lasers, filters and acquisition settings of Optix MX2

Optix-MX2 was also used to scan mice that received Cetux-800CW for the fluorescence-guided dissection. Mice were scan *in vivo* before (prescan), as well as at 24 h after the injection of the fluorescent probe. After the 24 h *in vivo* scan, mice underwent fluorescence-guided dissection (section 2.2.3.4), and then excised organs were also scanned *ex vivo* by Optix-MX2. Settings used for *in vivo* and *ex vivo* NIRF imaging of Cetux-800CW are shown in Table 2.

Lifetime analysis

Optix MX2 was also used to measure the LTs of Cetux-Alexa-647 and of hIgG-Alexa-750 probes *in vitro* and *in vivo*. The device calculates the fluorescence LT by linear regression (blue line, Figure 8) in the slope of the TPSF obtained for a specific raster point of a scan.

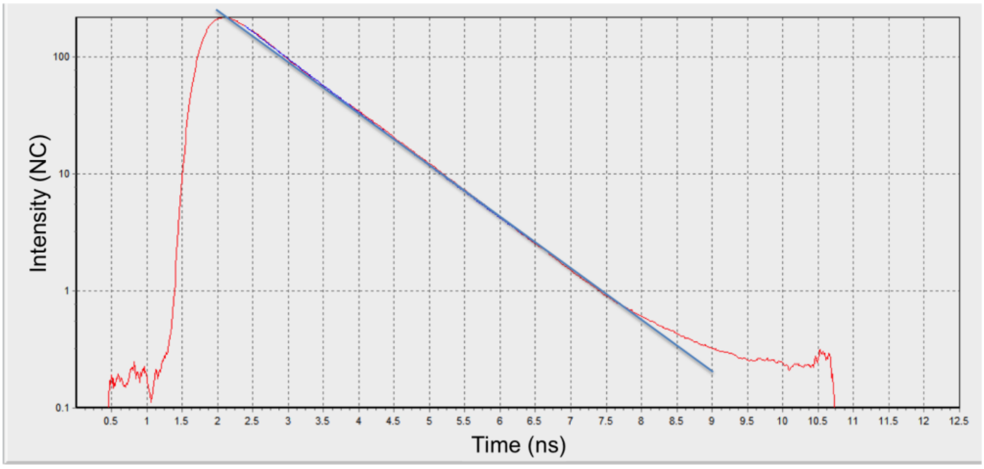

Figure 8 : TPSF of one representative raster scan point. TPSF curve, exemplarily shown for one scan point selected from a scan of a solution containing a fluorophore, representing the distribution of the number of photons over time. The time in nanoseconds (ns) between excitation pulse and detection of fluorescence photons is depicted on the x-axis, whereas the fluorescence intensity, in normalized counts (NC), is illustrated on the y-axis. From the decay of the curve (blue curve) the fluorescence LT is automatically calculated by Optix MX2.

LTs of the fluorescence conjugates Cetux-Alexa-647 as well as of the respective isotype control hIgG-Alexa-750 were first determined *in vitro*. For measurement, 0.05 µg of conjugates in 10 µl of the cell culture medium were dropped on a petri dish and scanned with Optix MX2 using settings indicated in Table 2. To measure the *in vivo* fluorescence LTs of the injected probes, Optix MX2 scans of the mice 24 h after the double-injection of Cetux-Alexa-647 and hIgG-Alexa-750 over the primary tumor or the liver, respectively, were considered.

- **IVIS Spectrum**

IVIS Spectrum uses a continuous wave quartz halogen lamp that simultaneously and uniformly illuminates the whole animal. Then, the light is spectrally filtered through 10 narrow band excitation filters and 18 narrow band emission filters.

For the *in vivo* analysis, isoflurane anesthetized mice were placed inside the IVIS imager and 2D fluorescence imaging of the whole body of the animal was performed in epi-fluorescence mode, before (prescan) as well as 24 h and 48 h after probe injection. *Ex vivo* scans of animals with opened abdominal cavity and of the excised organs were also performed. The detection of Alexa Fluor 647 and Alexa Fluor 750 fluorescence was obtained by IVIS Spectrum with the following settings reported in Table 3:

IVIS Spectrum

	Excitation filter	Emission filter
Alexa Fluor 647	622-656.5 nm	670-690 nm
Alexa Fluor 750	725.5-760 nm	790-810 nm

	Exposure time	f / Stop	Binning	Field of view (FOV)
in vivo / ex vivo scans	automatic	2	8	13.3

Table 3: Lasers, filters and acquisition settings of IVIS Sprectrum.

Moreover, since IVIS Spectrum enables the simultaneous visualization of multiple fluorophores differing in emission wavelength, by spectral-unmixing analysis. This was used to overlay Cetux-Alexa-647 and hIgG-Alexa-750 fluorescence imaging maps over the same mouse.

2.2.3.3 Co-registration of fluorescence tomography and CT data

AsPC-1 tumor bearing mice (n=2) received a single i.v. of Cetux-Alexa-647 and he control hIgG-Alexa-750 (25 µg each in 150 µl of 0.9% NaCl) 24 h prior to imaging and were sequentially scanned with QuantumFX micro CT (µCT) and IVIS Spectrum, and the data from both devices were co-registered. Since normal pancreas and pancreatic tumors in mice do not show uptake of intravenously injected iodine containing CT contrast agent, animals were fed for 24 h with pellets soaked with water-diluted oral iodine containing contrast agent (Imeron 300, diluted 1:10) to highlight the intestinal tract. Furthermore, mice received 200 µl of undiluted Imeron 300 orally by gavage shortly before the CT scan to display the stomach.

- **µCT**

First, the anatomical structures of the mice were as determined by µCT. Mice were anesthetized with 0.8-1.0% isoflurane, fixed ventral side up in the imaging shuttle and scanned with Quantum FX. This device is a low dose cone beam *in-vivo* µCT, especially designed for imaging of small animals such as mice. The following parameters were used for data acquisition: field of view 73 x 73 mm^2, tube voltage 70 kVp, tube current 200 µA and a total acquisition time of 17 s resulting in 3D data sets with a reconstructed voxel size of 150 x 150 x 150 µm^3.

- **3D Fluorescence Imaging Tomography (FLIT) imaging**

After the µCT scan, the imaging shuttle with anaesthetized mice was carefully moved inside the IVIS Spectrum device and imaged using the 3D FLuorescence Imaging Tomography (FLIT) mode, which enables first the reconstruction of the surface topography by using a structural illumination approach. Then, the 3D location of the fluorescent sources were as obtained by scanning the mouse ice in a transillumination setup using settings for the detection of either Alexa-Fluor-647 or and Alexa-Fluor-750 as indicated in Table 3.

In order to perform the fusion of the data obtained, the µCT images were exported as DICOM files and loaded together with the FLIT data into the Living Image software. The fiducial markers within in the imaging shuttle, allowed the reciprocal location of the data obtained with the two devices.

2.2.3.4 Fluorescence-guided dissection

Fluorescence-guided dissection of AsPC-1 tumor bearing mice was performed ~30 days after cell injection. Isoflurane anesthetized mice were i.v. injected with Cetux-800CW (25 µg in 150 µl of 0.9% NaCl) and sacrificed 24 h later. Section was guided with the Quest Spectrum clinical system for FGS equipped with a wide field lens for open surgery and a hand-held camera configured for the specific detection of IRDye 800CW fluorescence, using laser and filter settings shown in Table 4.

Quest Spectrum

	Excitation wavelength	Emission filter
IRDye 800CW	785 nm	> 808 nm

Table 4: Laser and filters settings of Quest Spectrum.

IRDye 800CW fluorescence and white light images were acquired simultaneously by the camera, allowing for an automatic depicted overlay of the two.

2.2.3.5 Schedule and evaluation of Cariporide-Erlotinib treatment

Mice implanted with AsPC-1 cells were treated with Cariporide or Erlotinib alone or a combination of them. At day 10 after implantation mice were randomly divided in four groups:

- Group 1: Erlotinib (50 mg/kg, 8.3 µl/gr BW, gauge) dissolved 6% Captisol in water applied orally by gavage
- Group 2: Cariporide (3 mg/kg, 3 µl/gr BW, i.p.) dissolved in 0.9% NaCl and given i.p.
- Group 3: a combination of Erlotinib (50 mg/kg, 8.3 µl/gr BW, gauge) and Cariporide (3 mg/kg, 3 µl/gr BW, i.p.) given as in groups 1 and 2.
- Group 4: control mice that received a solution of 6% Captisol orally by gavage and 0.9 % NaCl i.p. with volumes corresponding to the volumes applied for Cariporide and Erlotinib.

and each treatment was performed daily for 20 days.

At day 30 post implantation, animals were sacrificed as described above (section 2.2.3.1) and general status of the mice (presence of cachexia or jaundice) were documented. Then, the skin and peritoneum were opened and the primary tumor was carefully checked as for general morphology and macroscopically invasion in the stomach and duodenum. Afterwards, the tumor mass was measured as described in section 2.2.3.1.

In addition, peritoneal cavity, diaphragm, mesentery and organs such as liver, spleen, mesentery, diaphragm and kidney were analyzed for presence of macroscopic metastases. Metastases were identified, measured in size and counted.

For the microscopically evaluation of the invasion of the primary tumor into stomach and duodenum, primary tumors were cut at 4 different levels (distance: ~100 µm) and stained by IHC for EGFR as described in section 2.2.4.2. The four sections were analyzed by two researchers for infiltration of tumor cells in stomach and duodenum, which was then classified as follows: - (no infiltration), L (low infiltration), M (medium infiltration) and H (high infiltration). The highest grade obtained out of the four slides was considered.

To assess the tumor mass at treatment starting point, one additional group of mice was implanted with AsPC-1 cells and sacrificed at day 10 after transplantation. The small tumor mass developed was measured as described above (section 2.2.3.1).

2.2.3.6 Tissue preparation

Dissected tumors or organs were fixed in 4% formalin in PBS overnight and placed in Tissue Tek cassettes. The tissues were automatically dehydrated in an ethanol series and paraffinized in a tissue processor apparatus as indicated in Table 5.

repetition cycles	time	applied substance
1	1 h 30 min	60% Ethanol
2	1 h 30 min	75% Ethanol
2	1 h 30 min	95% Ethanol
2	1 h 30 min	100% Ethanol
2	1 h 30 min	Xylol
2	1 h 30 min	Paraffin

Table 5: Dehydration scheme for tissue processing.

Sections of the paraffin-fixed tumors and organs were obtained using made with the microtome in 2.5 µm thickness. Sections were dried overnight at RT, and stored at RT until staining was performed.

2.2.4 Histology of tissue sections

2.2.4.1 Hematoxylin-Eosin (HE) staining

Tissue sections were deparaffinized by heat at 60°C for 30 min, followed by two washes with xylol for 7 min each. Then, the sections were rehydrated using propanol (5 min) and decreasing concentrations of ethanol (95%, 75% and 60%) for 5 min each, followed by one wash with demineralized water. The Hematoxylin staining of cell nuclei was done for 5 min and after washing with demineralized water for 5 min, the cell cytoplasm of the cells was stained with Eosin G (1:10 dilution in H_2O) for 5 min. After staining, sections were washed shortly with demineralized water and dehydrated with increasing concentrations of ethanol (60%, 75% and 95%) and once in propanol, for 5 min each. Sections were then cleared twice in xylol (5 min each) and mounted in hydrophobic mounting medium (DePex).

2.2.4.2 Immunohistochemistry staining of tissue sections

For immunohistochemistry (IHC), tissue sections were deparaffinized and rehydrated as described in section 2.2.4.1. Antigen retrieval was performed by incubation in target retrieval solution (modified citrate buffer from Dako, pH 6) at 90°C in a steamer for 20 min. Sections were cooled down with cold DEPC water for 5 min and washed once with TBS for 5 min. The endogenous peroxidase was inhibited by incubation with 3% H_2O_2 for 10 min and washed twice with TBS (5 min).

After incubation with SEA BLOCK blocking buffer for 20 min at RT, sections were directly stained overnight at 4ºC with either the monoclonal rabbit anti-human EGFR antibody (SP9, 1:500) or the polyclonal rabbit anti-mouse alpha-smooth muscle actin (α SMA) antibody (1:500) diluted in antibody diluent. Sections were washed and further stained with one drop of undiluted anti-rabbit-HRP antibody (Histofine Simple Stain Max PO) for 60 min at RT. After two washes with TBS (5 min each), sections were incubated with 3-Amino-9-ethylcarbazole (AEC) peroxidase substrate for 30 min at RT, washed once with distilled water and counterstained with Hematoxylin for 20 sec. Following counterstaining, the sections were rinsed briefly in demineralized water and then in running tap water for 5 min. Finally, sections were mounted with aqueous mounting medium (Aquatex) and dried overnight at RT.

2.2.4.3 Collagen staining

For collagen I & III staining, Picro-Sirius Red staining kit was used. Tumor sections were deparaffinized and rehydrated as described in section 2.2.4.1. Then, Hematoxylin was used to stain the nuclei of the cells for 5 min, and after one wash with demineralized water for 5 min, sections were further immersed in solution A (phosphomolybdic acid) for 2 min, washed briefly with demineralized water and placed first into solution B (Picro-Sirius Red F3BA stain) for 60 min and then directly into solution C (0.01 N Hydrochloride Acid) for 2 min. Sections were then dehydrated, cleared in xylol and mounted as described in section 2.2.4.1.

HE and colorimetric staining of tumor tissue were evaluated with Axiovert 200M microscope using an AxioCamHR camera.

2.2.5 NIRF analysis of tumor and metastases sections

2.2.5.1 Immunofluorescence and NIRF microscopy

Immunofluorescence was performed on tumor tissue derived from animals co-injected with Cetux-Alexa-647 and hIgG-Alexa-750 and employed for NIRF imaging.

Sections were deparaffinized, rehydrated and antigen retrieval was performed as described in section 2.2.4.1. Autofluorescence was blocked with TRIS-glycine buffer for 10 min at RT, sections were washed twice with TBS (5 min each) and incubated with SEA BLOCK blocking buffer for 20 min. Then, sections were directly incubated overnight with rabbit-anti human EGFR antibody (SP9, 1:500) diluted in antibody diluent, washed twice with TBS (5 min each) and incubated at RT for 1 h with the secondary anti-rabbit-Alexa-Fluor 488 antibody (1:400). Afterwards, sections were washed twice with TBS (5 min each) and counterstained with DAPI (4 µg/ml) for 10 min, washed once with TBS (5 min) and mounted with aqueous mounting medium (Aquatex) and dried overnight at 4ºC.

For examination of Cetux-Alexa-647 and hIgG-Alexa-750 fluorescence signal on human AsPC-1 and MIA PaCa-2 tumor cells and PDAC tumor tissues, the fluorescence microscope Axiovert 200M equipped with a NIR-sensitive ORCA-ER digital camera was used. Filter settings are illustrated in Table 6. Images obtained were analyzed using Image J [85].

Fluorescence microscopy

	Excitation filter	Emission filter
Alexa Fluor 647	640 ± 15 nm	690 ± 25 nm
Alexa Fluor 750	708 ± 37.5 nm	809 ± 40.5 nm
Alexa Fluor 488	450-490 nm	515-565 nm
DAPI	365 ± 12.5 nm	445 ± 25 nm

Table 6: Microscopy filter settings used for detection of fluorophores.

2.2.5.2 Odyssey scans of tissue sections

For analysis of primary tumor and metastatic organs from AsPC-1 mice undergoing fluorescence-guided dissection, sections were deparaffinized and rehydrated as described in section 2.2.4.1. Sections were then washed once with TBS (5 min) before, directly mounted with aqueous mounting medium (Aquatex) and dried overnight at 4ºC. Cetux-800CW derived fluorescence signal on tumor tissue and metastases in different organs, was evaluated in the Odyssey infrared imaging system. Fluorescence intensity was detected by a 800 nm channel in a raster mode with a resolution of 42 µm.

2.2.6 Statistical analysis

The significance was analyzed by two-tailed unpaired Student's t-test using Past [86] program. Statistical significance was defined as $p \leq 0.05$.

3. Results

3.1 Orthotopic human PDAC mouse models

In order to select the most suitable models for preclinical evaluation of novel NIRF imaging and therapeutic strategies, different PDAC mouse models obtained by orthotopic implantation of well characterized human pancreatic tumor cell lines [87] were analyzed in detail for tumor growth, time of development and grade of invasion into the surrounding organs. Moreover, morphological features such as differentiation grade and desmoplastic reaction were investigated.

3.1.1 Growth characteristics and time of tumor development

Five different PDAC mouse models were established by orthotopic implantation of 1 x 10^6 human pancreatic tumor cells into the head of the pancreas of athymic male nude mice. Because human pancreatic cancer includes a multitude of histomorphological subgroups, AsPC-1, MIA PaCa-2 and PANC-1 cell lines as undifferentiated- or poorly differentiated-, BxPC-3 as moderately differentiated- and Capan-1 as differentiated cell lines were chosen to be applied.

Orthotopic transplantation into the head of the pancreas of all five human PDAC cell lines resulted in local tumor growth and in most cases in tumor invasion into the duodenum and stomach. However, in each PDAC mouse model, depending on the cell line implanted, a distinct pattern of tumor growth and progression occurred. Therefore, mice were sacrificed at different time points after cell transplantation, defined as time of tumor development and equating to the time between the day of implantation and the endpoint of the experiment (Figure 9). As PDAC tumors are hardly detectable by visual inspection, the time for sacrifice was chosen based on the presence of typical symptoms of PDAC such as weight loss of more than 20% of the initial weight, apathetic behavior or jaundice.

Due to a fast tumor growth rate of AsPC-1 *in vivo* (poorly differentiated), transplanted mice (n=6) were sacrificed as early as 4 to 5 weeks after cell transplantation, whereas mice that received the other two poorly differentiated cell lines, MIA PaCa-2 (n=9) and PANC-1 (n=4), were sacrificed later, between 10 and 16 weeks and between 12 and 20 weeks, respectively. 12 to 13 weeks was the time required for the BxPC-3 xenografts (moderately differentiated, n=7) to develop, whereas the well differentiated Capan-1 model (n=10) showed symptoms related to tumor development between 13 to 19 weeks after cell transplantation. Representative images of the macroscopical appearance of the different tumors after dissection are shown in Figure 9. AsPC-1 and BXPC-3 transplanted mice formed the smallest tumor lesions compared to the other PDAC mouse models with average tumor volumes of 122 ± 93 mm^3 and 193 ± 111 mm^3, respectively, followed by the PANC-1 mouse model, which is characterized by an average tumor volume of 294 ± 194 mm^3. Instead, MIA PaCa-2 and Capan-1 cells developed much larger tumor masses in the range of 845 ± 428 mm^3 and 1183 ± 812 mm^3, respectively. Furthermore, in all PDAC models tumors usually invaded into the duodenum and stomach (Figure 9), resulting in complications such as stomach and/or duodenum obstruction, accompanied by rapid weight loss. The tumor take rate, defined as the percentage of tumors that develop after orthotopic cell transplantation into mice, was 100% for AsPC-1, Capan-1 and BxPC-3 mouse models, whereas MIA PaCa-2 and PANC-1 cells revealed slightly lower tumor take rates of 90% and 75%, respectively.

	AsPC-1	MIA PaCa-2	PANC-1	BxPC-3	Capan-1
Time of Development (days)	30 ± 5	91 ± 23	115 ± 27	90 ± 8	116 ± 20
Tumor take rate *	100 %	90 %	75 %	100 %	100 %
Tumor Volume (mm^3)	122 ± 93	845 ± 428	294 ± 194	193 ± 111	1183 ± 812
Stomach/Duodenum invasion	+	+	+	+	+

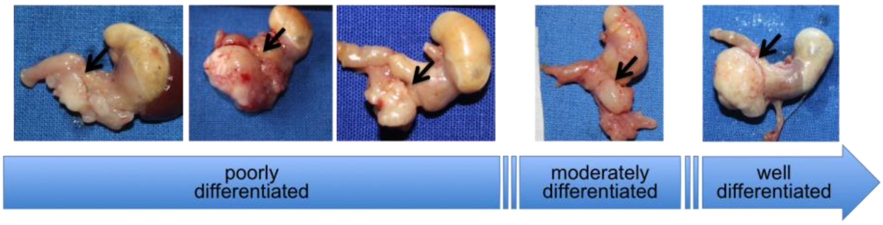

*percentage of tumors growing after orthotopic injection into mice

Figure 9: Characteristic features of primary tumor growth of human orthotopic PDAC mouse models. Time of tumor development, defined as the time between the day of implantation and the endpoint of the experiment, tumor take rate, defined as percentage of tumors that develop after orthotopic injection into mice, tumor volume and stomach/duodenum infiltration at the time of section are depicted for each PDAC xenograft. Representative images of the macroscopic morphology of the primary tumors invading into the stomach and duodenum (black arrow) are also depicted.

3.1.2 Histological features and desmoplastic reaction of primary tumors developed in PDAC mouse models

Primary tumors obtained from the five PDAC models were further analyzed histologically by HE and immunohistochemical staining of paraffin tumor sections (Figure 10).

Tumors from AsPC-1, MIA PaCa-2 and PANC-1 were diagnosed by HE staining (Figure 10, left column) as poorly differentiated PDAC, all with a completely homogenous and unorganized pattern of tumor cells. BxPC-3 tumors showed a moderately differentiated morphology with cells arranged in large round clusters (yellow arrow). Instead, tumor cells organized in duct-like clusters (yellow arrow) were found in the well differentiated Capan-1 tumors.

In order to assess in each mouse model the development of a desmoplastic reaction, a hallmark of human PDAC, paraffin sections of primary tumors were immunohistochemically stained with an antibody directed against α-SMA, a marker of activated pancreatic stellate cells, and histochemically stained with Sirius Red, for the detection of all types of collagen (I, II and III).

Each primary tumor obtained from the different PDAC mouse models revealed a distinct α-SMA staining pattern (Figure 10, middle column). All tumors showed reddish staining of elongated and myofibroblast-like stroma cells located among tumor cells, indicating the presence of activated PSCs. No differences in the amount of α-SMA positive cells were found between the tumors, however, in poorly differentiated primary tumors of the AsPC-1, MIA PaCa-2 and PANC-1 mouse models, α-SMA positive cells appeared homogenously dispersed between tumor cells. By contrast, in moderate to well differentiated BxPC-3 and Capan-1 tumors, α-SMA positive cells seemed to be more grouped around clusters of tumors cells.

Sirius Red staining (Figure 10, right column) revealed that only primary tumors of the Capan-1 model induced a large amount of collagen deposition around the duct-like tumor structures. Comparable collagen fibers surrounding the clusters of tumors were found in BxPC-3 mouse model, although containing less amounts of collagen. In contrast, the poorly differentiated tumors (MIA PaCa-2, AsPC-1 and PANC-1) were composed of a much more unorganized collagen deposition around the undifferentiated tumor cells. In each tumor model the same peri-tumoral areas were stained for both, α-SMA and Sirius Red.

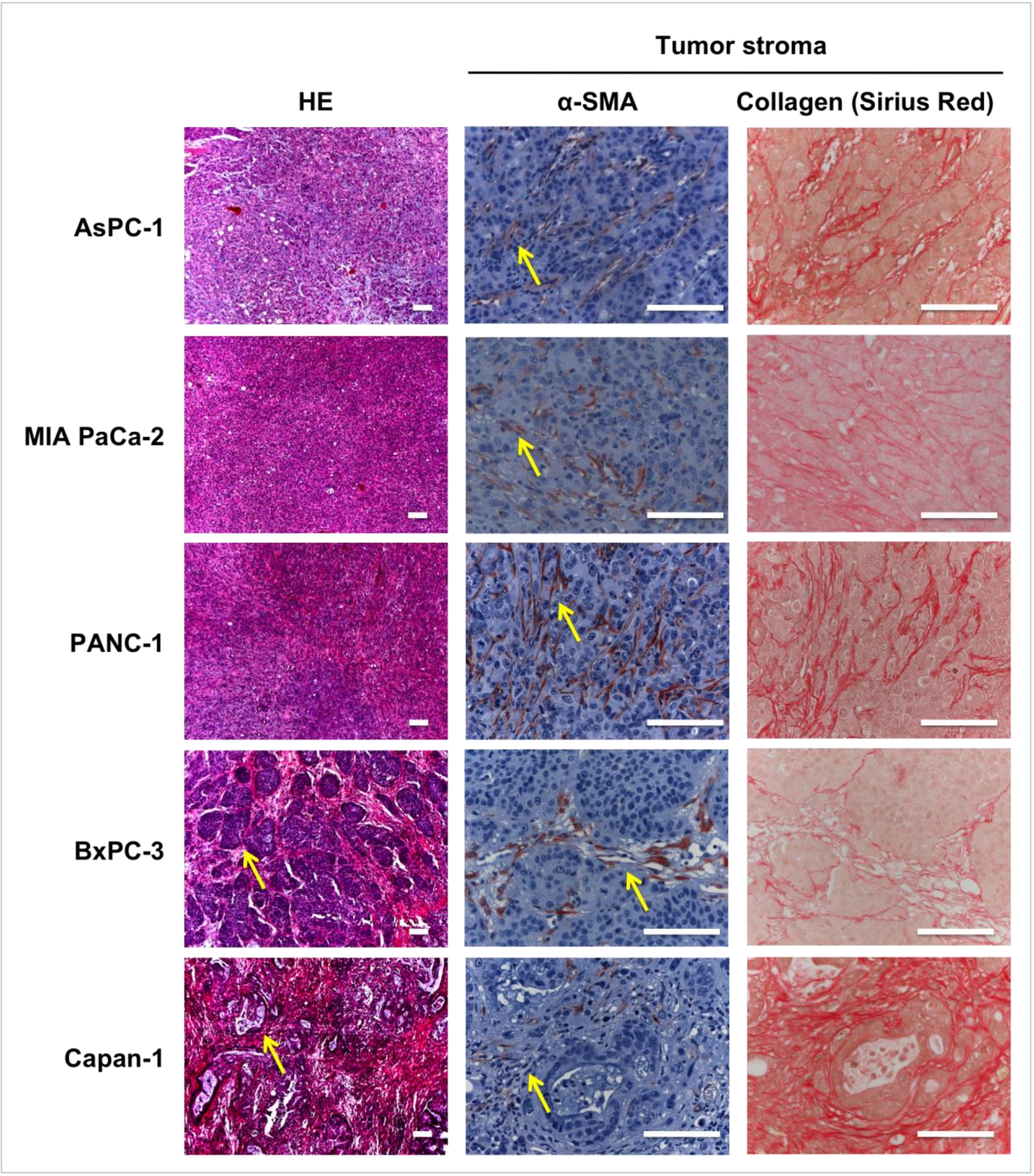

Figure 10: Paraffin sections of representative PDAC primary tumors, stained with HE (left), with an antibody directed against α-SMA (middle) and with Sirius Red kit for collagen (right). HE staining revealed differences in the grade of differentiation of the primary tumors. AsPC-1, MIA PaCa-2, PANC-1 show a poorly differentiated morphology, whereas BxPC-3 and Capan-1 reveal a moderately- and well-differentiated morphology, respectively. Yellow arrows indicate the presence of clusters of tumor cells in BxPC-3 and Capan-1 models. α-SMA staining showed activated PSCs (reddish staining; yellow arrows), dispersed all over the poorly differentiated tumors AsPC-1, MIA PaCa-2, PANC-1 and located around the clusters of the differentiated tumor BxPc-3 and Capan-1 cells. Sirius Red staining highlights elongated collagen fibers (strong red) in between the poorly differentiated cells and around the clusters of differentiated tumor cells. Note, that the same peri-tumoral areas are stained for α-SMA and Sirius Red in each mouse model. Scale bars represent 100 µm.

Taken together, five different PDAC models were established, each characterized by a distinct tumor growth rate and invasion behavior, independent of the grade of tumor differentiation. Moreover, each model revealed different characteristic morphological features such as grade of differentiation and development of desmoplastic reaction (the amount of collagen deposition and presence of PSC).

3.2 NIRF labeled Cetuximab targeting EGFR as a tool for fluorescence-guided surgery

Next, two of the orthotopic human PDAC mouse models were chosen to preclinically analyze the suitability of the already clinically used antibody Cetuximab, targeting human EGFR. The antibody was conjugated to fluorescence dyes in the NIR range to visualize primary PDAC tumors and detect small metastases in live mice by NIRF imaging and during fluorescence-guided dissection.

3.2.1 Characterization of PDAC cell lines for EGFR expression

In order to identify two human PDAC cell lines with high and low EGFR expression to be applied *in vivo* for NIRF imaging, the five human PDAC cell lines were analyzed for expression levels of EGFR protein by Western blotting. For this, 30 µg of total protein extract from each cell line was separated via SDS-PAGE and analyzed for the presence of bands at the expected molecular weight of 170 kDa, using a polyclonal anti-EGFR antibody (#2232). As positive and negative controls, we used MDA-MB-468 and MCF7 breast cancer cell lines, respectively.

As illustrated in Figure 11, a strong expression of EGFR was found in AsPC-1 and BxPC-3 cells, whereas a moderate and low expression of EGFR was observed in PANC-1 and MIA PaCa-2 cells, respectively. Capan-1 cells did not show any EGFR expression by Western blot analysis. β-actin expression was used as a loading control and showed equal amount of protein charge in each lane.

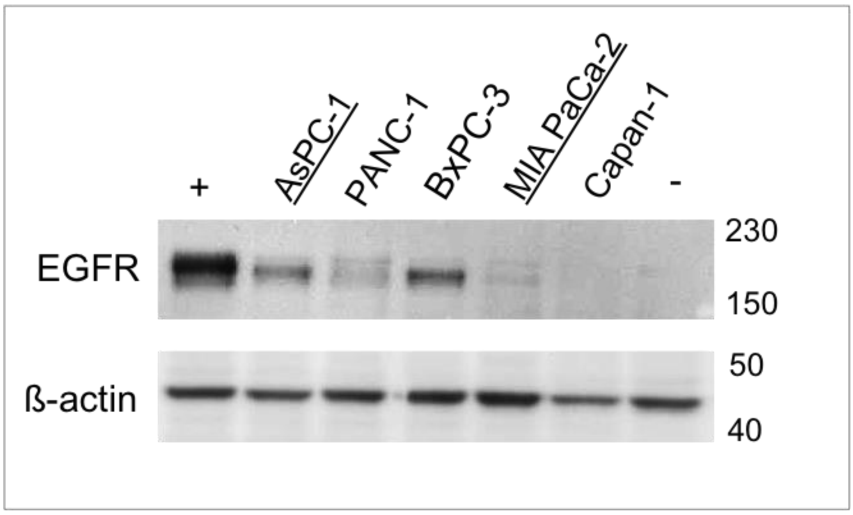

Figure 11: Expression of EGFR in PDAC cell lines. (a) Western-blot analysis shows high EGFR expression (170 kDa band) in AsPC-1 and BXPC-3 cells, moderate expression in PANC-1 cells, low expression in MIA PaCa-2 cells, and no expression in Capan-1 cells. MDA-MB-468 and MCF7 cells were used as positive (+) and negative (-) control, respectively. Staining of β-actin revealed a comparable amount of total protein loaded for all samples.

3.2.2 *In vitro* binding studies of NIRF labeled Cetuximab to EGFR expressing PDAC cells

NIRF labeled Cetuximab was used as follows: i) coupled to Alexa Fluor 647, one of the most common preclinically used NIRF dyes (Cetux-Alexa-647) at a dye-to-protein ration of 6.7, and ii) coupled to IRDye800CW (Cetux-CW800) at a dye-to-protein ratio of 0.6. For *in vivo* experiments, human IgG_1 coupled to Alexa Fluor 750 dye (hIgG-Alexa-750) at a dye-to-protein ratio of 5.3 was used as isotype control.

In order to characterize the binding of Cetux-Alexa-647 *in vitro* to high EGFR expressing (AsPC-1) and low EGFR expressing (MIA PaCa-2) cells, the cells were grown on coverslips and incubated for 1 h at 37ºC with 10 µg/ml of Cetux-Alexa-647. Figure 12a, left) shows that incubation of AsPC-1 cells with Cetux-Alexa-647 resulted in a strong plasma membrane and cytoplasmatic cell staining pattern indicating partial internalization of the conjugate. In comparison, MIA PaCa-2 cells incubated with Cetux-Alexa-647 showed a comparable plasma membrane and cytoplasmatic staining pattern, but with much lower intensity (Figure 12a, right).

Furthermore, binding of Cetux-800CW (10 µg/ml) to AsPC-1 was tested *in vitro* in cells grown on ibidi µdishes. After 1 h of incubation with the conjugate at 37ºC, cells were fixed and scanned by the Odyssey imager, which allows the detection of NIR fluorescence signals with a resolution lower than a fluorescence microscope. Scans revealed high fluorescence signals over the AsPC-1 cells incubated with Cetux-800CW (Figure 12b, left) in comparison to control cells incubated without the conjugate (Figure 12b, right), which showed only low autofluorescence.

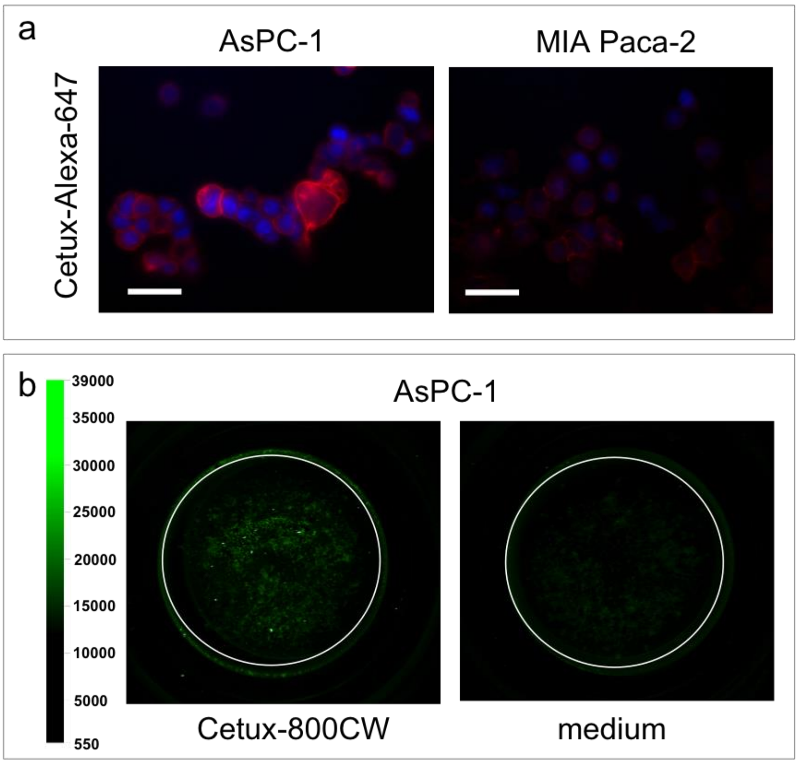

Figure 12: *In vitro* binding of Cetux-Alexa-647 and Cetux-800CW to PDAC cells. (a) Representative pictures of fixed AsPC-1 and MIA PaCa-2 cells incubated with Cetux-Alexa-647. Higher fluorescence signals on the membrane and within the cytoplasm of AsPC-1 cells were found than at the cell membrane and within the cytoplasm of MIA PaCa-2 cells (red). The nuclei are counterstained with DAPI (blue). Scale bars represent 50 µm. (b) Odyssey scan of fixed AsPC-1 cells incubated with Cetux-800CW (left) shows higher fluorescence signals in comparison to the low autofluorescence obtained over the AsPC-1 cells incubated with medium only (right).

Taken together, these results show that the NIRF labeled Cetuximab conjugates, Cetux-Alexa-647 and Cetux-800CW, bind to the high EGFR-expressing AsPC-1 and to the low EGFR-expressing MIA PaCa-2 cells *in vitro*. This confirms that AsPC-1 and MIA PaCa-2 PDAC mouse models are suitable for the evaluation of labeled Cetuximab as a tool for *in vivo* NIRF imaging.

3.2.3 Characterization of EGFR expressing orthotopic PDAC xenografts

AsPC-1 and MIA PaCa-2 orthotopic PDAC models were chosen as the most suitable mouse models to validate the binding of Cetux-Alexa-647 and Cetux-800CW to PDAC cells *in vivo* and to assess their suitability for NIRF imaging *in vivo* and during fluorescence-guided surgery.

Growth pattern and metastatic behavior of AsPC-1 and MIA PaCa-2 xenografts were evaluated by autopsy and then, EGFR expression on primary tumors was assessed by immunohistochemistry.

3.2.3.1 Tumor growth, invasion and metastatic spread of ASPC-1 and MIA PaCa-2 mouse models

Mice transplanted with AsPC-1 cells, were sacrificed within 4 to 5 weeks after implantation, a time point when mice developed symptoms related to PDAC growth. At this time, primary tumors showed average tumor volumes of 122 ± 93 mm^3, with invasion into the stomach and duodenum (Figure 9). Moreover, the AsPC-1 model showed a massive tumor spread to different sites and organs adjacent to the pancreas such as the left liver lobe, spleen, peritoneum and mesentery (Figure 13a-c). AsPC-1 tumor nodules were also found at the site of surgical incision (Figure 13d) where occasionally a large tumor mass developed.

Unlike AsPC-1, orthotopically transplanted MIA PaCa-2 mice were sacrificed much later, within 10 to 16 weeks after transplantation. At this time, tumor volumes in the range of 845 ± 428 mm^3 were much larger than the ones observed in the AsPC-1 mouse model (Figure 9). Similar to AsPC-1, invasion of the MIA PaCa-2 primary tumor into the stomach and duodenum was macroscopically observed (Figure 9). However, in contrast to the highly aggressive model AsPC-1, MIA PaCa-2 primary tumors did not form metastases in the peritoneal organs, but commonly infiltrated, in almost 90% of the mice, the liver hilus (Figure 13e), occasionally causing jaundice (Figure 13f).

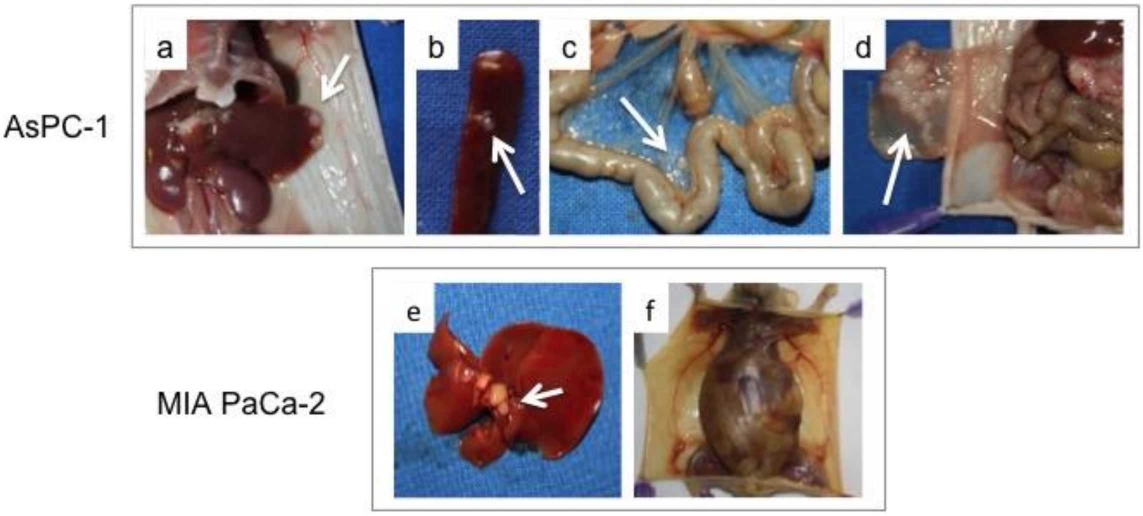

Figure 13: Macroscopic appearance of the metastatic spread of orthotopic AsPC-1 and MIA PaCa-2 xenografts in nude mice. (a-d) Representative macroscopic images of peritoneal organs from AsPC-1 tumor bearing mice during section performed ~30 days after cell transplantation (n=6). White arrows point to metastases in the (a) left liver lobe, (b) spleen (c) mesentery as well as to (d) tumor mass grown at the surgical scar. (e, f) Representative autopsy findings in MIA PaCa-2 xenografts during section performed ~90 days after orthotopic transplantation (n= 9). (e) Representative macroscopic image of metastases and infiltration of tumor cells into the liver portal triad, leading to biliary obstruction (arrow). (f) Evident jaundice of the mouse as a consequence of the biliary obstruction.

3.2.3.2 Characterization of EGFR expression in tumor tissue obtained from PDAC mouse models

Both, AsPC-1 and MIA PaCa-2 primary tissue sections obtained from tumors that developed in each PDAC mouse model were stained for the expression of the human EGFR by immunohistochemistry. Figure 14a,b shows relatively homogenous strong EGFR staining on AsPC-1 tumor cells. In contrast, a heterogeneous EGFR expression pattern was found within MIA PaCa-2 tumors (Figure 14c). Here, weak EGFR staining was observed in different areas within the primary tumor mass (Figure 14d), whereas tumor cells especially in the proximity of the invasion front into the stomach and duodenum showed strong staining of EGFR (Figure 14e). Large and central necrotic areas, with almost no EGFR staining, were present in both, AsPC-1 and MIA PaCa-2 primary tumors (black arrows; Figure 14a,c).

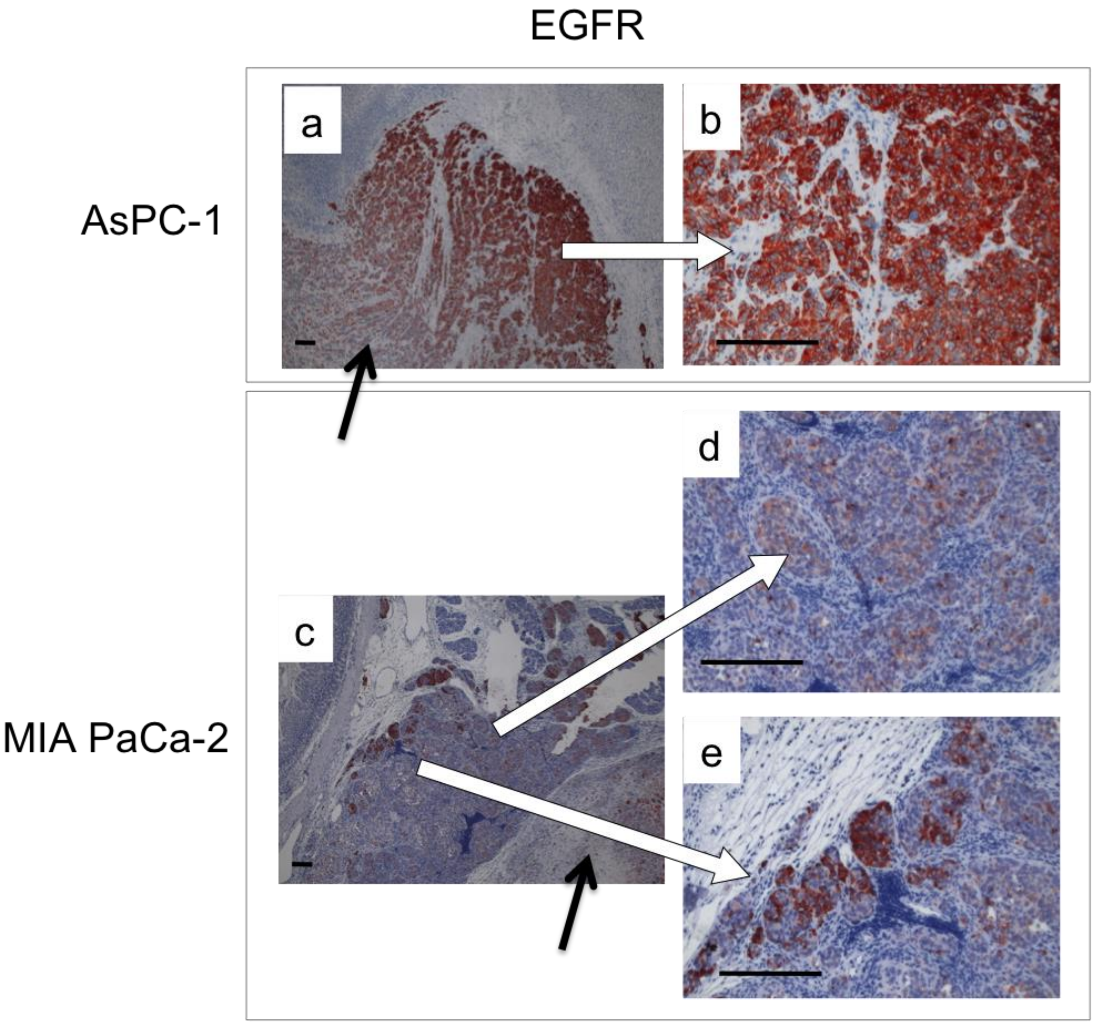

Figure 14: EGFR expression on AsPC-1 and MIA PaCa-2 primary tumors. (a-b) Anti-EGFR staining of paraffin sections of a primary AsPC-1pancreatic tumor shows relatively homogeneous and strong EGFR expression in almost all tumor cells. (c-e) Anti-EGFR staining of the MIA Paca-2 pancreatic tumor shows a heterogeneous expression pattern of EGFR in tumor cells. (c) Tumor areas with weak EGFR staining (d) as well as areas with high EGFR staining (e) are depicted. Necrotic areas in the center of both tumors are indicated in (a) and (c) by black arrows. Scale bars represent 200 µm.

Taken together, these results show that AsPC-1 and MIA PaCa-2 mouse models differ not only in their tumor growth rates but also show a distinct pattern of metastatic spread in peritoneal organs: the AsPC-1 mouse model was highly metastatic whereas the MIA PaCa-2 model revealed rare metastatic spread and common infiltration of the liver hilus. Therefore, both PDAC models, expressing high and moderate amounts of EGFR protein in the tumor, are suitable for the evaluation of the *in vivo* NIRF imaging approach in combination with NIRF labeled Cetuximab to visualize not only the primary tumor but also small metastatic lesions.

3.2.4 Characterization of the *in vivo* binding of Cetux-Alexa-647 in EGFR expressing PDAC xenografts

In order to assess the ability of Cetux-Alexa-647 to visualize EGFR expressing PDAC tumors, the fluorescent probe was applied to tumor bearing mice and analyzed by *in vivo* and *ex vivo* optical imaging.

3.2.4.1 Cetux-Alexa-647 accumulates within primary PDAC tumors *in vivo*

Binding of Cetux-Alexa-647 to AsPC-1 and MIA PaCa-2 xenografts was first analyzed *in vivo*. NIRF imaging experiments were performed at distinct time points after transplantation, depending on the different tumor growth rates of the two PDAC mouse models (described in section 3.1.1). Either 30 days (AsPC-1-tumor bearing mice) or 90 days (MIA PaCa-2-tumor bearing mice) after transplantation, mice were natively scanned with the Optix MX2 (upper abdominal scan) and the IVIS (whole body scan) in order to measure the level of autofluorescence background prior to probe injection. Then, Cetux-Alexa-647 was i.v. injected, either alone (25 µg; data not shown) or in combination with the control probe hIgG-Alexa-750 (25 µg of each; n=10 for AsPC-1 and n=7 for MIA PaCa-2) and imaging with both devices was performed 24 h and 48 h after probe injection to determine the distribution and binding kinetics of Cetux-Alexa-647 and the control.

Figure 15a shows a series of representative NIRF images of the upper abdomen (white rectangle represents the scanned area) of tumor bearing mice taken with the Optix MX2 before as well as 24 and 48 h after co-injection of Cetux-Alexa-647 and hIgG-Alexa-750. Cetux-Alexa-647 derived fluorescence detected in AsPC-1 mice (Figure 15a, upper panels) is diffusely localized over the scanned area of the upper abdomen, presumably due to the overlap of the signals derived from the primary tumor with the signals from the tumor mass grown at the surgical incision right above the primary tumor mass. In comparison, Cetux-Alexa-647 derived fluorescence in the MIA PaCa-2 tumor bearing mice (Figure 15a lower panels) had a lower intensity and was clearly localized over the center of the upper abdomen where the primary pancreatic tumors are expected to develop. In both tumor models the measured fluorescence intensities of Cetux-Alexa-647 were highest at 24 h and decreased at 48 h after injection.

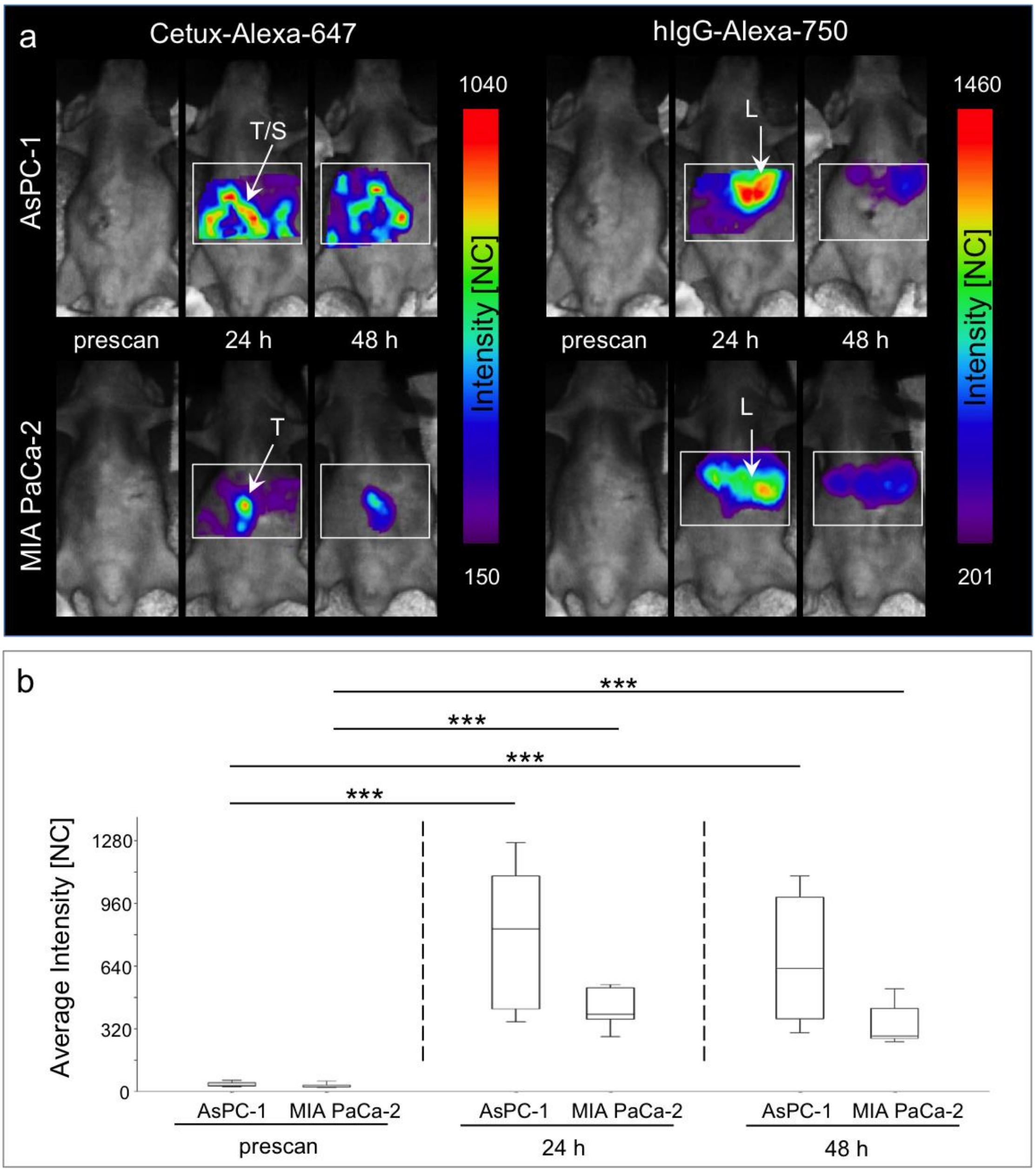
a
Cetux-Alexa-647
hIgG-Alexa-750
AsPC-1
MIA PaCa-2
T/S
T
L
L
prescan
24 h
48 h
prescan
24 h
48 h
1040
150
Intensity [NC]
1460
201
Intensity [NC]
b
***
***
***
***
Average Intensity [NC]
1280
960
640
320
0
AsPC-1
MIA PaCa-2
AsPC-1
MIA PaCa-2
AsPC-1
MIA PaCa-2
prescan
24 h
48 h

Figure 15: *In vivo* binding of Cetux-Alexa-647 to AsPC-1 and MIA PaCa-2 primary tumors. (a) Representative *in vivo* Optix MX2 scans of the upper abdominal area (white rectangle) before, 24 h and 48 h after co-injection of Cetux-Alexa-647 (left) and hIgG-Alexa-740 (right), 25 µg each, in AsPC-1 (upper panel, n=10) and MIA PaCa-2 (lower panel, n=7) tumor bearing mice. Cetux-Alexa-647, but not the control hIgG-Alexa-750, was detected over the AsPC-1 and MIA PaCa-2 primary pancreatic tumors (T), as well as over the tumor mass developed at the surgical scar (T/S) in the AsPC-1 model. Due to the overlap of the two tumor masses in the AsPC-1 model (primary tumor and tumor at the scar), average Cetux-Alexa-647 fluorescence intensity in the AsPC-1 mice is much higher and more diffuse than the signal obtained in MIA PaCa-2 mice. Fluorescence intensities are displayed in normalized counts [NC]. (b) Box plot showing significantly higher average fluorescence intensities [NC] measured over the tumor areas at 24 h and at 48 h (*** represent $p < 0.001$) than in prescans of both, AsPC-1 and MIA PaCa-2 tumor bearing mice.

In contrast, the co-injected control antibody, hIgG-Alexa-750, did not localize to the pancreatic tumor sites but showed fluorescence signals only over the liver area. Similar to the Cetux-Alexa-647, hIgG-Alexa-750 reached its maximum measured fluorescence intensity at 24 h after injection in both mouse tumor models. The native scans (prescan) of both mouse models did not show any significant fluorescence signals (Figure 15a).

As shown in Figure 15b, quantification of the average fluorescence intensities of Cetux-Alexa-647 over the tumor areas confirmed significantly higher fluorescence intensity in both, AsPC-1 and in MIA PaCa-2 mice at 24 h and 48 h compared to values of the prescans.

Although Optix MX2 allows high sensitivity scans in the intensity- and time-domains, this non-invasive imaging method is difficult to apply for high resolution multi-channel scans of larger areas or the whole body of a mouse, in particular due to the very long scanning times required. Therefore, in order to assess whole body distribution and reciprocal localization of both probes, Cetux-Alexa-647 and hIgG-Alexa-750, following each Optix MX2 scan mice were also scanned with the IVIS Spectrum using the spectral unmixing tool. Figure 16 shows an overlay of the two fluorescent signals derived from the Cetux-Alexa-647 and hIgG-Alexa-750 probes, detected *in vivo* in the AsPC-1 and MIA PaCa-2 tumor bearing mice 24 h after co-injection of both probes. As expected, Cetux-Alexa-647 derived fluorescence (red) was localized over the primary tumor in the MIA PaCa-2 model, whereas AsPC-1 mice showed Cetux-Alexa-647 derived fluorescence over both, the primary tumor and the surgical scar grown above it. No accumulation of Cetux-Alexa-647 in any other organs of both animals was observed. hIgG-Alexa-750 (green) accumulated in the liver in both tumor mouse models. In the overlays, yellow signals over the bladder were frequently visible, presumably representing the renal excretion of the unbound dyes, Alexa-647 (red) and Alexa-750 (green).

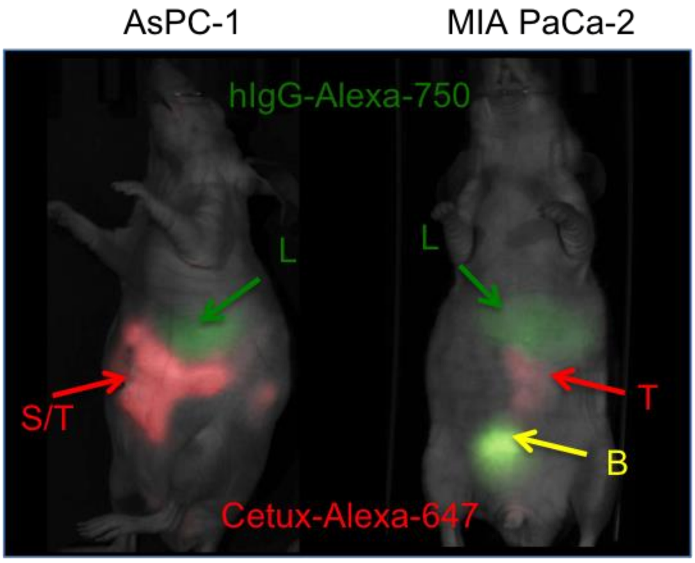

Figure 16: Overlays/Spectral unmixing of Cetux-Alexa-647 and hIgG-Alexa-750 signals obtained *in vivo* by IVIS Spectrum. Representative composite images obtained by spectral unmixing of IVIS scans 24 h after co-injection of Cetux-Alexa-647 (red) and hIgG-Alexa-750 (green) into AsPC-1 (left) and MIA PaCa-2 (right) tumor bearing mice. Cetux-Alexa-647 derived fluorescence signals were determined at the tumor site and at the tumor mass developed at the surgical incision (S/T) in the AsPC-1 model, or at the primary tumor site (T) in the MIA PaCa-2 model. By contrast, the control probe localizes only at the liver (L) in both tumor mouse models. Note, that a yellow signal over the bladder in the MIA PaCa-2 xenograft (B; right panel) is also visible, representing the co-localization of both signals.

In order to precisely localize the fluorescence images to the anatomical structure of the mice, we exemplarily performed a co-registration of 3D fluorescence data obtained by IVIS Spectrum with µCT scans performed with the Quantum FX using AsPC-1 tumor bearing mice (n=2) 24 h after the i.v. injection of Cetux-Alexa-647. The results of the co-registration are shown in Figure 17a, and demonstrate that Cetux-Alexa-647 derived fluorescence (orange) is visible in the upper abdominal cavity next to the stomach and duodenum that are highlighted by iodine containing contrast agent used for the CT scan. Additional fluorescence was detected over the bladder (B) and most probably derived, similar as stated above, from the free dye, here from Alexa-Fluor-647. In the center (Figure 17b), the *ex vivo* image of the same mouse confirmed the location of the AsPC-1 pancreatic tumor (T). The macroscopic image of the primary tumor in Figure 17c, confirms that the tumor is localized between the stomach (S) and the duodenum (D).

Co-registration of the control probe hIgG-Alexa-750 alone with the anatomical structure of the mice (data not shown) did not show any accumulation of the probe within the tumor.

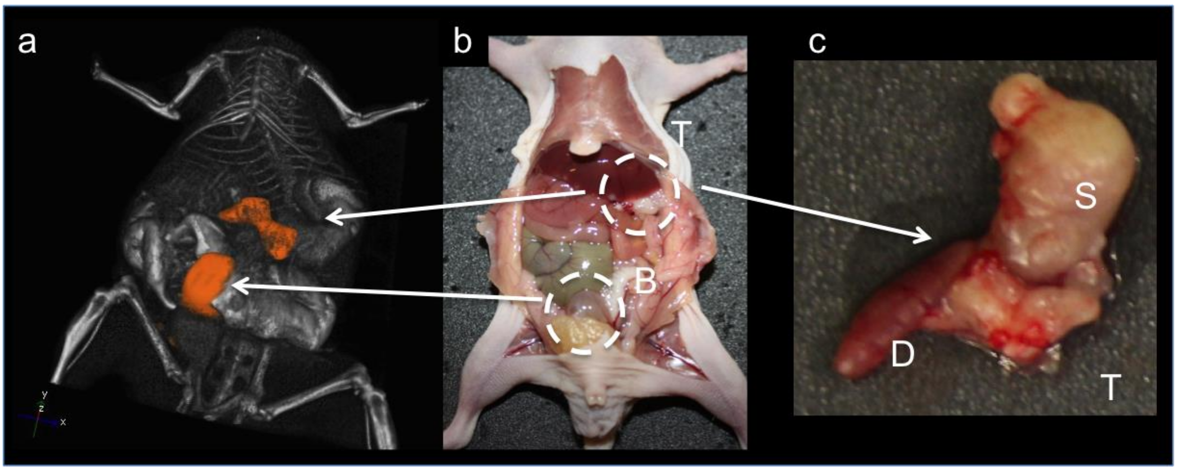

Figure 17: Correlation of Cetux-Alexa-647 to anatomical structures *in vivo* by co-registration of 3D fluorescence signals with µCT data. (a) Fusion of the 3D NIRF data sets with 3D µCT demonstrates correlation of the Cetux-Alexa-647 derived fluorescence to the site of the pancreatic tumor. The other intense fluorescence signal visible in the scan is derived from the bladder (B). (b) Corresponding photograph of the same animal *ex vivo* confirms that the pancreatic tumor (T, white dashed circle) developed on the left side of the mouse and dorsal to the liver. (c) Macroscopic appearance of the primary pancreatic tumor (T) confirms that it extended between the stomach (S) and the duodenum (D).

Taken together, we could clearly show that Cetux-Alexa-647, but not the control hIgG-Alexa-750 antibody, specifically accumulates in both, AsPC-1 and MIA PaCa-2, primary tumors *in vivo,* with a more pronounced accumulation in high EGFR expressing AsPC-1. Moreover, the AsPC-1 primary tumor was perfectly visualized by Cetux-Alexa-647 derived signal within the anatomical structure of the mouse.

3.2.4.2 Validation of the specificity of *in vivo* signals by fluorescence LTs

In order to confirm that the fluorescence signals detected *in vivo* over the tumor and the liver of the PDAC mice were specific for Cetux-Alexa-647 and hIgG-Alexa-750, respectively, we measured fluorescence LTs of the two conjugates *in vitro* (Figure 18a) and compared them with the fluorescence LTs of the signals measured *in vivo* 24 h after injection (Figure 18b).

The TPSFs (Figure 18a, middle) of representative points on the *in vitro* scans of Cetux-Alexa-647 (left) and hIgG-Alexa-750 (right) revealed LTs of 1.34 ns and 0.59 ns, respectively. Comparable fluorescence LTs were obtained for the *in vivo* scans (Figure 18b; middle). Cetux-Alexa-647 scans (Figure 18b; left) showed LTs of 1.37 ± 0.05 ns at the tumor site in the AsPC-1 and 1.47 ± 0.02 ns in the MIA PaCa-2 mouse model, whereas hIgG-Alexa-750 scans (Figure 18b; right) revealed LTs of 0.73 ± 0.02 ns over the liver in the AsPC-1 and 0.71 ± 0.03 ns in MIA PaCa-2 mouse model, confirming that the signals obtained *in vivo* are specifically derived from the injected probes.

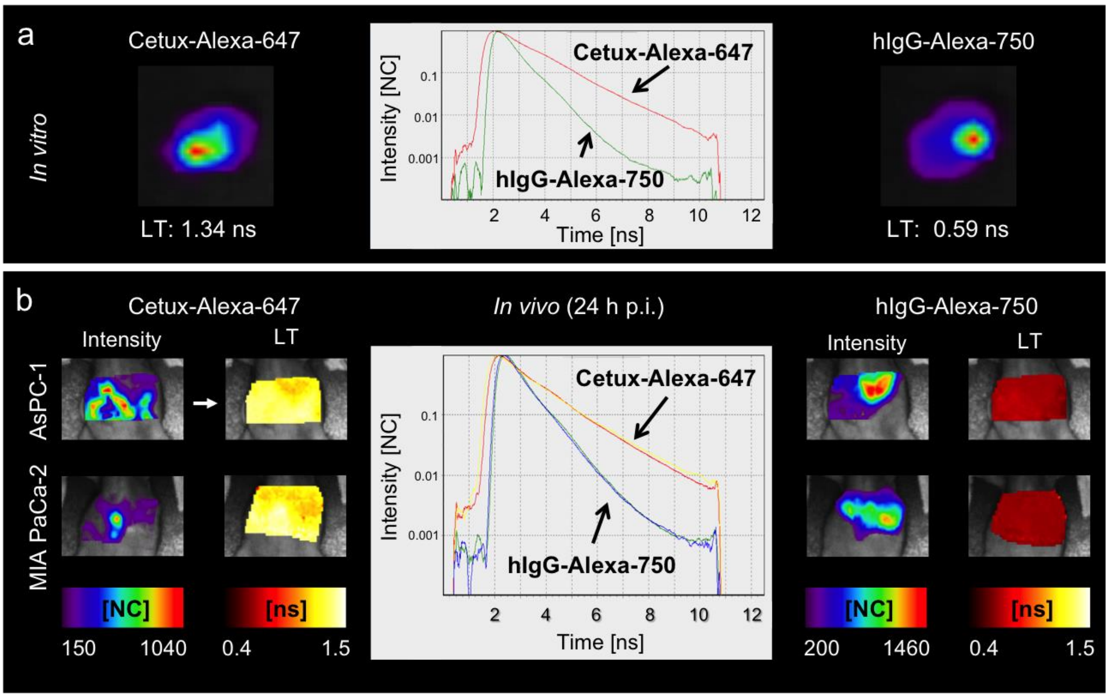
a
In vitro
Cetux-Alexa-647
LT: 1.34 ns
Intensity [NC]
0.1
0.01
0.001
Cetux-Alexa-647
hIgG-Alexa-750
2
4
6
8
10
12
Time [ns]
hIgG-Alexa-750
LT: 0.59 ns
b
Cetux-Alexa-647
Intensity
LT
AsPC-1
MIA PaCa-2
[NC]
150
1040
[ns]
0.4
1.5
In vivo (24 h p.i.)
Intensity [NC]
0.1
0.01
0.001
Cetux-Alexa-647
hIgG-Alexa-750
2
4
6
8
10
12
Time [ns]
hIgG-Alexa-750
Intensity
LT
[NC]
200
1460
[ns]
0.4
1.5

Figure 18: *In vitro* and *in vivo* fluorescence LTs of Cetux-Alexa-647 and hIgG-Alexa-750. (a) Representative *in vitro* scans of both probes, Cetux-Alexa-647 (left) and hIgG-Alexa-750 (right) taken with Optix MX2. Middle panel shows the corresponding representative TPSFs. The monoexponential decay of each curve was used to calculate the fluorescence LT of both, the EGFR targeting probe Cetux-Alexa-647 (1.34 ns) and the control probe hIgG-Alexa-750 (0.59 ns). (b) The same representative *in vivo* intensity scans of AsPC-1 (left) and MIA PaCa-2 (right) mouse models 24 h after probe injection that are also shown in Fig. 15a, with corresponding LT maps as well as representative TPSFs (middle panel), demonstrating that *in vivo* fluorescence LTs over the tumors (for Cetux-Alexa-647) and the liver (for hIgG-Alexa-750) are comparable to the *in vitro* LTs of each probe. TPSFs are graphed as fluorescence intensity [NC] versus time [ns].

3.2.5 Cetux-Alexa-647 detects PDAC primary tumors and metastases by *ex vivo* optical imaging

In order to confirm the exact location of the *in vivo* Alexa-647 and Alexa-750 signals, mice were sacrificed and consecutively scanned *ex vivo* with opened abdominal cavity using Optix MX2 (Figure 19) and IVIS Spectrum (data not shown) 48 h after probe injection, a time point when the *in vivo* fluorescence signal had clearly decreased.

As shown in the left panel of Figure 19, Cetux-Alexa-647-derived signals were clearly localized over the MIA PaCa-2 and AsPC-1 primary tumors (white arrow, T) as well as at the tumor nodules on the scar of the AsPC-1 model (white arrow, S), depicted also in the *ex vivo* image of the mouse (middle panel; primary tumor = white dashed tracing; scar = red dashed tracing). Consistently, no hIgG-Alexa-750 derived fluorescence signals (Figure 19, right panel) were visible over the MIA PaCa-2 or the AsPC-1 tumor area, but the hIgG-Alexa-750 derived signals clearly were localized at the liver. NIRF scans of Cetux-Alexa-647 and hIgG-Alexa-750 frequently revealed high fluorescence signals detected within the bladder (white arrow, B) in both mouse models.

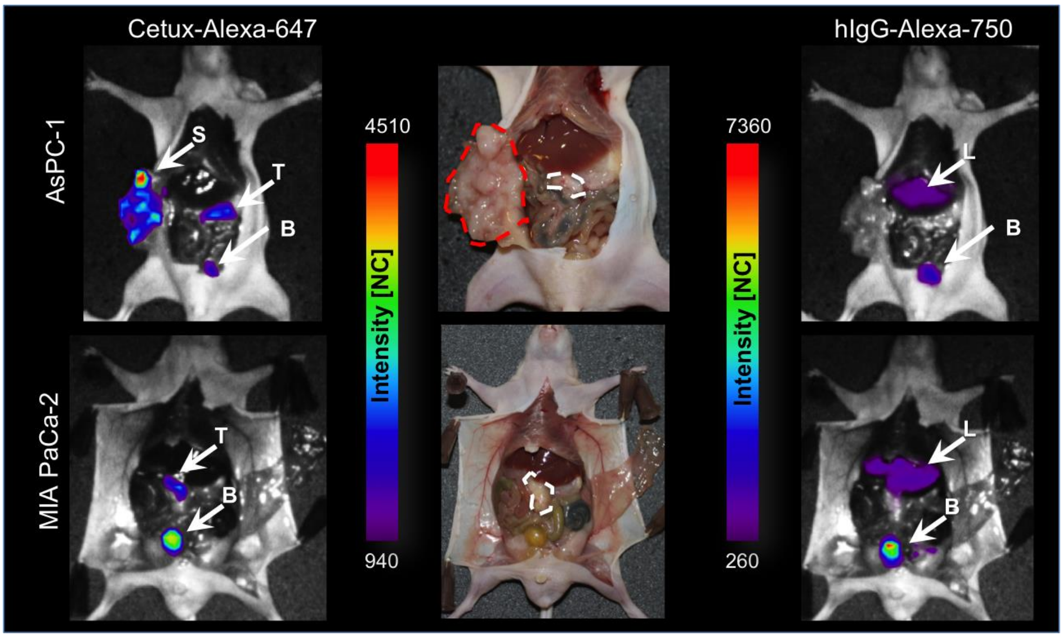

Figure 19: *Ex vivo* detection of Cetux-Alexa-647 over AsPC-1 and MIA PaCa-2 primary tumors. *Ex vivo* NIRF scans of Cetux-Alexa-647 (left) and hIgG-Alexa-750 (right), of the same AsPC-1 (upper panel) and MIA PaCa-2 tumor bearing mice (lower panel) shown in Figure 15 (*in vivo* scans), after opening the abdominal cavity. The corresponding photographs of the mice (middle panel) confirm the presence of AsPC-1 and MIA PaCa-2 primary tumors (white dashed tracing) and the localization of the tumor mass developed at the surgical scar of AsPC-1 mice (red dashed tracing). Cetux-Alexa-647 signals co-localize with the AsPC-1 and MIA PaCa-2 tumor areas (T = primary tumor, S = tumor mass at the surgical incision, white arrows), whereas hIgG-Alexa-750 signals co-localize with the liver (L). B (white arrow) indicates the fluorescence signal coming from the bladder of AsPC-1 and MIA PaCa-2 mice detected on both Cetux-Alexa-647 and hIgG-Alexa-750 NIRF scans.

Primary tumor, spleen, lung, liver, kidney, mesentery, lymph nodes and diaphragm from both PDAC mouse models that received the double injection of Cetux-Alexa-647 and hIgG-Alexa-750 were explanted and scanned *ex vivo* with Optix MX2 (Figure 20) and IVIS Spectrum (data not shown). As shown on the left of Figure 20a, upper panel, in addition to the primary tumors developed in both tumor models, also the metastatic sites of the AsPC-1 model at the diaphragm, left liver lobe and mesentery as well as the tumor mass at the site of surgical incision (arrows), displayed a strong Cetux-Alexa-647 derived fluorescence. Since no metastases in the peritoneal organs and over the scar were macroscopically found in the MIA PaCa-2 tumor bearing mouse, no fluorescence signals were observed over the different organs (Figure 20a, lower panel). These findings are consistent with the characteristic low metastatic behavior of the MIA PaCa-2 mouse tumor model in comparison to the high number of metastases found in the AsPC-1 model, as also described in section 3.2.3.1. On the contrary, representative NIRF scans for the control probe hIgG-Alexa-750 shown on the right of Figure 20a revealed, together with the corresponding photograph in the middle panel, only a strong accumulation of hIgG-Alexa-750 within the liver of both mouse models, whereas only background fluorescence signals were detected over AsPC-1 and MIA PaCa-2 primary tumors (white circles).

Furthermore, the average *ex vivo* fluorescence intensities of Cetux-Alexa-647 and hIgG-Alexa-750 over tumor areas (white circles) were quantified (Figure 20b). *Ex vivo* scans confirmed that AsPC1 tumors displayed a significantly (p=0.04) higher Cetux-Alexa-647 average fluorescence intensity than the MIA PaCa-2 tumors. On the contrary, only very low hIgG-Alexa-750 average fluorescence intensities could be measured over tumor areas, with no significant differences when comparing the low hIgG-Alexa-750 signals over AsPC-1 and MIA PaCa-2 tumors.

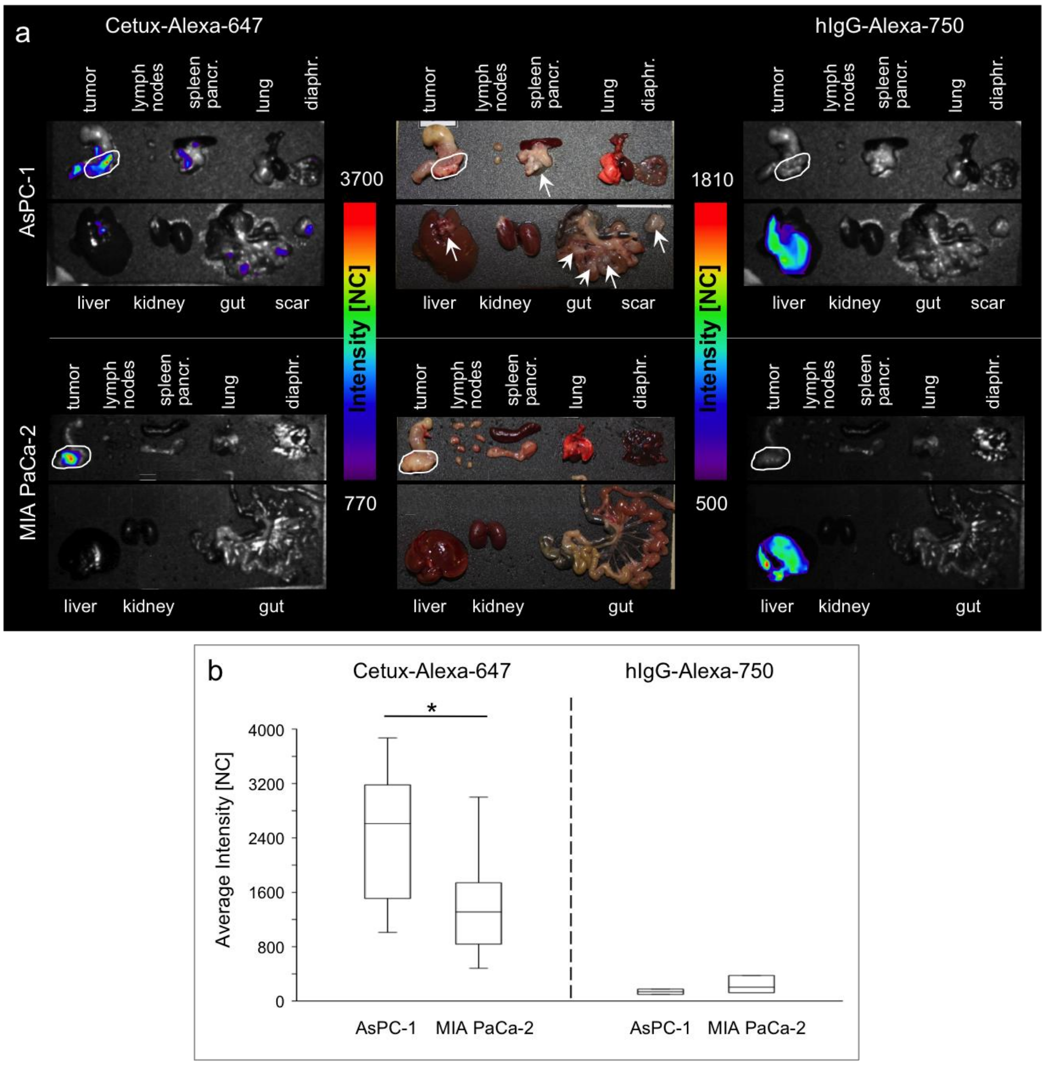
a
Cetux-Alexa-647
hIgG-Alexa-750
AsPC-1
MIA PaCa-2
tumor
lymph nodes
spleen pancr.
lung
diaphr.
liver
kidney
gut
scar
3700
770
1810
500
Intensity [NC]
b
Cetux-Alexa-647
hIgG-Alexa-750
*
Average Intensity [NC]
4000
3200
2400
1600
800
0
AsPC-1
MIA PaCa-2
AsPC-1
MIA PaCa-2

Figure 20: Biodistribution of Cetux-Alexa-647 analyzed by *ex vivo* NIRF imaging. (a) Representative *ex vivo* NIRF scans of Cetux-Alexa-647 (left) and hIgG-Alexa-750 (right) of the excised AsPC-1 (upper panel) and MIA PaCa-2 (lower panel) tumors and organs as well as the corresponding photograph (middle). Cetux-Alexa-647 derived fluorescence was detected over both, AsPC-1 and MIA PaCa-2 primary tumors (white circles) as well as in the AsPC-1 model over metastases in the mesentery, pancreas and in the left liver lobe (arrows). The control hIgG-Alexa-750 was not visible over the tumor areas of both tumor models but accumulated clearly in the liver (right). (b) Box plots of average *ex vivo* fluorescence intensities [NC] of Cetux-Alexa-647 and hIgG-Alexa-750 quantified over the explanted tumors of both tumor models (* p=0.04) are shown.

3.2.6 Validation of Cetux-Alexa-647 fluorescence by NIRF microscopy

Binding of the i.v. injected Cetux-Alexa-647 to tumor cells within AsPC-1 and MIA PaCa-2 primary tumor was confirmed by NIRF microscopy of tissue sections obtained from mice that received Cetux-Alexa-647 and hIgG-Alexa-750 simultaneously. Tissues were stained *ex vivo* by immunohistochemistry with anti-EGFR antibody targeting a different epitope of the receptor than Cetuximab. Figure 21 shows the binding of *in vivo* administered Cetux-Alexa-647 (red) to tumor cells expressing EGFR (*ex vivo* staining, green). Cetux-Alexa-647 (red) clearly bound only to EGFR-positive cells, stained in green. Nevertheless, some cells showed solely green staining, suggesting that *in vivo* injected Cetux-Alexa-647 conjugate did not bind to every tumor cell that expresses EGFR. As expected, hIgG-Alexa-750 derived fluorescence was not detected within the primary tumor sections by NIRF microscopy (data not shown).

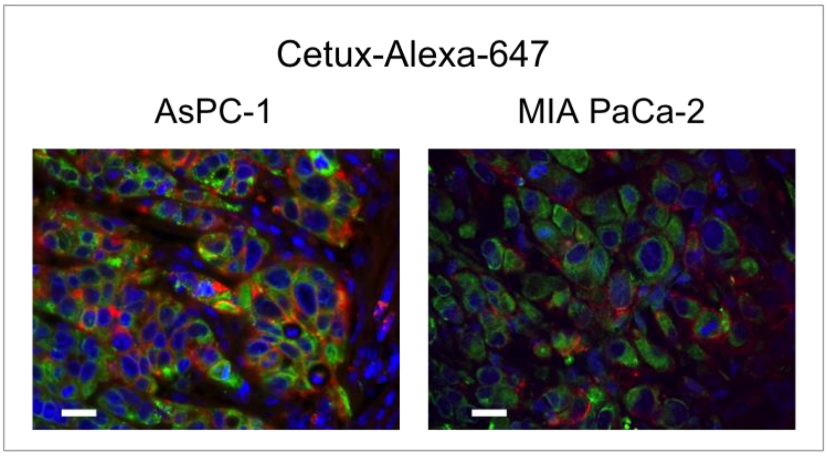

Figure 21: Binding of *in vivo* injected Cetux-Alexa-647 to tumor cells analyzed by *ex vivo* NIRF microscopy. NIRF microscopy of paraffin sections of AsPC-1 (left) and MIA PaCa-2 (right) primary tumors excised 48 h after i.v. injection of both, Cetux-Alexa-647 and hIgG-Alexa-750 and co-stained by IHC with an anti-EGFR antibody confirmed binding of the *in vivo* applied Cetux-Alexa-647 (red) to the membrane of EGFR-positive tumor cells (green), although not to all EGFR expressing tumor cells. Nuclei are counterstained with DAPI (in blue). Scale bars represent 50 µm.

Taken together, *in vivo* and *ex vivo* analysis of Cetux-Alexa-647 distribution by NIRF imaging, demonstrate the suitability of the NIRF Cetuximab conjugate to visualize not only primary PDAC tumors but also various metastases in multiple peritoneal organs, especially in the highly aggressive AsPC-1 model. NIRF microscopy confirmed specific binding of Cetux-Alexa-647 to EGFR expressing tumor cells, however not to all EGFR positive cells. Therefore, application of Cetux-Alexa-647 for fluorescence-guided dissection of PDAC was considered to be performed in the AsPC-1 mouse model.

3.2.7 Cetux-800CW detects AsPC-1 tumors and metastases during fluorescence-guided dissection

In order to evaluate Cetuximab as a tool for fluorescence-guided surgery, Cetuximab was conjugated to the IRDye 800CW (Cetux-800CW) to adapt the fluorophore to the settings of the Quest Spectrum clinical device for FGS. Cetux-800CW (25 ug) was employed i.v. during fluorescence-guided dissection of AsPC-1 tumor bearing mice (n=5), 30 days after tumor cell transplantation. 24 h after the injection of the probe, tumor bearing mice were sacrificed to proceed with the dissection accompanied by real time monitoring with the Quest Spectrum clinical system for FGS.

Figure 22a shows selected frames of the representative real-time movie made during the progressive steps of the dissection, showing overlays of the two views of the camera. The first two frames show the mouse with intact skin (Frame 1) and peritoneum with scans of three highly fluorescent areas over the upper abdomen (Frame 2), immediately taken after sacrifice and exposure to the camera. The larger fluorescent area represents the tumor mass that developed at the surgical scar (S), whereas the two small fluorescent lesions (M1 and M2) may correlate to metastatic sites. Frame 3 shows clear delineation of the primary tumor mass (T) that show high fluorescence signals, partially covered by the liver. Furthermore, the tumor mass developed at the site of surgical incision (S), after opening the peritoneum of the mouse is clearly visible. In addition, tumor lesions, such as M1 (at the peritoneum, close to the larger tumor mass developed at the surgical incision) and M2 (at the costal arch) shown in the previous frame could be clearly localized and a small metastasis at the left liver lobe (M3) was further detected at this stage. Frame 4 shows the entire primary tumor (T) that was then exposed to the camera enabling its image-guided resection. Furthermore, multiple tumor nodules (M4), hardly discernable with the naked eye, were detected along the stomach. The *ex vivo* image of the same mouse (Figure 22b) shows the macroscopic appearance of the tumor (T, black arrow), the tumor mass at the surgical incision (S, black arrow) and the very small metastases at the costal arch (M2, black arrow), which are barely visible without FGS.

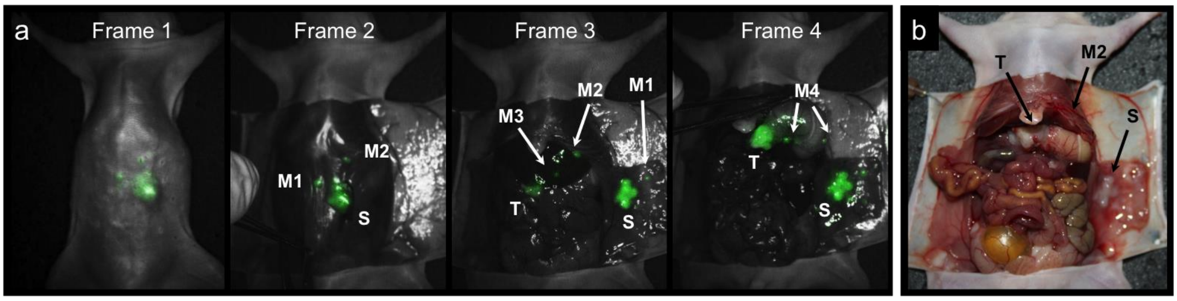

Figure 22: Cetux-800CW detects AsPC-1 primary tumor, the tumor mass at the surgical incision and metastases during fluorescence-guided dissection. (a) Representative movie-frames (Frame 1-4) recorded with the Quest Spectrum imaging system during fluorescence-guided dissection of a AsPC-1 tumor bearing mouse (n=5) 24 h after injection of 25 µg of Cetux-800CW, showing accumulation of the probe (green) within the primary tumor (T), at the tumor mass at the surgical incision (S), and within small metastases (M1-4). (b) Corresponding photograph of the same mouse with opened abdomen, showing macroscopic appearance of the primary tumor, of the tumor mass developed at the surgical incision and of the tumor lesion at the costal arch which is barely visible without fluorescence guidance.

In order to compare the distribution of Cetux-800CW to Cetux-Alexa-647 and exclude any interference of the dye in the localization of the probe, mice that received Cetux-800CW were analyzed by Optix MX2 *in vivo* before the fluorescence-guided dissection and *ex vivo* after fluorescence-guided dissection by imaging the excised organs, as previously performed with the mice that had received Cetux-Alexa-647. Figure 23a shows the *in vivo* Optix MX2 scan of the same mouse analyzed in Figure 22. Cetux-800CW derived fluorescence *in vivo* was specifically localized over the AsPC-1 tumor. Moreover, *ex vivo* scans confirmed the specificity of the fluorescence signal over primary tumor, the metastases, i.e. in the liver (arrow), and the infiltrated tumor mass at the surgical incision (scar; arrow) which was earlier detected during fluorescence-guided dissection (Figure 23b). The metastasis at the costal arch detected by fluorescence-guided dissection did not reveal any fluorescence signal by Optix MX2 scans. Fluorescence signal was also present over a retroperitoneal metastasis (not shown in Figure 22, but also detected during fluorescence-guided dissection), as well as infiltrating cells into the pancreas (arrow). A moderate fluorescence signal was also depicted over the whole healthy liver, which was neither observed with the Cetux-Alexa-647 probe, nor during fluorescence-guided dissection.

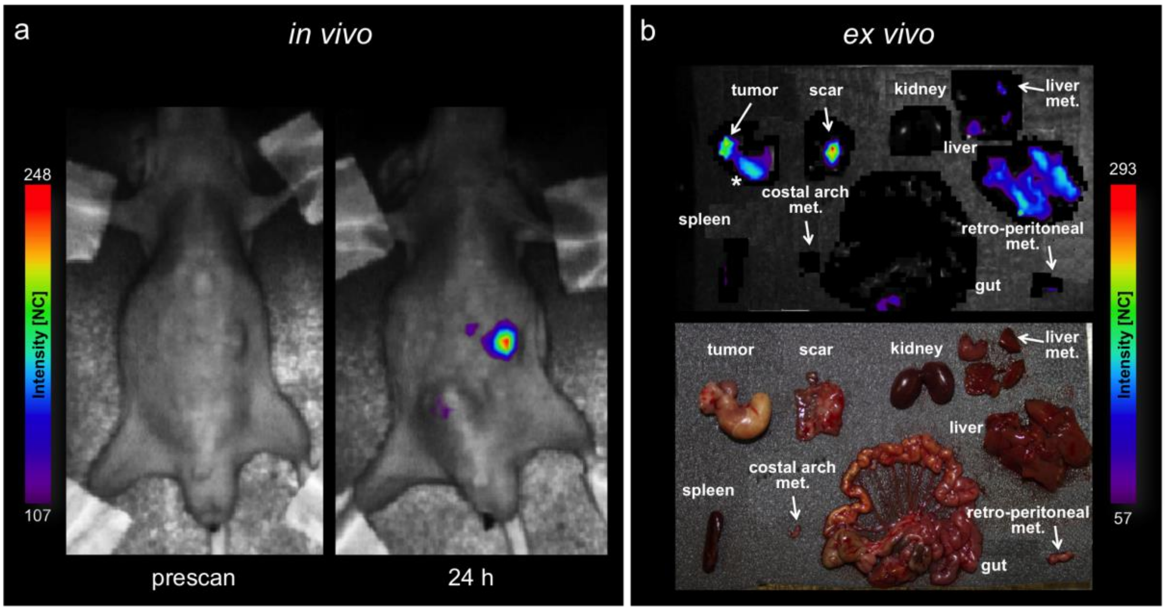

Figure 23: Cetux-800CW fluorescence signal detected over AsPC-1 primary tumor and metastases by *in vivo* and *ex vivo* NIRF imaging. The same AspC-1 bearing mouse undergoing fluorescence-guided section and presented in Figure 22 was scanned for NIRF imaging by Optix MX2. (a) Representative images of the *in vivo* prescan (the day before the fluorescence-guided surgery) and 24 h scan (just before the start of fluorescence-guided surgery) after Cetux-800CW injection reveal an accumulation of the probe specifically at the tumor site. (b) Representative images of *ex vivo* NIRF imaging obtained by Optix MX2 of extracted organs of the same mouse that was scanned *in vivo* by Optix MX2 and subsequently underwent fluorescence-guided dissection (Figure 22). Cetux-800CW derived signals were detected over the primary tumor, at the tumor mass developed at the surgical incision (scar), but also over small metastases located at the liver and in the retroperitoneum (white arrow). Cells infiltrating the stomach (asterisk) were also detected. The small metastasis at the costal arch did not show any fluorescence signal (white arrow). A low fluorescence signal was detected over the rest of the liver.

3.2.8 *Ex vivo* validation of Cetux-800CW fluorescence signals of tumor and metastases

As fluorophores emitting fluorescence in the range of 800 nm cannot be analyzed by our NIRF microscopes, Cetux-800CW derived fluorescence was further assessed on sections of AsPC-1 primary tumors and of metastatic sites using the Odyssey scanner. Figure 24a revealed that only the vital part of the primary tumor was stained with the i.v. injected Cetux-800CW (green), whereas the necrotic part in the tumor center, confirmed by HE staining (right panel; N) did not show any Cetux-800CW-derived fluorescence. Moreover, tumor cells that bound Cetux-800CW and invading the stomach (S) and the duodenum (D) were also clearly visualized by Odyssey (white arrow). Cetux-800CW-derived fluorescence was also found specifically at the tumor mass developed at the scar (Figure 24b), and at the two small (~1 mm) metastases present in the liver lobe (Figure 24c) as well as at the costal arch (Figure 24d), all sites that were previously detected by Quest Spectrum as shown in Figure 22.

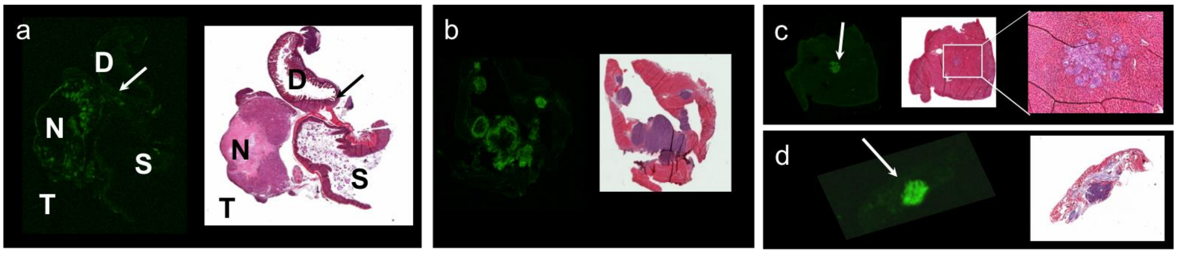

Figure 24: Confirmation of Cetux-800CW fluorescence signals at primary tumor and metastases by Odyssey system. (a) Odyssey scan of a representative primary AsPC-1 tumor (T) embedded together with adjacent stomach (S) and duodenum (D) (left) and corresponding HE staining (right). Cetux-800CW derived fluorescence (green) is observed at the vital part of the primary tumor and at the site of tumor invasion (arrow) into the stomach (S) and duodenum (D), but not at the necrotic area (N). (b-d) Odyssey scans and corresponding HE staining of tissue sections confirming the presence of Cetux-800CW derived fluorescence (b) at the tumor mass that developed at the surgical incision and at two small metastases (~1 mm) developed (c) at the liver and (d) at the costal arch. All the metastatic lesions were previously detected by fluorescence-guided surgery as shown in Figure 22.

Taken together, Cetuximab conjugated with NIRF dyes is a valuable tool to visualize not only the primary tumor but also very small metastatic lesions by NIRF imaging and by FGS.

3.3 Proof-of-Concept: Validation of treatment efficacy targeting EGFR in combination with NHE1 in the orthotopic AsPC-1 tumor mouse model

Next, the AsPC-1 tumor mouse model was applied to validate the efficacy of a novel therapeutic strategy, the combination of Erlotinib and Cariporide, on tumor growth, invasion and metastatic spread *in vivo*. Erlotinib is a target of EGFR, while Cariporide is a specific inhibitor of the activity of NHE1, a sodium/hydrogen exchanger, known to be implicated in the maintenance of the acidic tumoral pH. For this study the AsPC-1 tumor model was chosen which is characterized by the high aggressive tumor phenotype with invasion and metastatic spread. Earlier *in vitro* results had also demonstrated that inhibition of both, EGFR and NHE1 activity, by Erlotinib and Cariporide, respectively, reduced the formation of invadopodia in AsPC-1 cells (unpublished data, personal communication of Prof. Reshkin and colleagues, from University of Bari, Italy).

3.3.1 Treatment schedule of Erlotinib/Cariporide therapy in AsPC1 tumor bearing mice

To validate the efficacy of the combined Erlotinib/Cariporide therapy on tumor progression, treatment was started 10 days after transplantation. This time was chosen since at this time point we found that the primary AsPC-1 tumors presented an average volume of 7.9 ± 0.1 mm^3 (n=4), but no macroscopical appearance of invasion or metastatic spread into peritoneal organs as yet. Mice transplanted with tumor cells 10 days prior to the start of the experiment were randomly divided into four groups and treated following the therapeutic schedule shown in Figure 25: for 20 days they received daily either Erlotinib (50 mg/kg of body weight (BW) in Captisol 6%, orally, n=7) or Cariporide (3 mg/kg of body weight (BW) in NaCl 0.9%, i.p. n=7) or a combination of both (n=7) or the corresponding vehicles as controls (NaCl 0.9% i.p. and Captisol 6% orally; n=6).

All mice were sacrificed at day 30 after AsPC-1 cell transplantation, since at this time point untreated AsPC-1 mice usually developed an average primary tumor mass of 171 ± 118 mm^3 invading into the stomach and duodenum, with metastatic spread in different peritoneal organs.

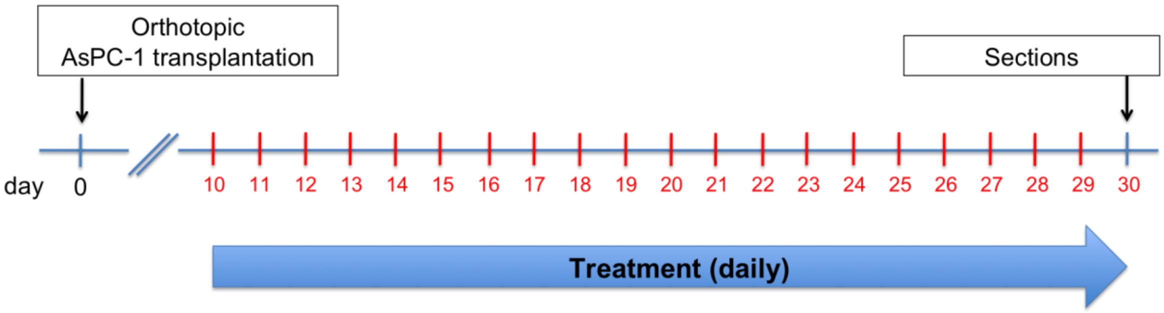

Group 1 n=7	Cariporide	3 mg/kg (3 µl/g) BW	i.p.
Group 2 n=7	Erlotinib	50 mg/kg (8.3 µl/g) BW	orally
Group 3 n=7	Cariporide	3 mg/kg (3 µl/g) BW	i.p.
	Erlotinib	50 mg/kg (8.3 µl/g) BW	orally
Group 4 (Control) n=6	NaCl 0.9%	* 3 µl/g BW	i.p.
	Captisol 6%	* 8.3 µl/g BW	orally

*Controls received volumes equivalent to the corresponding treatment

Figure 25: Time schedule and therapy groups of the Erlotinib/Cariporide therapy.

3.3.2 Tolerance of the treatment and effect on body weight of the mice

All treatment regimes were well tolerated by all mice. At the day of sacrifice, body weights of the animals were recorded and scored. As shown in Figure 26, the highest loss of body weight of ΔW_M = -4.7% ± 4.2% was observed in the group treated with Erlotinib alone. A minor loss in body weight was seen also in the control group (ΔW_M = -1.8% ± 10.5%) and in the Erlotinib/Cariporide- double treated group (ΔW_M = -1.2% ± 13.1%), although both groups showed relatively high standard deviations. Interestingly, the group treated with Cariporide alone showed even an increase in body weight (ΔW_M = +3.3% ± 8.0%).

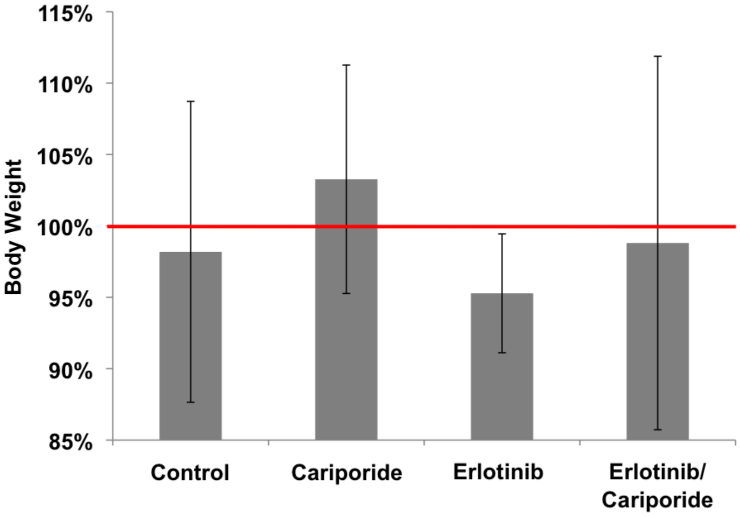

Figure 26: Effect of the combined Erlotinib/Cariporide therapy on body weight. The weight at the end of the therapy was calculated for all treatment groups as a percentage of the initial body weight. Red line marks 100% corresponding to unchanged weight. Mice of the control and the Erlotinib/Cariporide groups show similar average body weight measured before the dissection. In comparison to the control group, mice treated with only Cariporide show higher average body weights whereas Erlotinib-treated mice show a decrease in the body weight.

3.3.3 Effect of Erlotinib/Cariporide therapy on primary tumor growth

The influence of the different treatments on tumor growth was assessed by manually measuring primary tumor volumes with a caliper during section (Figure 27). No significant inhibitory effect on the tumor growth was observed in response to therapy, neither to Cariporide nor to Erlotinib given alone, nor to the combination of both drugs. However, mice treated with Cariporide alone developed a larger primary tumor (140 ± 16 mm^3) in comparison to the controls with an average primary tumor volume of 95 ± 27 mm^3. The highest variation in tumor volumes were found in the Erlotinib-treated group with an average tumor volume of 109 ± 34 mm^3 and tumor sizes that were comparable to those of controls. A slightly reduced primary tumor volume in comparison to the control group was found only for tumors that were treated with combined Cariporide/Erlotinib (80 ± 15 mm^3), although the difference was not significant ($p=0.27$).

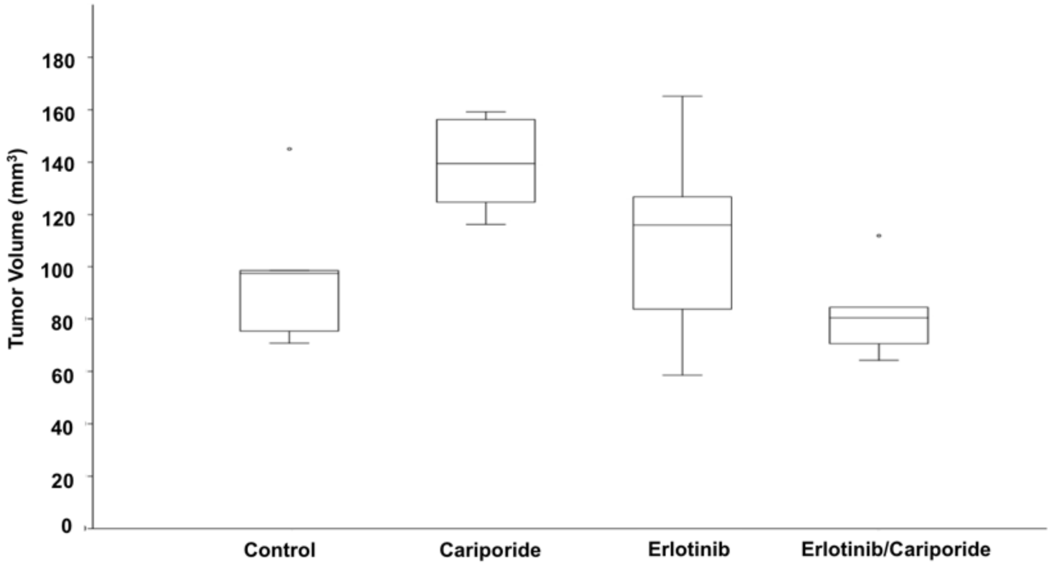

Figure 27: Effect of Erlotinib/Cariporide therapy on primary tumor growth. Primary tumor volumes (mm^3) of the mice of the different groups, measured with caliper during the dissection. In comparison to the control group (95 ± 27 mm^3), Cariporide-treated mice show a higher average tumor volume (140 ± 16 mm^3) whereas Erlotinib-treated mice show a slight increase in the average tumor volume, but with high variability (109 ± 34 mm^3). A slight decrease in the average tumor volume in comparison to the control group was seen in the Erlotinib/Cariporide-double treated group (80 ± 15 mm^3).

3.3.4 Effect of Erlotinib/Cariporide therapy on tumor infiltration into the stomach and duodenum

To evaluate the grade of invasion of tumor cells into adjacent organs such as stomach and duodenum in response to therapy in the AsPC-1 tumor mouse model, we stained the tumor cells in paraffin tumor sections immunohistochemically with anti-EGFR antibody. Tissue sections were taken from 4 different plains of the tumor mass embedded in paraffin blocks together with the adjacent organs such as stomach and part of the duodenum. As shown in the images of the histological sections in the upper panel of Figure 28 (upper part), EGFR staining identifies even small groups of tumor cells infiltrating the mucosa of the stomach and duodenum. The grade of invasion was scored according to the extent of tumor cells infiltrating the different layers (serosa, muscularis, mucosa) of duodenum and stomach, stained by anti-EGFR antibody (- = no infiltration; L = low infiltration, single tumor cells start to invade the serosa; M = medium infiltration, tumor cells invade the serosa and muscularis; H = high infiltration, tumor cells invade the mucosa).

As shown in Figure 28 (lower part), mice of the untreated control group showed a high infiltration grade into the stomach (5/6 mice) whereas most of the mice showed no tumor cell infiltration into the duodenum (4/5 mice). Treatment with Cariporide only resulted in primary tumors that showed infiltration into the stomach at different grades (2/7 mice with low, 3/7 mice with medium and 2/7 mice with high infiltration). The majority of Erlotinib-treated mice revealed primary tumors with a medium (4/7 mice) and high (2/7 mice) grade of infiltration into the stomach. In both Cariporide and Erlotinib-only treated groups, high infiltration in the duodenum was observed (4/6 mice and 4/7 mice, respectively). Instead, tumor tissue sections from combined Erlotinib/Cariporide-double treated mice showed that only two mice had high infiltration of tumor cells into the stomach, one had only low infiltration, whereas 3/7 mice revealed no infiltration at all. The grade of tumor infiltration in the duodenum of the double treated mice (5/7 mice with no infiltration, 2/7 mice with high infiltration) was found to be similar to the control group.

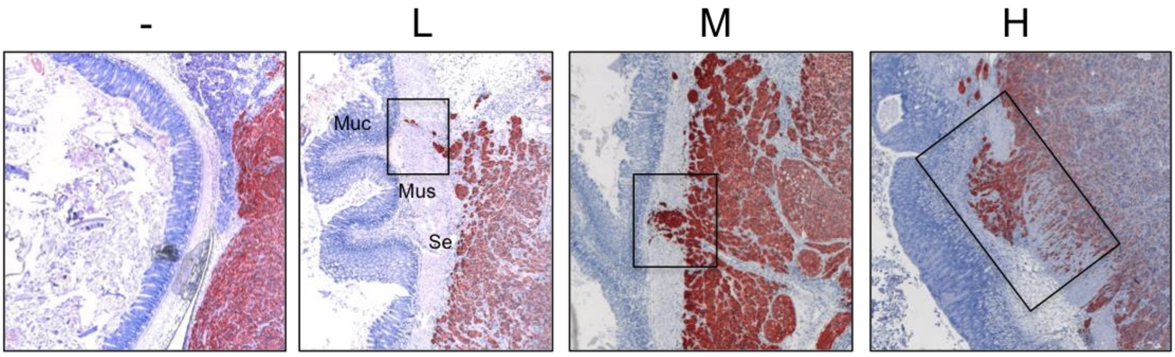

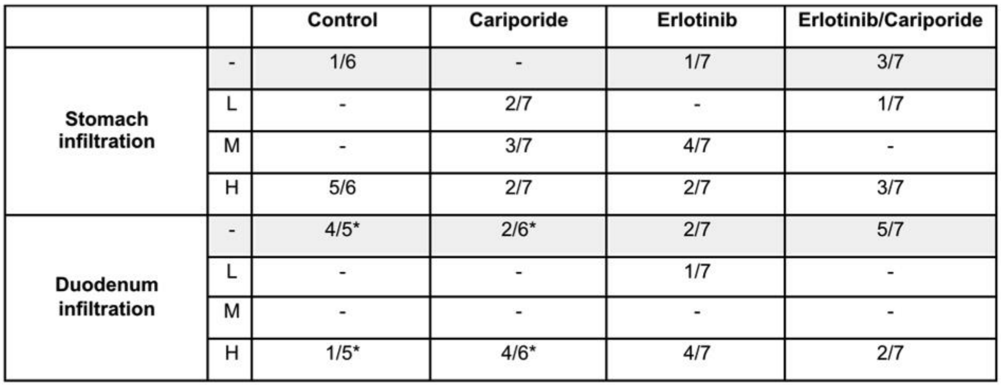

		Control	Cariporide	Erlotinib	Erlotinib/Cariporide
Stomach infiltration	-	1/6	-	1/7	3/7
	L	-	2/7	-	1/7
	M	-	3/7	4/7	-
	H	5/6	2/7	2/7	3/7
Duodenum infiltration	-	4/5*	2/6*	2/7	5/7
	L	-	-	1/7	-
	M	-	-	-	-
	H	1/5*	4/6*	4/7	2/7

* analysis of duodenum infiltration was not possible in one animal.

Figure 28: Analysis of the invasion grade of AsPC-1 tumor cells into the stomach and duodenum evaluated by EGFR staining. Squares depicted in the images show different amount of infiltration which was relatively quantified by scores. (0 = no infiltration; L = low infiltration, single tumor cells starts to invade the serosa; M = medium infiltration, tumor cells invade the serosa and muscularis; H = high infiltration, tumor cells invade the mucosa). Serosa (Se), muscularis (Mus) and mucosa (Muc) layers are exemplarily shown in the figure with low infiltration (L). 4 different slides of the primary tumor were evaluated for each model and the highest score was taken into account. Minor invasion of tumor cells into the stomach was only found in the Erlotinib/Cariporide treated group in comparison to the control group, whereas the invasion of the duodenum of the Erlotinib/Cariporide double treated mice was not affected. No effect was seen on the invasion of tumor cells in the stomach and duodenum in response to administration of either Cariporide alone or Erlotinib alone.

In conclusion, only the Erlotinib/Cariporide-double treated group revealed a minor effect on the invasion behavior by showing a reduced degree of infiltration into the stomach, whereas none of the treatments were efficient in altering invasion behavior into the duodenum.

3.3.5 Effect of Erlotinib/Cariporide therapy on metastatic spread

To evaluate the effect of Erlotinib and Cariporide alone or in combination on the metastatic load, peritoneal organs such as liver, spleen, kidney and diaphragm were macroscopically analyzed in all mice for the presence and number of metastases. The presence of tumor mass at the surgical incision was also recorded.

The results of the metastatic tumor spread in the different treatment groups are summarized in Table 8. In the control group, most of the mice presented metastatic lesions in the liver (3/6 mice), kidneys (3/6 mice), spleen (3/6 mice) and diaphragm (4/6 mice). The groups receiving the therapy with either Cariporide or Erlotinib showed equal numbers of mice with metastatic findings comparable to controls. For example, the Cariporide-treated group metastasized to the liver (4/7 mice), kidneys (4/7 mice) and spleen (4/7 mice). Only a minor reduction in the incidence of metastases was observed in the diaphragm (2/7 mice) of the Cariporide-treated mice in comparison to controls. In Erlotinib-treated mice, metastases were observed in the liver and diaphragm (4/7 mice), whereas less mice (2/7 mice) were observed with metastases in the spleen in comparison to the controls; kidneys were completely free of metastases. Cariporide and Erlotinib alone had no effect on the development of a tumor mass at the surgical incision site (4/7 mice) in comparison to the controls.

By contrast, Erlotinib/Cariporide-double treated mice showed a reduced metastatic spread with no metastases findings in the kidney and with a low number of metastases located in the liver (1/7 mice), and diaphragm (2/7 mice), when compared to the control group. The number of double treated mice with spleen metastases (3/7 mice) was comparable to the controls. Moreover, double treated mice did not develop as often a tumor mass at the surgical incision site (2/7 mice) when compared to the control group (4/6 mice).

Incidence of metastasis/ infiltration	Control (n=6)	Cariporide (n=7)	Erlotinib (n=7)	Erlotinib/Cariporide (n=7)
Liver	3/6 (50%)	4/7 (57%)	4/7 (57%)	1/7 (14%)
Kidneys	3/6 (50%)	4/7 (57%)	0/7 (0%)	0/7 (0%)
Spleen	3/6 (50%)	4/7 (57%)	2/7 (28%)	3/7 (43%)
Diaphragm	4/6 (66%)	2/7 (28%)	4/7 (57%)	2/7 (28%)
Site of surgical incision	4/6 (66%)	5/7 (71%)	4/7 (57%)	2/7 (14%)

Table 7: Effects of Erlotinib/Cariporide therapy on metastatic spread in AsPC-1 tumor bearing mice. Liver, kidney, spleen and diaphragm were analyzed for the presence of macroscopic metastases, together with infiltration of tumor cells at the site of surgical incision. The control group presents a high incidence of metastases (50-66%) in all considered organs as well as infiltration at the site of surgical incision. Erlotinib/Cariporide-double treatment showed a slight inhibitory effect on the metastatic spread to kidneys, liver and diaphragm and a slightly reduced number of mice with infiltration at the site of surgical incision.

The metastatic load in the mesentery was also evaluated in response to therapy in all groups (Figure 29). A high number of metastases with sizes of 1, 2 and 3 mm was observed in the control group in comparison to all treated groups. A strong reduction in mesenterial metastases was found in the Erlotinib/Cariporide-double treated group for all sizes of metastases, whereas a reduced number of metastases was found in both Cariporide- and Erlotinib-only treated mice, especially for metastases of sizes of 2 mm and 3 mm.

Cariporide and Erlotinib alone had no effect on the metastatic behavior of the tumor cells in the AsPC-1 model. However, Erlotinib/Cariporide applied together showed a minor inhibition of metastatic spread to the liver, kidneys and mesentery, and also reduced numbers of mice with infiltration of tumor cells to the site of surgical incision.

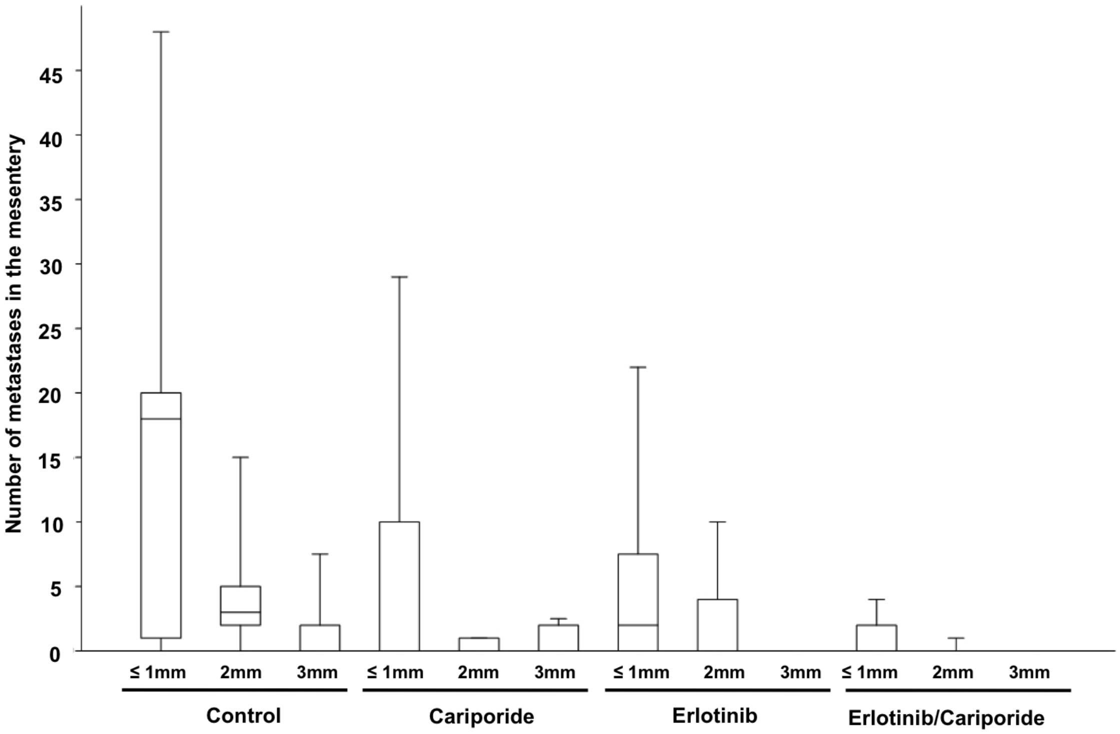

Figure 29: Effects of Erlotinib and Cariporide on the metastatic load in mesentery. During section, the mesentery of the animals was exposed and the number of macroscopic metastases was counted. A high decrease of metastases of different sizes (1mm, 2mm and 3mm) were observed in the Erlotinib/Cariporide-double treated mice in comparison to the controls. A minor reduction in number of metastases, especially of 2 mm and 3 mm, was found in the Cariporide- and Erlotinib- only treated groups.

Taken together, Erlotinib/Cariporide-double therapy did not affect the growth of the primary tumor, but showed some efficacy on steps of tumor progression such as reducing the invasion behavior of the tumor cells into the stomach and at the surgical incision, and inhibiting the metastatic spread to organs such as liver, kidney and mesentery.

4. Discussion

4.1 Orthotopic human PDAC mouse models with distinct growth and metastatic behavior

In the first part of my study, five orthotopic mouse models of human PDAC, each derived from different human pancreatic tumor cell lines were successfully established.

At the time when symptoms suggested PDAC growth (defined by us as time of development), all orthotopic PDAC mouse models developed PDAC tumors presenting macroscopic invasion into the stomach and duodenum, which is a characteristic tumor growth behavior also seen during the progression of PDAC in humans. PDAC tumors developed at different time points after cell transplantation, with tumor take rates between 75% and 100% depending on the transplanted cells, with strong differences in tumor size. MIA PaCa-2 and Capan-1 transplanted mice developed tumors after ~90 and ~120 days respectively, with much larger tumor masses in comparison to the other three PDAC models, and varying highly in tumor sizes (845 ± 428 mm^3 and 1183 ± 812 mm^3) in comparison to the other three. In fact, BxPC-3 and PANC-1 transplanted mice developed smaller tumor masses (193 ± 111 and 294 ± 194 mm^3) after ~90 and ~115 days, respectively, whereas the AsPC-1 model was the only one among the five tested, that developed tumors of 122 ± 93 mm^3 in size in a very short period of 30 days after cells transplantation. Moreover, the AsPC-1 model, with a tumor take rate of 100%, showed an aggressive phenotype with high metastatic spread in various peritoneal organs in agreement with previous studies reporting AsPC-1 as a highly aggressive cell line *in vivo* [88, 89]. In contrast, we showed that the MIA PaCa-2 model revealed almost no peritoneal metastatic spread, however with common invasion of tumor cells into the liver hilus, occasionally resulting in jaundice. These findings demonstrate that AsPC-1 and MIA PaCa-2, resemble a metastatic tumor spread typical of PDAC but with two different characteristic grades of dissemination, one with a high metastatic (AsPC-1) phenotype and one with a low metastatic (MIA PaCa-2) phenotype. Altogether, these results indicate that there is no linear correlation between the tumor size, the grade of differentiation, and the aggressiveness of the models, but all strongly depend on the intrinsic characteristic of the transplanted cells. It is of interest to observe that only the AsPC-1 mouse model, which is the only one derived from the ascites of a PDAC patient, shows a high aggressive phenotype with a very short time of development and metastatic spread. This also suggests that the metastatic spread is not due to a possible microscopical cell leakage during operation as reported by others [90], which may overestimate the number of metastatic findings in mice in comparison to the human disease.

Moreover, histological analysis revealed that each orthotopic PDAC mouse model established here reflected characteristic morphological and pathological features, such as desmoplastic reaction, a hallmark of human pancreatic cancer. AsPC-1, MIA PaCa-2 and PANC-1 xenografts presented a poorly undifferentiated morphology with completely unorganized tumor cells, although the transplanted cells derived from different origins, ascites of a PDAC patient (AsPC-1) and from a PDAC tumor of a patient with signs of metastases (MIA PaCa-2 and PANC-1). By contrast, BxPC-3 and Capan-1 differentiated tumors are both characterized by tumor cells organized in clusters. Especially Capan-1 tumors, which were derived from a liver metastasis of a PDAC patient, closely resemble the duct-like morphology typical for human PDAC. Our histological findings of the grade of differentiation of the tumors were already described by others, that applied the PDAC mouse models for preclinical imaging or therapeutic studies mainly using Capan-1 [91], BxPC-3 [92], AsPC-1 [93], MIA PaCa-2 and PANC-1 [94] mouse models. However, the majority of the researchers used subcutaneous tumor models, which usually show faster tumor growth rates and no invasion and metastatic spread [95].

Similar amounts of PSCs were present in all primary PDAC tumors with comparable myofibroblastic-like morphology. Instead, a high amount of deposition of elongated collagen fibers, resembling the fibrotic reaction typical of human PDAC, was only found in the Capan-1 model, whereas all others developed a fibrotic reaction as well, however to a minor degree. PSCs and collagen fibers were located around the duct-like- or round clusters of the differentiated Capan-1 and BxPC-3 tumors, respectively, whereas the poorly differentiated models (AsPC-1, MIA PaCa-2 and Panc-1) revealed the presence of disperse and unorganized PSCs, together with elongated collagen fibers, all over the tumor among the cells. The presence of PSCs and collagen in PDAC mouse models such as Capan-1 [96], MIA PaCa-2 and PANC-1 [94] has been described by positive staining of α-SMA and/or collagen before but only on subcutaneous PDAC tumors. Similar to these previous results, we found strong staining with α-SMA and Sirius Red in the same peri-tumoral regions, confirming that mouse PSCs are the major producers of collagen not only in human PDAC [11] but also in PDAC xenografts. Moreover, the finding of elongated collagen fibers found here in all PDAC models is in agreement with previous observations that collagen fibers, which are typically curly and anisotropic in normal tissue, progressively thicken and linearize following tumor initiation [97]. Since it has been already proven that fibrotic reaction impedes the diffusion of intravenously injected molecules throughout the tumor tissue [98], collagen deposition and presence of PSCs have to be carefully analyzed before choosing the PDAC mouse model for preclinical imaging or therapeutic evaluation.

Therefore, it is clear that orthotopic mouse models derived from a single cell line do not represent the complexity of clinicopathological properties seen in practice in human disease, but each model can exploit a specific pathological characteristic of the disease. In fact, only scarce data are present in the literature for the characterization and comparison of tumor mass progression and timing of development of the different PDAC mouse models [24, 25]. A comparison of these studies with the data obtained here is very difficult, due to the different amount of tumor cells transplanted and to the different transplantation sites performed by others. For example, here, transplantation of $1x10^6$ cells into the more proximal (head) part of the pancreas was performed, obtaining in all models a structured tumor mass in an adequate period of time. By comparison, Hotz and colleagues transplanted a much higher number of AsPC-1, Capan-1 and MIA PaCa-2 tumor cells ($1x10^7$) into the tail of the pancreas [24]. Instead, Loukopoulos and colleagues [25], transplanted orthotopically the same quantity of Capan-1, Panc-1, AsPC-1 and BxPC-3 cells as in this study, but they did not report any data for the timing of development and tumor volumes. Both studies showed peritoneal dissemination and metastases to liver, lungs and lymph nodes, each PDAC tumor model to a different extent, as was observed in the present study using AsPC-1 and MIA PaCa-2 mouse models.

Along with the orthotopic or subcutaneous transplantation of cells, another established technique for developing orthotopic PDAC mouse models is the transplantation of small tumor fragments (called tumor grafts) derived from biopsies of human patients or from subcutaneous tumors in animals. Different groups demonstrated that mice undergoing this procedure developed primary tumors with characteristic features similar to those of the donor [20, 21]. However, the heterogeneity of cells presented in surgical biopsies (i.e. tumor- , stromal- , inflammatory- cells), together with the development of necrotic areas of different extent, makes this approach highly variable and therefore not the best choice for diagnostic and therapeutic ends.

Overall, PDAC orthotopic bearing mice constitute a powerful preclinical platform, which has been already used in a number of studies on PDAC, for evaluating novel probes for imaging [93, 99, 100], for testing the effect of new treatment protocols [101] as well as for analyzing the behavior of the disease such as the interaction between PSCs and tumor cells [102].

4.2 NIRF labeled Cetuximab as a tool for fluorescence-guided surgery

The results obtained in the second part of my study are the first to show the potential of the FDA approved therapeutic antibody Cetuximab targeting the human EGFR, labeled with NIRF dyes, to detect pancreatic tumors and metastatic nodules in PDAC xenografts in mice in combination with non-invasive *in vivo* and *ex vivo* NIRF imaging and fluorescence-guided dissection.

4.2.1 Visualization of PDAC primary tumors and metastases with Cetux-Alexa-647 by NIRF imaging

By using 2D NIRF imaging in PDAC mouse models that develop tumors with different EGFR expression, AsPC-1 (high and homogenous EGFR expression) and MIA PaCa-2 (high/low and heterogeneous expression), we demonstrated that Cetux-Alexa-647 accumulates solely at the AsPC-1 and MIA PaCa-2 primary tumor sites whereas the control human hIgG-Alexa-750 localized only in the liver, with a maximum fluorescence for both antibodies observed 24 h after probe injection. This is in line with results of a previous study performed by our group using radiolabeled Cetuximab in combination with SPECT, that showed that the best time point to visualize the antibody *in vivo* is 24 h after i.v. probe injection, giving the antibody sufficient time to accumulate at the tumor site [103].

The specificity of Cetux-Alexa-647 and hIgG-Alexa-750 derived fluorescence detected *in vivo* was confirmed by comparing their fluorescence LTs *in vivo* at 24 h with the LTs of the probes dissolved in medium. Slightly higher LT values of Cetux-Alexa-647 and hIgG-Alexa-750 derived fluorescence were measured *in vivo* over the tumor area which is in agreement with our previous observations, showing that the LT of fluorescently labeled antibodies, e.g. antibody targeting matriptase, can be slightly influenced by *in vivo* conditions, such as the presence of serum proteins in the blood [93].

By an *in vivo* multimodality approach using fluorescence tomography data co-registered with µCT, the shape and the exact 3D location of the fluorescent AsPC-1 pancreatic tumor targeted by Cetux-Alexa-647 was perfectly identified in relation to the gastrointestinal tract. This indirect approach is of high importance especially for studies involving PDAC models, since pancreatic tumors are not visible by palpation or by inspecting just the outer appearance of the mouse. A similar multiplex approach was used by our group to visualize PDAC xenografts [93] using 2D *in vivo* NIRF images of a fluorescently labeled anti-matriptase antibody co-registered with 3D-CT data. The 3D visualization of PDAC was also obtained by Hudson and colleagues [104] using a fluorescently labeled EGF in combination with multispectral optoacustic tomography (MSOT), with the main limitation that optoacustic technology does not have a sufficient field of view (FOV) to accommodate the reconstruction of the entire size of a mouse.

Ex vivo NIRF imaging of the opened abdominal cavity of AsPC-1 and MIA PaCa-2 transplanted mice and of the explanted organs of the mice confirmed that *in vivo* applied Cetux-Alexa-647, but not the hIgG-Alexa-750, specifically accumulates at AsPC-1 and MIA PaCa-2 primary tumors. Furthermore, in the highly metastatic AsPC-1 model, Cetux-Alexa-647 is able to detect metastatic lesions as small as 1 mm, whereas in the low metastatic MIA PaCa-2 tumor bearing mice, usually no additional accumulation of the Cetux-Alexa-647 was observed than at the primary tumor.

Quantification of the *ex vivo* average fluorescence intensities over the primary tumors, showed that uptake of Cetux-Alexa-647 by high EGFR-expressing AsPC-1 primary tumors was significantly higher than the moderate EGFR-expressing MIA PaCa-2 primary tumors, whereas negligible hIgG-Alexa-750 derived control signals were measured over both, AsPC-1 and MIA PaCa-2 primary tumors. The moderate fluorescence signals measured over the MIA PaCa-2 primary tumors reflect the heterogeneous expression of EGFR observed throughout the MIA PaCa-2 primary tumor sections. Low expression of EGFR was observed in different areas within the tumor mass, whereas tumor cells in the vicinity or already invading stomach and duodenum showed upregulation of EGFR, in accordance with previous data showing that EGFR promotes metastases of human pancreatic cancer [48]. By contrast, a homogenous high EGFR expression was seen in the AsPC-1 tumor.

By NIR fluorescence microscopy of tumor tissue sections from mice co-injected with Cetux-Alexa-647 and hIgG-Alexa-750, we showed that in both tumor models, AsPC-1 and MIA PaCa-2, not all EGFR-expressing tumor cells bound detectable levels of the intravenously injected Cetux-Alexa-647. This might be due to the poor vascularization of the pancreatic tumor, which may simply prevent the sufficient transport of Cetuximab to all tumor cells. Moreover, the high affinity of Cetuximab, together with its large size of 150 kDa may also influence its extravasation and diffusion into the less-vascularized regions [105]. Nevertheless, the inhomogeneous binding of Cetux-Alexa-647 within the tumor does not seem to have a significant impact on the detection capacity of tumor lesions by *in vivo* or *ex vivo* NIRF imaging. Visualization of PDAC by targeting EGFR has not yet been performed, but different groups were already able to visualize PDAC in combination with *in vivo* and *ex vivo* NIRF by targeting highly expressed cell receptors on PDAC such as carbohydrate antigen 19.9 (CA 19.9) [106], mucin-1 (MUC-1) [107] and matriptase [93]. Another interesting approach detected Capan-2 xenografts using pH sensitive probes [99]. However, an essential limitation of all these studies is that the preclinical probes employed will be difficult to translate into the clinic due to the possible toxicity of the preclinical dyes used (i.e. Alexa Fluor Dyes).

4.2.2 Identification of AsPC-1 primary tumor and metastatic sites with Cetux-800CW by fluorescence-guided dissection

Visualization of primary tumor and identification of multiple metastatic nodules as small as 1 mm was realized by using Cetux-800CW during *ex vivo* fluorescence-guided dissection of high EGFR-expressing and metastatic AsPC-1 xenografts. High Cetux-800CW signals over the tumor area were detected even through the intact skin of the mice despite the inhomogeneous lighting conditions of the open camera, known to cause a lower detection efficacy compared to the preclinical systems [108]. Optix MX2 scans of the same mice, injected with Cetux-800CW and undergoing fluorescence-guided dissection, confirmed the localization of Cetux-800CW *in vivo* and *ex vivo* at the AsPC-1 primary tumor and metastatic sites. Of note, a low Cetux-800CW *ex vivo* signal was depicted over the healthy liver, which was absent in the Cetux-Alexa-647 scans. This can be explained by the superior tissue penetration of the long-wavelength light (~800 nm) to the shorter wavelength light (~647 nm) used to excite the fluorescence probes. However, it is clear that the hepatic signal did not interfere with the detection of Cetux-800CW at the primary tumor and metastases, neither by NIRF imaging nor during fluorescence-guided dissection.

Odyssey scans confirmed the specificity of Cetux-800CW that binds exclusively to the tumor cells but does not accumulate within the necrotic areas of the tumors, as also recently described for clinical samples [109]. The presence of necrosis in the tumor does not impede the visualization of the surgical margins, since the vital tumor cells targeted by the fluorescently labeled Cetuximab are mainly located at the periphery of the tumor.

Until now, there has only been a single preclinical study describing the application of the Quest Spectrum clinical system for the detection of preclinical tongue tumors and of sentinel lymph nodes in mice [110]. The same report also showed results of a clinical trial, using Quest Spectrum for the detection of human colorectal liver metastases that were located near or at the liver surface, 24h after injection of ICG. Two other FDA-approved intraoperative fluorescence imaging systems, SPY and FLARE, were used in preclinical studies in combination with different therapeutic monoclonal antibodies labeled with IRDye-800CW, e.g for the surgical resection of breast cancer [111], HNSCC [112], and for the visualization of pancreatic xenografts using a CEA-targeting single-chain antibody fragment [113]. Moreover, a laparoscopic preclinical approach of pancreatic surgery, which was performed by Bouvet and colleagues [114, 115], involved anti-CEA antibody labeled with Alexa Fluor 488 dye. Although this approach seemed to be promising, similarly in this case the clinical translation will be difficult due to the possible toxicity of preclinical Alexa Fluor dyes and because the antibodies used were not FDA-approved.

The choice to use the FDA approved Cetuximab antibody and the IRDye-800CW, which is currently in the process for clinical translation, was therefore reasoned as this fluorescence conjugate may have the best prospect for clinical approval, which requires that each component of the probe on trial must be verified individually for its toxicity. The likelihood of approval thus falls the more multi-componential the probe is.

4.3 Anti metastatic effect of NHE1 and EGFR inhibition in PDAC xenografts

In the third part of my study, AsPC-1 xenografts, characterized by a fast development of a poorly differentiated primary tumor that invades into the surrounding organs and metastasizes to multiple sites in the abdomen, were employed to evaluate the efficacy of a combined anti-EGFR/anti-NHE1 therapy involving Erlotinib (50 mg/kg) and Cariporide (3 mg/kg). The major and most relevant effect of the combined Erlotinib/Cariporide- therapy was found in the inhibition of the metastatic spread to different peritoneal organs, especially to liver, kidney, diaphragm, mesentery and in the tumor infiltration at the site of surgical incision. Moreover, the combined therapy was able to reduce the tumor infiltration in the stomach of the mice. By contrast, both, Erlotinib and Cariporide administered as individual treatments, only had a very low effect on the metastatic spread to the kidney and to the diaphragm, respectively.

The major challenge for the analysis of the effect of the therapy on the metastatic spread was the quantification of the effect of the different drugs. This was due to the fact that most of the organs analyzed displayed a number of metastases in the range of 1-4 and of different sizes (1-3 mm) making the comparison of the different groups difficult. The decision to categorize the mice either as negative or as positive for the presence of macroscopic metastases in the analyzed organ, independently of their number and sizes, allowed us though to visualize the clear difference between the groups. Moreover, by counting the number of metastases of different sizes (1mm, 2mm and 3 mm), we could clearly show the inhibitory effects of the combined treatment on the mesenterial tumor spread.

Another slight (though not significant) effect of Erlotinib/Cariporide- double therapy was seen in the reduction of the tumor mass (average tumor mass 80 ± 15 mm^3) in comparison to control mice (average tumor mass 95 ± 27 mm^3), whereas the separate treatments had very different effects, from even an increase of the average tumor mass (average tumor mass 140 ± 16 mm^3) seen in Cariporide-treated mice, to a highly variable effect seen for the Erlotinib-treated mice, characterized by tumor masses ranging between 60 and 160 mm^3. The lack of effect of the individual treatments and low effect of the combined treatment on the growth of the AsPC-1 primary tumors was not a surprise, because molecules such as Cariporide and Erlotinib usually act only as sensitizers for other chemotherapeutic drugs, such as Gemcitabine which have a much stronger cytotoxic effect [22]. In the present study we only wanted to investigate an alternative way to promote the effect of Erlotinib. Any further variables such as chemotherapeutic drugs were not investigated. Nevertheless, the high variability of the primary tumor mass measured in the Erlotinib-treated mice, may indicate the requirement of a precise longitudinal visualization of the tumor mass with a non-invasive imaging technique such as MRI at regular time points prior to and during the course of the therapy. Here, mice were randomly assigned to the treatment groups at day 10. At this time the average tumor volumes, measured in an additional group of animals sacrificed at day 10 was 7.9 ± 0.1 mm^3 and showed only a low variability. Nevertheless, the implementation of an additional imaging technology would help not only to assess the exact tumor volumes at the beginning of the therapy but also to monitor tumor progression over time in response to the therapy and to visualize the possible causes of the variability.

The very low efficacy of the Erlotinib-only therapy also on the metastatic spread may be due to a form of resistance of the tumor cells. One of the key elements in this case could be attributed to the KRAS mutation, crucial for the EGFR- signaling pathway, which could limit the downstream effect of Erlotinib. This might be relevant in this study, since AsPC-1 cells are known to carry the KRAS mutation [116]. In fact, it has been shown by Larbouret and colleagues [117] that Capan-1 pancreatic cells characterized also by the KRAS mutation ($KRAS^{mut}$), subcutaneously injected in nude mice did not respond to a double therapy with Erlotinib (100 mg/kg) and Trastuzumab, whereas the BxPC-3 cell line ($KRAS^{wt}$) did. AsPC-1 cells were chosen for this study despite having the mutated KRAS, because of their much higher EGFR expression in comparison to the $KRAS^{mut}$ Capan-1 cells, as demonstrated in the first part of my study and, therefore, expected to be more responsive to EGFR targeting.

Moreover, it is known that EGFR-targeting therapeutic approaches, although very promising in treatment of NSCLC or colorectal cancer, seem to be less effective for treatment of PDAC [118]. In PDAC, single EGFR inhibition is typically not sufficient to abort critical signaling pathways, as most probably EGFR-signaling is not the only pathway for proliferation of the disease. For this reason, more recent studies have started focusing on combining TKIs based-therapies with other drugs targeting either other interaction partners of EGFR, or downstream effectors of the EGFR pathway, thus boosting the anti-tumor effect. As cited above, others have used Erlotinib (100 mg/kg) for pancreatic tumor therapy in combination with the anti-HER2 antibody Trastuzumab, a combination which proved to have a positive effect on pancreatic tumor bearing mice transplanted with KRas^{wt} cells. Moreover, Gefitinib, a TKI similar to Erlotinib, proved to inhibit the incidence of PDAC in genetically engineered mice, when used in combination with Licofelone, a dual inhibitor of 5-LOX-COX (Cyclooxygenase-2 and 5-Lipoxygenase) [119]. This underlines the need for alternative biological targets to be employed in combination with Erlotinib. In this respect, use of Cariporide as an inhibitor of NHE1 would not only target the recently proposed EGFR-NHE1 axis but would also act on the pH-driven metastasis, in which NHE1 is a pivotal regulator, and would thus potentially avoid the limitation of EGFR single-treatment in PDAC.

Neither Cariporide nor the combination of Erlotinib with Cariporide has as yet been investigated in any tumor model. No previous data have been published on the anti-tumor efficacy of Cariporide *in vivo*, but the same dose as used here (3 mg/kg) has shown a cardioprotective effect in rat models of cardiac arrhythmias and infarction [120]. Although Cariporide revealed an anti-proliferative and anti-metastatic effect *in vitro* in different PDAC cell lines [73], no corresponding results were seen here *in vivo* in inhibiting the metastatic spread in the Cariporide-only treated group. Since Cariporide has been tested for clinical translation and its safety confirmed at different concentrations (20, 80, or 120 mg, 3 times a day) [121], future studies may involve increasing the dose of Cariporide given to the animals in combination with Erlotinib to examine a potential enhancement of the metastatic inhibition. Such a study may also be supported by the positive effect we saw on the body weight of Cariporide-only treated animals, as opposed to mice treated with Erlotinib, which showed a reduction of body weight, due to the common side effect of high-dosed Erlotinib (100-150 mg/kg daily) [117]. The fact that the body weights in the Erlotinib/Cariporide combination treated mice were similar to those of controls, might indicate a protective role of Cariporide on the systemic toxicity of Erlotinib.

The mechanisms responsible for the effects of the Erlotinib/Cariporide-combination on the metastatic spread may be attributed to the inhibition of the tyrosine kinase of EGFR expressed on the membrane of AsPC-1 cells and the parallel inhibition of NHE1, an important down-stream effector of EGFR. Moreover, the inhibition of NHE1 on AsPC-1 cells would increase the acidic pH present in the surrounding of these extremely aggressive cells, which might secondarily inhibit their infiltration and the metastatic spread. However, the precise mechanisms of the *in vivo* interaction of both drugs with tumor cells have yet to be elucidated.

5. Summary and Conclusions

This study presents first a detailed comparative characterization of *in vivo* development, morphology and stroma features of five human PDAC xenografts that developed within the head of the pancreas in immunodeficient mice. Orthotopic transplantation of mice of five human PDAC cell lines (AsPC-1, MIA PaCa-2, PANC-1, BxPC-3 and Capan-1) with known grade of differentiation resulted in tumor formation, each after different time from the transplantation and each with invasion into stomach and duodenum, both hallmarks of the human PDAC. Moreover, detailed analysis of two poorly differentiated PDAC models, AsPC-1 and MIA PaCa-2, showed that they both have metastatic capacity, but to a different extend, AsPC-1 showing a high and MIA PaCa-2 a low metastatic spread. Among all primary tumors only the Capan-1 differentiated tumors consisted of the classic duct-like structure also seen in human PDAC. Round clusters of tumor cells were found in the BxPC-3 moderately differentiated tumors whereas all other tumors were composed of unorganized tumor cells. Presence of PSCs and collagen in the peri-tumoral areas was confirmed within the primary tumors of all mouse models, with much higher collagen deposition in Capan-1 differentiated tumors in comparison to all the others. The comparison of the different mouse models obtained in the first part of my study, demonstrate that each xenograft analyzed, reflects specific morphological and aggressive characteristics of the human disease, which help the selection of the best model for further studies.

AsPC-1 and MIA PaCa-2 mouse models, characterized by different EGFR expression and metastatic behavior, were chosen for further investigation of the suitability of intravenously injected Cetuximab-NIRF dye conjugates for NIRF imaging and fluorescence-guided dissection. We showed for the first time that Cetux-Alexa-647 and Cetux-800CW localized at PDAC primary tumors and metastatic sites. Therefore, Cetuximab-dye conjugates might be a useful tool in clinical settings for fluorescence-guided cancer surgery that could lead to significant improvements in the resection of tumors. Although this approach provides a valuable tool to address positive margin rates and metastatic spread it is not without limitations. As not all pancreatic tumors express EGFR and especially because clinical settings are much more complex and inhomogeneous than the preclinical models, further studies in order to evaluate different monoclonal antibodies for tumor targeting should follow, aiming at the development of a probe “cocktail” that can be applied to the patients in order to label every single tumor cell.

The highly metastatic AsPC-1 model was selected for testing a novel therapeutic strategy, the combined inhibition of NHE1 by Cariporide and of EGFR by Erlotinib, We show that the Erlotinib/Cariporide-double treatment has an effect on the metastatic spread of highly aggressive PDAC cells in different peritoneal organs and on the infiltration of tumor cells within the stomach and at the surgical incision. We believe that this reduction in metastatic load occurs primarily via inhibition of the NHE1-EGFR axis. However, the quantification of the numbers of metastases in the different organs and the high variability of metastases within each group was challenging. Undoubtedly, further animal studies are needed to establish the full efficacy of treatment on the metastatic reduction. Since this drug regime did not have any effect on the primary tumor mass, further studies employing chemotherapeutic drugs (i.e. Gemcitabine) in combination with these sensitizers are needed to further design a possible therapeutic regime for the application in the clinic. Finally, in addition to the a kras^{mut} cell line (AsPC-1) that we have employed, a further evaluation of the combined therapy should be performed with a kras^{wt} cell line, to evaluate a potentially stronger effect on the metastatic spread of Erlotinib alone or in combination with Cariporide.

Overall, this study confirms that PDAC orthotopic bearing mice are useful tools for testing novel imaging and therapeutic strategies, as well as for studying the pathophysiology of the disease, such as expression of tumor markers and stroma interaction.

Bibliography

1. Longnecker, D.S., *Anatomy and Histology of the Pancreas.* Pancreapedia: Exocrine Pancreas Knowledge Base, 2014.
2. Reichert, M. and A.K. Rustgi, *Pancreatic ductal cells in development, regeneration, and neoplasia.* J Clin Invest, 2011. **121**(12): p. 4572-8.
3. Luttges, J., et al., *Rare ductal adenocarcinoma of the pancreas in patients younger than age 40 years.* Cancer, 2004. **100**(1): p. 173-82.
4. Raimondi, S., P. Maisonneuve, and A.B. Lowenfels, *Epidemiology of pancreatic cancer: an overview.* Nat Rev Gastroenterol Hepatol, 2009. **6**(12): p. 699-708.
5. Lowenfels, A.B. and P. Maisonneuve, *Risk factors for pancreatic cancer.* J Cell Biochem, 2005. **95**(4): p. 649-56.
6. Takada, R., et al., *Duodenal Hemorrhage from Pancreatic Cancer Infiltration Controlled through Combination Therapy with Gemcitabine and S-1.* Case Rep Gastroenterol, 2014. **8**(2): p. 221-6.
7. Wolfgang, C.L., et al., *Recent progress in pancreatic cancer.* CA Cancer J Clin, 2013. **63**(5): p. 318-48.
8. Ahlgren, J.D., *Epidemiology and risk factors in pancreatic cancer.* Semin Oncol, 1996. **23**(2): p. 241-50.
9. Freelove, R. and A.D. Walling, *Pancreatic cancer: diagnosis and management.* Am Fam Physician, 2006. **73**(3): p. 485-92.
10. Kloppel, G. and N.V. Adsay, *Chronic pancreatitis and the differential diagnosis versus pancreatic cancer.* Arch Pathol Lab Med, 2009. **133**(3): p. 382-7.
11. Apte, M.V., et al., *Desmoplastic reaction in pancreatic cancer: role of pancreatic stellate cells.* Pancreas, 2004. **29**(3): p. 179-87.
12. Xu, Z., et al., *Role of pancreatic stellate cells in pancreatic cancer metastasis.* Am J Pathol, 2010. **177**(5): p. 2585-96.
13. Xu, Z., et al., *Pancreatic cancer and its stroma: a conspiracy theory.* World J Gastroenterol, 2014. **20**(32): p. 11216-29.
14. Fatima, J., et al., *Pancreatoduodenectomy for ductal adenocarcinoma: implications of positive margin on survival.* Arch Surg, 2010. **145**(2): p. 167-72.
15. Rau, B.M., et al., *R1 resection in pancreatic cancer has significant impact on long-term outcome in standardized pathology modified for routine use.* Surgery, 2012. **152**(3 Suppl 1): p. S103-11.
16. Regine, W.F., et al., *Fluorouracil vs gemcitabine chemotherapy before and after fluorouracil-based chemoradiation following resection of pancreatic adenocarcinoma: a randomized controlled trial.* JAMA, 2008. **299**(9): p. 1019-26.
17. Oettle, H., et al., *Adjuvant chemotherapy with gemcitabine vs observation in patients undergoing curative-intent resection of pancreatic cancer: a randomized controlled trial.* JAMA, 2007. **297**(3): p. 267-77.
18. Burris, H.A., 3rd, et al., *Improvements in survival and clinical benefit with gemcitabine as first-line therapy for patients with advanced pancreas cancer: a randomized trial.* J Clin Oncol, 1997. **15**(6): p. 2403-13.
19. Andersson, R., et al., *Gemcitabine chemoresistance in pancreatic cancer: molecular mechanisms and potential solutions.* Scand J Gastroenterol, 2009. **44**(7): p. 782-6.

20. Sun, C., et al., *Does gemcitabine-based combination therapy improve the prognosis of unresectable pancreatic cancer?* World J Gastroenterol, 2012. **18**(35): p. 4944-58.
21. Ansari, D., A. Gustafsson, and R. Andersson, *Update on the management of pancreatic cancer: surgery is not enough.* World J Gastroenterol, 2015. **21**(11): p. 3157-65.
22. Warsame, R. and A. Grothey, *Treatment options for advanced pancreatic cancer: a review.* Expert Rev Anticancer Ther, 2012. **12**(10): p. 1327-36.
23. Moore, M.J., et al., *Erlotinib plus gemcitabine compared with gemcitabine alone in patients with advanced pancreatic cancer: a phase III trial of the National Cancer Institute of Canada Clinical Trials Group.* J Clin Oncol, 2007. **25**(15): p. 1960-6.
24. Hotz, H.G., et al., *An orthotopic nude mouse model for evaluating pathophysiology and therapy of pancreatic cancer.* Pancreas, 2003. **26**(4): p. e89-98.
25. Loukopoulos, P., et al., *Orthotopic transplantation models of pancreatic adenocarcinoma derived from cell lines and primary tumors and displaying varying metastatic activity.* Pancreas, 2004. **29**(3): p. 193-203.
26. Alves, F., et al., *An orthotopic model of ductal adenocarcinoma of the pancreas in severe combined immunodeficient mice representing all steps of the metastatic cascade.* Pancreas, 2001. **23**(3): p. 227-35.
27. Bernsen, M.R., et al., *Biomarkers in preclinical cancer imaging.* Eur J Nucl Med Mol Imaging, 2015. **42**(4): p. 579-96.
28. Willmann, J.K., et al., *Molecular imaging in drug development.* Nat Rev Drug Discov, 2008. **7**(7): p. 591-607.
29. Ashton, J.R., J.L. West, and C.T. Badea, *In vivo small animal micro-CT using nanoparticle contrast agents.* Front Pharmacol, 2015. **6**: p. 256.
30. Badea, C.T., et al., *In vivo small-animal imaging using micro-CT and digital subtraction angiography.* Phys Med Biol, 2008. **53**(19): p. R319-50.
31. Weissleder, R. and M.J. Pittet, *Imaging in the era of molecular oncology.* Nature, 2008. **452**(7187): p. 580-9.
32. Lakowicz, J.R., *Principles of frequency-domain fluorescence spectroscopy and applications to cell membranes.* Subcell Biochem, 1988. **13**: p. 89-126.
33. Mahmood, U. and R. Weissleder, *Near-infrared optical imaging of proteases in cancer.* Mol Cancer Ther, 2003. **2**(5): p. 489-96.
34. Phan, T.G. and A. Bullen, *Practical intravital two-photon microscopy for immunological research: faster, brighter, deeper.* Immunol Cell Biol, 2010. **88**(4): p. 438-44.
35. Vahrmeijer, A.L., et al., *Image-guided cancer surgery using near-infrared fluorescence.* Nat Rev Clin Oncol, 2013. **10**(9): p. 507-18.
36. Ntziachristos, V., *Fluorescence molecular imaging.* Annu Rev Biomed Eng, 2006. **8**: p. 1-33.
37. Ntziachristos, V., et al., *Looking and listening to light: the evolution of whole-body photonic imaging.* Nat Biotechnol, 2005. **23**(3): p. 313-20.
38. Kosaka, N., et al., *Clinical implications of near-infrared fluorescence imaging in cancer.* Future Oncol, 2009. **5**(9): p. 1501-11.
39. de la Zerda, A., et al., *A comparison between time domain and spectral imaging systems for imaging quantum dots in small living animals.* Mol Imaging Biol, 2010. **12**(5): p. 500-8.

40. Mondal, S.B., et al., *Real-time fluorescence image-guided oncologic surgery.* Adv Cancer Res, 2014. **124**: p. 171-211.
41. Frangioni, J.V., *New technologies for human cancer imaging.* J Clin Oncol, 2008. **26**(24): p. 4012-21.
42. van der Vorst, J.R., et al., *Near-infrared fluorescence imaging of a solitary fibrous tumor of the pancreas using methylene blue.* World J Gastrointest Surg, 2012. **4**(7): p. 180-4.
43. Stummer, W., et al., *Fluorescence-guided surgery with 5-aminolevulinic acid for resection of malignant glioma: a randomised controlled multicentre phase III trial.* Lancet Oncol, 2006. **7**(5): p. 392-401.
44. Ishizawa, T., et al., *Real-time identification of liver cancers by using indocyanine green fluorescent imaging.* Cancer, 2009. **115**(11): p. 2491-504.
45. Motekallemi, A., et al., *The current status of 5-ALA fluorescence-guided resection of intracranial meningiomas-a critical review.* Neurosurg Rev, 2015. **38**(4): p. 619-28.
46. Jonckheere, N., N. Skrypek, and I. Van Seuningen, *Mucins and pancreatic cancer.* Cancers (Basel), 2010. **2**(4): p. 1794-812.
47. Hanahan, D. and R.A. Weinberg, *The hallmarks of cancer.* Cell, 2000. **100**(1): p. 57-70.
48. Tobita, K., et al., *Epidermal growth factor receptor expression in human pancreatic cancer: Significance for liver metastasis.* Int J Mol Med, 2003. **11**(3): p. 305-9.
49. Shaib, W., R. Mahajan, and B. El-Rayes, *Markers of resistance to anti-EGFR therapy in colorectal cancer.* J Gastrointest Oncol, 2013. **4**(3): p. 308-18.
50. Oliveira-Cunha, M., W.G. Newman, and A.K. Siriwardena, *Epidermal growth factor receptor in pancreatic cancer.* Cancers (Basel), 2011. **3**(2): p. 1513-26.
51. Faller, B.A. and B. Burtness, *Treatment of pancreatic cancer with epidermal growth factor receptor-targeted therapy.* Biologics, 2009. **3**: p. 419-28.
52. Raymond, E., S. Faivre, and J.P. Armand, *Epidermal growth factor receptor tyrosine kinase as a target for anticancer therapy.* Drugs, 2000. **60 Suppl 1**: p. 15-23; discussion 41-2.
53. Tebbutt, N., M.W. Pedersen, and T.G. Johns, *Targeting the ERBB family in cancer: couples therapy.* Nat Rev Cancer, 2013. **13**(9): p. 663-73.
54. Schmitz, K.R. and K.M. Ferguson, *Interaction of antibodies with ErbB receptor extracellular regions.* Exp Cell Res, 2009. **315**(4): p. 659-70.
55. Faloppi, L., K. Andrikou, and S. Cascinu, *Cetuximab: still an option in the treatment of pancreatic cancer?* Expert Opin Biol Ther, 2013. **13**(5): p. 791-801.
56. Conradt, L., et al., *Disclosure of erlotinib as a multikinase inhibitor in pancreatic ductal adenocarcinoma.* Neoplasia, 2011. **13**(11): p. 1026-34.
57. Reshkin, S.J., R.A. Cardone, and S. Harguindey, *Na+-H+ exchanger, pH regulation and cancer.* Recent Pat Anticancer Drug Discov, 2013. **8**(1): p. 85-99.
58. Webb, B.A., et al., *Dysregulated pH: a perfect storm for cancer progression.* Nat Rev Cancer, 2011. **11**(9): p. 671-7.
59. Kumar, A.P., et al., *Repression of NHE1 expression by PPARgamma activation is a potential new approach for specific inhibition of the growth of tumor cells in vitro and in vivo.* Cancer Res, 2009. **69**(22): p. 8636-44.
60. Chiang, Y., et al., *EGF upregulates Na+/H+ exchanger NHE1 by post-translational regulation that is important for cervical cancer cell invasiveness.* J Cell Physiol, 2008. **214**(3): p. 810-9.

61. Miraglia, E., et al., *Na+/H+ exchanger activity is increased in doxorubicin-resistant human colon cancer cells and its modulation modifies the sensitivity of the cells to doxorubicin.* Int J Cancer, 2005. **115**(6): p. 924-9.
62. Martinez-Zaguilan, R., et al., *Vacuolar-type H(+)-ATPases are functionally expressed in plasma membranes of human tumor cells.* Am J Physiol, 1993. **265**(4 Pt 1): p. C1015-29.
63. Sennoune, S.R., et al., *Vacuolar H+-ATPase in human breast cancer cells with distinct metastatic potential: distribution and functional activity.* Am J Physiol Cell Physiol, 2004. **286**(6): p. C1443-52.
64. Pinheiro, C., et al., *Expression of monocarboxylate transporters 1, 2, and 4 in human tumours and their association with CD147 and CD44.* J Biomed Biotechnol, 2010. **2010**: p. 427694.
65. Chiche, J., et al., *In vivo pH in metabolic-defective Ras-transformed fibroblast tumors: key role of the monocarboxylate transporter, MCT4, for inducing an alkaline intracellular pH.* Int J Cancer, 2012. **130**(7): p. 1511-20.
66. Pinheiro, C., et al., *Increasing expression of monocarboxylate transporters 1 and 4 along progression to invasive cervical carcinoma.* Int J Gynecol Pathol, 2008. **27**(4): p. 568-74.
67. Kemp, G., H. Young, and L. Fliegel, *Structure and function of the human Na+/H+ exchanger isoform 1.* Channels (Austin), 2008. **2**(5): p. 329-36.
68. Putney, L.K., S.P. Denker, and D.L. Barber, *The changing face of the Na+/H+ exchanger, NHE1: structure, regulation, and cellular actions.* Annu Rev Pharmacol Toxicol, 2002. **42**: p. 527-52.
69. Tominaga, T. and D.L. Barber, *Na-H exchange acts downstream of RhoA to regulate integrin-induced cell adhesion and spreading.* Mol Biol Cell, 1998. **9**(8): p. 2287-303.
70. Bourguignon, L.Y., et al., *CD44 interaction with Na+-H+ exchanger (NHE1) creates acidic microenvironments leading to hyaluronidase-2 and cathepsin B activation and breast tumor cell invasion.* J Biol Chem, 2004. **279**(26): p. 26991-7007.
71. Pedersen, S.F., *The Na+/H+ exchanger NHE1 in stress-induced signal transduction: implications for cell proliferation and cell death.* Pflugers Arch, 2006. **452**(3): p. 249-59.
72. Hoffmann, E.K. and S.F. Pedersen, *Cell volume homeostatic mechanisms: effectors and signalling pathways.* Acta Physiol (Oxf), 2011. **202**(3): p. 465-85.
73. Cardone, R.A., et al., *A novel NHE1-centered signaling cassette drives epidermal growth factor receptor-dependent pancreatic tumor metastasis and is a target for combination therapy.* Neoplasia, 2015. **17**(2): p. 155-66.
74. Cardone, R.A., et al., *The NHERF1 PDZ2 domain regulates PKA-RhoA-p38-mediated NHE1 activation and invasion in breast tumor cells.* Mol Biol Cell, 2007. **18**(5): p. 1768-80.
75. Reshkin, S.J., et al., *Phosphoinositide 3-kinase is involved in the tumor-specific activation of human breast cancer cell Na(+)/H(+) exchange, motility, and invasion induced by serum deprivation.* J Biol Chem, 2000. **275**(8): p. 5361-9.
76. Busco, G., et al., *NHE1 promotes invadopodial ECM proteolysis through acidification of the peri-invadopodial space.* FASEB J, 2010. **24**(10): p. 3903-15.
77. Yang, X., et al., *Inhibition of Na(+)/H(+) exchanger 1 by 5-(N-ethyl-N-isopropyl) amiloride reduces hypoxia-induced hepatocellular carcinoma invasion and motility.* Cancer Lett, 2010. **295**(2): p. 198-204.

78. Rios, E.J., et al., *Chronic hypoxia elevates intracellular pH and activates Na+/H+ exchange in pulmonary arterial smooth muscle cells.* Am J Physiol Lung Cell Mol Physiol, 2005. **289**(5): p. L867-74.
79. Lucien, F., et al., *Hypoxia-induced invadopodia formation involves activation of NHE-1 by the p90 ribosomal S6 kinase (p90RSK).* PLoS One, 2011. **6**(12): p. e28851.
80. Paradiso, A., et al., *The Na+-H+ exchanger-1 induces cytoskeletal changes involving reciprocal RhoA and Rac1 signaling, resulting in motility and invasion in MDA-MB-435 cells.* Breast Cancer Res, 2004. **6**(6): p. R616-28.
81. Magalhaes, M.A., et al., *Cortactin phosphorylation regulates cell invasion through a pH-dependent pathway.* J Cell Biol, 2011. **195**(5): p. 903-20.
82. Martin, C., et al., *Intracellular pH gradients in migrating cells.* Am J Physiol Cell Physiol, 2011. **300**(3): p. C490-5.
83. Stock, C., et al., *Protons extruded by NHE1: digestive or glue?* Eur J Cell Biol, 2008. **87**(8-9): p. 591-9.
84. Garty, H. and D.J. Benos, *Characteristics and regulatory mechanisms of the amiloride-blockable Na+ channel.* Physiol Rev, 1988. **68**(2): p. 309-73.
85. Schneider, C.A., W.S. Rasband, and K.W. Eliceiri, *NIH Image to ImageJ: 25 years of image analysis.* Nat Methods, 2012. **9**(7): p. 671-5.
86. Hammer, Ø.H., D. A. T. I; Ryan, P. D. PAST: Paleontological Statistics Software Package for Education and Data Analysis. Palaeontol. Electron. 2001, 4, 9.
87. Deer, E.L., et al., *Phenotype and genotype of pancreatic cancer cell lines.* Pancreas, 2010. **39**(4): p. 425-35.
88. Chen, W.H., et al., *Human pancreatic adenocarcinoma: in vitro and in vivo morphology of a new tumor line established from ascites.* In Vitro, 1982. **18**(1): p. 24-34.
89. Tan, M.H. and T.M. Chu, *Characterization of the tumorigenic and metastatic properties of a human pancreatic tumor cell line (AsPC-1) implanted orthotopically into nude mice.* Tumour Biol, 1985. **6**(1): p. 89-98.
90. Hoffman, R.M., *Orthotopic metastatic mouse models for anticancer drug discovery and evaluation: a bridge to the clinic.* Invest New Drugs, 1999. **17**(4): p. 343-59.
91. Kyriazis, A.P., et al., *Human pancreatic adenocarcinoma line Capan-1 in tissue culture and the nude mouse: morphologic, biologic, and biochemical characteristics.* Am J Pathol, 1982. **106**(2): p. 250-60.
92. Nielsen, C.H., et al., *In vivo imaging of therapy response to a novel pan-HER antibody mixture using FDG and FLT positron emission tomography.* Oncotarget, 2015. **6**(35): p. 37486-99.
93. Napp, J., et al., *Time-domain in vivo near infrared fluorescence imaging for evaluation of matriptase as a potential target for the development of novel, inhibitor-based tumor therapies.* Int J Cancer, 2010. **127**(8): p. 1958-74.
94. Bachem, M.G., et al., *Pancreatic carcinoma cells induce fibrosis by stimulating proliferation and matrix synthesis of stellate cells.* Gastroenterology, 2005. **128**(4): p. 907-21.
95. Huynh, A.S., et al., *Development of an orthotopic human pancreatic cancer xenograft model using ultrasound guided injection of cells.* PLoS One, 2011. **6**(5): p. e20330.
96. Buckway, B., et al., *Overcoming the stromal barrier for targeted delivery of HPMA copolymers to pancreatic tumors.* Int J Pharm, 2013. **456**(1): p. 202-11.

97. Provenzano, P.P., et al., *Collagen reorganization at the tumor-stromal interface facilitates local invasion.* BMC Med, 2006. **4**(1): p. 38.
98. Netti, P.A., et al., *Role of extracellular matrix assembly in interstitial transport in solid tumors.* Cancer Res, 2000. **60**(9): p. 2497-503.
99. Cruz-Monserrate, Z., et al., *Targeting pancreatic ductal adenocarcinoma acidic microenvironment.* Sci Rep, 2014. **4**: p. 4410.
100. Lisy, M.R., et al., *In vivo near-infrared fluorescence imaging of carcinoembryonic antigen-expressing tumor cells in mice.* Radiology, 2008. **247**(3): p. 779-87.
101. Alves, F., et al., *Inhibitory effect of a matrix metalloproteinase inhibitor on growth and spread of human pancreatic ductal adenocarcinoma evaluated in an orthotopic severe combined immunodeficient (SCID) mouse model.* Cancer Lett, 2001. **165**(2): p. 161-70.
102. Vonlaufen, A., et al., *Pancreatic stellate cells: partners in crime with pancreatic cancer cells.* Cancer Res, 2008. **68**(7): p. 2085-93.
103. Kruwel, T., et al., *In vivo detection of small tumour lesions by multi-pinhole SPECT applying a (99m)Tc-labelled nanobody targeting the Epidermal Growth Factor Receptor.* Sci Rep, 2016. **6**: p. 21834.
104. Hudson, S.V., et al., *Targeted noninvasive imaging of EGFR-expressing orthotopic pancreatic cancer using multispectral optoacoustic tomography.* Cancer Res, 2014. **74**(21): p. 6271-9.
105. Pleijhuis, R.G., et al., *Near-infrared fluorescence (NIRF) imaging in breast-conserving surgery: assessing intraoperative techniques in tissue-simulating breast phantoms.* Eur J Surg Oncol, 2011. **37**(1): p. 32-9.
106. McElroy, M., et al., *Imaging of primary and metastatic pancreatic cancer using a fluorophore-conjugated anti-CA19-9 antibody for surgical navigation.* World J Surg, 2008. **32**(6): p. 1057-66.
107. Park, J.Y., et al., *MUC1 selectively targets human pancreatic cancer in orthotopic nude mouse models.* PLoS One, 2015. **10**(3): p. e0122100.
108. Keereweer, S., et al., *Optical image-guided cancer surgery: challenges and limitations.* Clin Cancer Res, 2013. **19**(14): p. 3745-54.
109. de Boer, E., et al., *In Vivo Fluorescence Immunohistochemistry: Localization of Fluorescently Labeled Cetuximab in Squamous Cell Carcinomas.* Sci Rep, 2015. **5**: p. 10169.
110. van Driel, P.B., et al., *Characterization and evaluation of the artemis camera for fluorescence-guided cancer surgery.* Mol Imaging Biol, 2015. **17**(3): p. 413-23.
111. Korb, M.L., et al., *Use of monoclonal antibody-IRDye800CW bioconjugates in the resection of breast cancer.* J Surg Res, 2014. **188**(1): p. 119-28.
112. Day, K.E., et al., *Preclinical comparison of near-infrared-labeled cetuximab and panitumumab for optical imaging of head and neck squamous cell carcinoma.* Mol Imaging Biol, 2013. **15**(6): p. 722-9.
113. Boonstra, M.C., et al., *Preclinical evaluation of a novel CEA-targeting near-infrared fluorescent tracer delineating colorectal and pancreatic tumors.* Int J Cancer, 2015. **137**(8): p. 1910-20.
114. Metildi, C.A., et al., *Fluorescence-guided surgery with a fluorophore-conjugated antibody to carcinoembryonic antigen (CEA), that highlights the tumor, improves surgical resection and increases survival in orthotopic mouse models of human pancreatic cancer.* Ann Surg Oncol, 2014. **21**(4): p. 1405-11.
115. Metildi, C.A., et al., *Advantages of fluorescence-guided laparoscopic surgery of pancreatic cancer labeled with fluorescent anti-carcinoembryonic antigen*

antibodies in an orthotopic mouse model. J Am Coll Surg, 2014. **219**(1): p. 132-41.

116. Hofmann, I., et al., *K-RAS mutant pancreatic tumors show higher sensitivity to MEK than to PI3K inhibition in vivo.* PLoS One, 2012. **7**(8): p. e44146.
117. Larbouret, C., et al., *In pancreatic carcinoma, dual EGFR/HER2 targeting with cetuximab/trastuzumab is more effective than treatment with trastuzumab/erlotinib or lapatinib alone: implication of receptors' down-regulation and dimers' disruption.* Neoplasia, 2012. **14**(2): p. 121-30.
118. Liles, J.S., et al., *Targeting ErbB3-mediated stromal-epithelial interactions in pancreatic ductal adenocarcinoma.* Br J Cancer, 2011. **105**(4): p. 523-33.
119. Rao, C.V., et al., *Simultaneous targeting of 5-LOX-COX and EGFR blocks progression of pancreatic ductal adenocarcinoma.* Oncotarget, 2015. **6**(32): p. 33290-305.
120. Aye, N.N., S. Komori, and K. Hashimoto, *Effects and interaction, of cariporide and preconditioning on cardiac arrhythmias and infarction in rat in vivo.* Br J Pharmacol, 1999. **127**(4): p. 1048-55.
121. Chaitman, B.R., *A review of the GUARDIAN trial results: clinical implications and the significance of elevated perioperative CK-MB on 6-month survival.* J Card Surg, 2003. **18 Suppl 1**: p. 13-20.

Curriculum vitae

PERSONAL INFORMATION:

Name: Mara
Surname: Saccomano
Date of birth: January 04th, 1985
Place of birth: Portogruaro (Venezia) – Italy
Natioinality: Italian
Present Adress: Maschmühlenweg, 5B, 37073. Göttingen

EDUCATION:

09.2012 - present	Marie Curie Fellowship (“IonTrac” Marie Curie ITN project) / PhD position “Molecular Medicine” program, University Medical Center of Göttingen, Germany Position at Max Planck Institute for Experimental Medicine of Göttingen, Germany - Department of molecular biology of neuronal signals Supervisor: Prof. Dr. Frauke Alves. Title of the thesis: Imaging techniques for novel pancreatic ductal adenocarcinoma (PDAC) diagnostics based on the transportome
06.2012 - 08.2012	Marie Curie Fellowship (“P^{3}AGI” Marie Curie PEOPLE-IAPP project) Position at University Medical Center of Göttingen - Department of Haematology and Oncology. Supervisor: Prof. Dr. Frauke Alves. Title of the project: *In vivo* detection of lung edema occurred in asthma by optical imaging analysis (Optix MX2) using a fluorescent-labeled albumin (BSA)
09.2011 - 06.2012	Marie Curie Fellowhip (“P3AGI” Marie Curie PEOPLE-IAPP) Position at Medical University of Wien, Austria - Department of Dermatology Supervisor: Dr. Michelle Epstein. Title of the project: FACS characterization of regulatory T cells isolated from spleen/lungs of asthmatic mice

02.2011 – 09-2011	Fellowship funded by AREA Science Park –Trieste (Italy) Position at CBM scrl (Cluster in Biomedicine), Trieste, Italy. Supervisor: Dr. Stefania Biffi Title of the project: *In vivo* optical imaging analysis (Optix MX2) in rats and mice
12.2007 – 04.2010	Master of Science at University of Trieste, Italy - Department of Life Science. Supervisor: Prof. Dr. Francesco Tedesco Title of the thesis: *In vivo* and *in vitro* validation of a phage display antibody against anti beta 2 glycoprotein
09.2004 – 12.2007	Bachelor of Science at University of Trieste, Italy – Department of Life Science Supervisor: Prof. Dr. Francesco Tedesco Title of the thesis: Screening of sera of patients with antiphospholipid syndrome
06.2004	High School Diploma

CONTRIBUTION AT SCIENTIFIC MEETINGS:

09.2015	Poster and oral presentation “Visualization of human pancreatic ductal adenocarcinoma xenografts by near-infrared optical imaging in combination with fluorescent labeled Cetuximab” at the International Meeting on Ion Channels, Transporters and cancer - London, UK
06.2014	Poster presentation “Visualization of human pancreatic ductal adenocarcinoma xenografts with Cetuximab antibody - fluorescent labeled using non-invasive time-domain near-infrared optical imaging” at the European Molecular Imaging Meeting 2014 - Antwerp, The Netherland
03.2013	Oral presentation “Imaging techniques for PDAC diagnostics based on the “transportome” at the 2nd Ringberg Conference on Ion Channels and Cancer - Ringberg Castel, Germany
03.2013	Poster presentation ““Imaging techniques for pancreatic ductal adenocarcinoma (PDAC) diagnostics based on Eag1 voltage gated potassium channel” at the Winter school of “Namdiatream” EU-project - Villars sur Ollon, Switzerland.

05.2012	Poster presentation “Imaging techniques for pancreatic ductal adenocarcinoma (PDAC) diagnostics based on Eag1 voltage gated potassium channel” at the 45th Sandbjerg Meeting on Membrane Transport – Sandbjerg, Denmark